Lidar observations of natural and volcanic-ash-induced cirrus clouds

Christian Rolf

Mitglied der Helmholtz-Gemeinschaft

JÜLICH
FORSCHUNGSZENTRUM

Schriften des Forschungszentrums Jülich
Reihe Energie & Umwelt / Energy & Environment Band / Volume 163

Forschungszentrum Jülich GmbH
Institute of Energy and Climate Research (IEK)
Stratosphere (IEK-7)

Lidar observations of natural and volcanic-ash-induced cirrus clouds

Christian Rolf

Schriften des Forschungszentrums Jülich
Reihe Energie & Umwelt / Energy & Environment Band / Volume 163

ISSN 1866-1793 ISBN 978-3-89336-847-1

Bibliographic information published by the Deutsche Nationalbibliothek.
The Deutsche Nationalbibliothek lists this publication in the Deutsche Nationalbibliografie; detailed bibliographic data are available in the Internet at http://dnb.d-nb.de.

Publisher and Distributor:	Forschungszentrum Jülich GmbH Zentralbibliothek 52425 Jülich Phone +49 (0) 24 61 61-53 68 · Fax +49 (0) 24 61 61-61 03 e-mail: zb-publikation@fz-juelich.de Internet: http://www.fz-juelich.de/zb
Cover Design:	Grafische Medien, Forschungszentrum Jülich GmbH
Printer:	Grafische Medien, Forschungszentrum Jülich GmbH
Copyright:	Forschungszentrum Jülich 2013

Schriften des Forschungszentrums Jülich
Reihe Energie & Umwelt / Energy & Environment Band / Volume 163

D 468 (Diss., Wuppertal, Univ., 2012)

ISSN 1866-1793
ISBN 978-3-89336-847-1

The complete volume is freely available on the Internet on the Jülicher Open Access Server (JUWEL) at http://www.fz-juelich.de/zb/juwel

Abstract

Cirrus clouds - which consist solely of ice particles - influence the Earth's radiation budget and thus the climate system since they scatter the incoming solar radiation (cooling effect) and absorb the outgoing radiation of the Earth (warming effect). However, this influence has not yet been quantified. The purpose of this thesis is to extend our knowledge about cirrus with the help of lidar measurements in combination with model simulations.

In the first part, observations of cirrus clouds made with a backscatter lidar over Jülich are presented, focusing on obtaining a representative cirrus climatology. The cirrus clouds are evaluated with a temporal average extinction profile by considering a multiple scattering correction. By using additional meteorological data, the climatological observations are analyzed under macrophysical, radiative, and microphysical aspects and considered to be representative in comparison to other mid-latitude lidar climatologies. Most of the observed cirrus clouds were generated due to synoptic weather patterns (e.g. frontal systems), showing a large vertical thickness of about 2.2 km and occurring mostly directly below the tropopause. Mean and median values of optical depth are found to be around 0.28 and 0.12 (range: 0.002 - 3), respectively. The most frequently observed ice water content (IWC) was found to be 6 ppmv (range: 0.01 - 400 ppmv). The lowest detected IWC values from aircraft in situ measurements ($\sim$ 0.01 ppmv) are confirmed by the lidar observations. This result is of importance, since up to now it has been unclear whether in situ aircraft instruments were able to detect the thinnest cirrus clouds.

In the second part of the thesis, heterogeneous ice formation induced by volcanic ash from the Eyjafjallajökull volcano eruption in April 2010 is investigated based on a lidar observation of an ash-induced cirrus cloud in combination with model simulations along air mass trajectories. The microphysical properties of the cirrus cloud can only be represented by the microphysical model simulations on the assumption of an enhanced number of efficient ice nuclei (IN) originating from the volcanic eruption. The IN concentration determined by lidar measurements directly before and after cirrus cloud occurrence implies a value of around 0.1 cm^{-3} (in comparison to normal IN conditions of 0.01 cm^{-3}). This leads to a cirrus cloud with rather small ice crystals having a mean radius of 12 µm and a modification of the ice particle number (0.08 cm^{-3} instead of $3 \cdot 10^{-4}$ cm^{-3} under normal IN conditions). The effectiveness of IN was estimated by the microphysical model and the backward trajectories based on ECMWF data, establishing a freezing threshold of around 105 % relative humidity with respect to ice in a temperature range from -45 to $-55°C$. Only these highly efficient IN made the formation of the cirrus cloud in a slightly supersaturated environment possible. With the help of this case study, the possible influence of IN on the appearance and microphysical - and thus radiative - properties of cirrus clouds was demonstrated. From an additional set of idealized model simulations it can be concluded that the microphysical and thus optical properties of cirrus clouds are affected for the complete range of atmospheric conditions in the presence of a high number of IN.

Zusammenfassung

Zirruswolken, die komplett aus Eiskristallen bestehen, beeinflussen den Strahlungshaushalt der Erde und somit auch das Klimasystem, da sie die einfallende solare Strahlung streuen (kühlender Einfluss) und emittierte Strahlung der Erde absorbieren (wärmender Einfluss). Dieser Einfluss ist jedoch bis heute noch nicht genau quantifiziert. Das Ziel dieser Arbeit ist es mit Hilfe von Lidar Messungen in Kombination mit Modellsimulationen das Verständnis über Zirren zu erweitern.

Im ersten Teil der Arbeit werden Beobachtungen von Zirruswolken mit einem Rückstreu-Lidar System über Jülich gezeigt, wobei der Fokus auf der Erstellung einer repräsentativen Zirren Klimatologie liegt. Die Zirruswolken werden mit Hilfe eines gemessenen Extinktionsprofils, welches zuvor auf Mehrfachstreuung korrigiert wurde, ausgewertet. Die klimatologischen Beobachtungen sind mit Hilfe von zusätzlichen meteorologischen Daten unter makrophysikalischen, optischen und mikrophysikalischen Aspekten analysiert worden und sind repräsentativ im Vergleich zu anderen Lidar Klimatologien aus den mittleren Breiten. Die am häufigsten beobachteten Zirruswolken entstehen durch synoptische Wetterlagen (z.B. frontale Systeme), wodurch sie eine große vertikale Dicke von ungefähr 2.2 km haben und sich meist direkt unterhalb der Tropopause befinden. Die optischen Dicken der Zirruswolken liegen in einem Bereich von 0.002 bis 3 mit einem Mittelwert von 0.28 und einem Median von 0.12 beobachtet worden. Der häufigste Eiswassergehalt (IWC) liegt bei 6 ppmv in einem Bereich von 0.01 ppmv bis 400 ppmv. Damit bestätigen die Lidar Beobachtungen auch die niedrigsten Eiswassergehalte von Flugzeug in-situ Messungen ($\sim$ 0.01 ppmv). Dies ist wichtig, weil es bis dato nicht sicher war, ob flugzeuggetragene in-situ Instrumente die dünnsten Zirruswolken erfassen können.

Im zweiten Teil der Arbeit wird heterogene Eisbildung untersucht, basierend auf der Lidarmessung einer Zirruswolke die sich an Vulkanasche des Eyjafjallajökull Vulkans im April 2010 gebildet hat. Dazu wurden Modellsimulationen entlang von Luftmassen Trajektorien mit dem mikrophysikalischen Modell MAID durchgeführt. Die mikrophysikalischen Eigenschaften der Zirruswolke können von dem Modell nur unter der Annahme einer erhöhten Konzentration von sehr effizienten Eiskeimen (IN), verursacht durch den Vulkanausbruch, reproduziert werden. Die Eiskeim-Konzentration von 0.1 cm^{-3} ist durch die Lidar Messungen direkt vor und nach Auftreten der Zirruswolke bestimmt worden (im Vergleich liegt die normale Eiskeim Konzentration bei 0.01 cm^{-3}). Dies führt zu einer Zirruswolke mit eher kleinen Eiskristallen mit einem mittleren Radius von 12 µm und zu einer Erhöhung der Konzentration (0.08 cm^{-3} im Vergleich zu $3 \cdot 10^{-4}$ cm^{-3} unter normalen Bedingungen). Die Effizienz der Eiskeime ist mit Hilfe des mikrophysikalischen Modells und den Rückwärtstrajektorien basierend auf ECMWF Daten bestimmt worden. Dabei ergibt sich eine Gefrierschwelle von ungefähr 105 % relative Feuchte im Bezug auf Eis in einem Temperaturbereich von -45 bis -55°C. Nur mit diesen hocheffizienten Eiskeimen war es möglich, dass sich eine Zirruswolke in einer nur leicht übersättigten Umgebung bilden konnte. Mit Hilfe dieser Fallstudie ist es möglich, den Einfluss von

Eiskeimen auf die Bildung von Zirruswolken und deren mikrophysikalischen Eigenschaften (d.h. auch Strahlungseigenschaften) abzuschätzen. Durch zusätzliche idealisierte Modellsimulationen kann gezeigt werden, dass mikrophysikalische und optische Eigenschaften von Zirruswolken über den kompletten Bereich atmosphärischer Bedingungen durch das Vorhandensein einer hohen Konzentration von Eiskeimen beeinflusst werden.

Contents

List of Figures

List of Tables

1 Introduction

Clouds play an important role by influencing the Earth's radiation budget and the global climate (Heintzenberg and Charlson, 2009). This is shown in the current report of the Intergovernmental Panel on Climate Change (IPCC, 2007), where the large error bars relating to cloud radiative forcing underline the poor scientific knowledge of the underlying processes.

Cirrus clouds which consists solely of ice particles have a varying effect on the radiation budget and therefore it is difficult to estimate their climate impact. Microphysical properties like size, shape, and orientation determine the optical properties of a cirrus cloud. Especially the mostly unknown shape and orientation of ice particles represent a problem in comparison to warm liquid clouds with spherical droplets. Cirrus clouds trap outgoing long-wave radiation (greenhouse effect) and reflect the solar radiation (albedo effect). Depending on their optical depth and cloud top height, the net effect may be warming or even cooling. Optical thin cirrus clouds allow most of the sun radiation to reach the Earth's surface. They also absorb infrared radiation from the Earth and re-emit it at colder temperatures, which leads to a net warming effect. In contrast, the solar albedo effect dominates the radiation budget in optically thick cirrus clouds which leads to a net cooling (Kärcher and Spichtinger, 2009). Besides, the albedo effect is larger for small effective ice particle radii than the absorption of long-wave radiation. Furthermore, this radiation can have dramatic effects on cirrus itself causing changes in inhomogeneity and lifetime by local warming (Dobbie and Jonas, 2001). Radiative cooling at cloud top may create supersaturation high enough to initiate ice formation. Cirrus development is controlled by solar radiation in the case of cirrus optical depths in the range between 1 and 2, whereas clouds with optical depths larger than 2 are more greatly affected by long-wave radiation. Finally, estimating warming and cooling effects of cirrus clouds is highly uncertain, due to the mostly unknown microphysical properties and spatial structure of the clouds as mentioned in IPCC (2007). By considering only the effects on spatial inhomogeneity of cirrus clouds the radiative forcing in global models may change locally by several 10 W/m^2 (Gu and Liou, 2006). Furthermore, the behavior and prediction of cirrus clouds in future climate, with a global change in temperature, relative humidity, and cooling rates, cannot be predicted unless the underlying processes of formation, development, and environmental impacts of ice particles are clearly understood.

The direct impact of cirrus clouds on climate change is based on their substantial radiative effects, but they can also contribute indirectly by partial control of stratospheric water vapor concentration (Holton and Gettelman, 2001) and impact on tropospheric ozone by providing

surfaces for heterogeneous chemistry (Thornton et al., 2007).

It is known that the radiative properties of clouds are indirectly influenced by aerosols. The indirect effects are manifold and difficult to assess. The most relevant indirect aerosol effect is ascribed to modification of cirrus cloud microphysical properties as mentioned by IPCC (2007). Indirect aerosol effects occur either on homogeneously or heterogeneously formed cirrus clouds (see Section 2.3). While only a very high amount of solution droplets can influence homogeneous ice microphysics, heterogeneous freezing is strongly affected by ice nuclei (IN) similar to the influence of cloud condensation nuclei (CCN) on warm liquid clouds (Twomey, 1974).

In general, heterogeneous freezing always occurs before homogeneous freezing, but the role of heterogeneous freezing in the atmosphere is largely unknown. However, IN can have a significant impact on the formation and evolution of natural cirrus clouds (DeMott et al., 2003; Spichtinger and Cziczo, 2010). Tropospheric ice nuclei concentrations can vary over several orders of magnitude and are related to human activity or natural sources (DeMott et al., 2010). Even industrial activities or aircraft exhausts provide a strong source of potential IN. However, a non-neglectable and often much larger IN source is of natural origins, such as biomass burning, mineral dust outbreaks or volcanic eruptions (Rolf et al., 2012). Many laboratory studies have investigated the suitability of different types of aerosols to serve as IN. Their efficiency to nucleate ice varies due to chemical and morphological properties or potential coatings of the IN surface by organics or sulfuric acid (e.g. Mangold et al., 2005; Moehler et al., 2008; Cziczo et al., 2009). They may be potentially efficient IN species such as mineral dust, metals, and some biological particles (e.g. pollen, bacteria) or less efficient such as soot-coated particles. The complex relations between IN and cirrus cloud particles, as well as the source strength of IN, are still not sufficiently well established.

It is generally difficult to observe ice nucleation processes and the impact of potential IN on cirrus clouds in the higher atmosphere. Aircraft in situ measurements of cirrus clouds provide microphysical properties of the current state of the observed cloud. Ongoing improvements in measurement techniques allow us to determine many quantities concerning ice particles and aerosols in situ, but there is still a need for progress to reduce uncertainties and improve general particle identification (Baumgardner et al., 2012). However, turbulence and air mixing produced by aircraft after flying through clouds and injection of exhausts prohibits multiple observations of the same cloud. Therefore it is difficult to perform measurements with aircraft on cloud formation, evolution, and lifetime. In addition, the SPARC Water Vapor Assessment Report emphasized systematic and sometimes significant differences between different water vapor instruments measuring relative humidity with an overall uncertainty of 5 to 10 % at temperatures above 210 K (Kley et al., 2000). However, even this quantity constitutes a crucial parameter of cirrus process understanding.

A vertical cloud profile can be obtained by remote sensing lidar instruments. This contact-free measurement technique allows the observation of the same cloud over an extended

time period and is therefore a useful method to investigate impacts on cloud formation and evolution. However, the lidar instrument provides only optical cloud particle properties and the microphysical properties have to be derived. The concentration and size of scattering particles limits the applicability of the lidar technique. The short wavelengths used by lidars are suitable to detect aerosols, whereas a large amount of larger particles like cloud droplets or ice particles rapidly attenuate the received signal. Depending on the lidar system the determination of microphysical properties of the scattering particles is often not possible from the lidar measurements alone. In addition, the differentiation of aerosol particles from cloud particles and mixtures of both requires a considerable effort and cannot usually be achieved without further information.

Microphysical models are helpful tools for investigations of cloud formation, evolution and underlying microphysics. This work uses the approach of combining optical particles properties obtained with a lidar instrument merged with microphysical properties provided by a model. Case studies of aerosol cloud interactions are possible with this combination. Here, the impact of volcanic ash particles on cirrus formation and the modification of cloud microphysics is investigated based on the eruption of the Eyjafjallajökull volcano in 2010. The case study focuses on an atmospheric observation of an ash-induced cirrus cloud with a lidar, reproduced by simulations with the microphysical Model for Aerosol and Ice Dynamics (MAID). The simulations provide information on the microphysical properties of the ash-induced cirrus cloud and the conditions for the development of such clouds.

While case studies are useful to investigate specific processes, monitoring of cirrus clouds provides information on a wider temporal (long observation period) and local scale (observations at many places). Climatologies can be used to validate instruments or make a comparison with global models. Such a broad dataset of atmospheric cirrus observations also allows parametrizations to be developed that are required to estimate the role of cirrus clouds with global climate models. Here, climatological cirrus observations with a lidar, representative of mid-latitudes, from April 2011 to April 2012 are compared to other lidar measurements. Furthermore, the lidar cirrus climatology is used to assess the aircraft in situ IWC climatology from Schiller et al. (2008) and the extended version by Luebke et al. (2012).

This thesis is structured as follows. In the next section scientific questions are formulated to summarize the main issues concerning this work. After the Introduction a general overview of the current understanding of cirrus clouds is given in Chapter 2. The dynamics and occurrence, important measurement parameters, and ice formation (i.e. homogeneous and heterogeneous freezing) of cirrus clouds are discussed. Chapter 3 briefly describes the principle of the box model MAID and the model extension by a sedimentation module is discussed in more detailed. MAID simulates atmospheric ice formation along air parcel trajectories. Thus, a precise and realistic trajectory preparation and model initialization is required. In Chapter 4, the lidar measurement technique and the lidar instrument are introduced. Since this measurement principle has been only recently established at IEK-7 it is described in

more detailed. Besides the instrument itself, the steps taken to identify, classify, and analyze cirrus clouds are presented. Effects such as multiple scattering and specular reflection have to be considered and are explained accordingly. Chapter 5 presents the climatological cirrus measurements taken over Jülich in the west of Germany. These cirrus observations are analyzed for macrophysical, radiative, and microphysical properties and are compared to other lidar climatologies. A comparison between the mid-latitude lidar climatology and an aircraft base in situ climatology is shown. The case study of cirrus formation influenced by volcanic ash is presented in Chapter 6. Estimation of IN concentration based on the lidar measurements, observation and simulation of the ash-induced cirrus cloud as well as the general effect of a high number of efficient IN on cirrus microphysics is shown. Results concerning the atmospheric relevance of IN numbers and their influence on cirrus microphysics are described based on idealized model sensitivity studies. Finally, Chapter 7 summarizes and concludes this work and provides a further outlook.

1.1 Scientific questions

The following scientific questions are intent to represent and summarize the orientation of this work and help to expand the current state of knowledge.

1. *Do aircraft in situ water instruments - in particular the hygrometers FISH and CLH - identify thin cirrus clouds?*

   Aircraft in situ measurements are a powerful tool for detailed investigations of cloud microphysics. Accurate measurements of ice water content (IWC) are required for the investigation of cirrus clouds and mixed phase clouds (Baumgardner et al., 2012). For example, the FISH instrument, which measures total water vapor, is used to obtain the IWC. A heated forward-facing inlet system transports air and evaporate ice particles from outside the aircraft to the instrument, which results in a total water vapor measurement. The IWC can be derived by additionally measuring the gas phase water vapor. The quality of the IWC measurements depends on the water vapor uncertainty itself and the ice particle sampling efficiency of the inlet (Krämer and Afchine, 2004). In the case of warmer thin cirrus clouds, the amount of water vapor in the condensed phase is usually very small relative to the gas phase water vapor, since the amount of water vapor increases with temperature. Thus water instruments with a typical uncertainty of 6 % could not clearly identify small amounts of IWC below 7 % of the gas phase water vapor measurements (Schiller et al., 2008). Below this ratio it is uncertain whether the signal stems from instrument uncertainties or from a cloud (Krämer et al., 2009). One purpose of this study is to compare cirrus climatologies measured from aircraft to that measured with a ground-based lidar instrument. This leads to a further question: Is it possible to obtain a representative lidar cirrus climatology to validate in situ instruments?

2. *Is it possible to derive cirrus microphysical properties from lidar observations?*

   Microphysical properties of cirrus clouds determine the radiative characteristics and are related to their evolution. The exploration and extension of the current understanding of the complex processes in cirrus clouds are based on the knowledge of their microphysical properties. Deriving a relation between lidar-determined optical quantities and microphysical properties of measured cirrus cloud would considerably extend the database of cirrus observations, since lidar measurements are much easier to perform.

3. *Does volcanic ash from the Eyjafjallajökull volcano influence cirrus cloud formation?*

   The indirect aerosol impact on cirrus cloud formation depends on the availability of efficient IN. At the moment, there is a lack of IN observations, and the influence of volcanic ash on heterogeneous freezing is a matter of controversy. Some studies state that volcanic ash particles act as good IN (e.g. Isono et al., 1959; Durant et al., 2008; Fornea et al., 2009; Prenni et al., 2009), while others suggest that volcanic ash particles have no further impact as IN (e.g. Langer et al., 1974; Schnell and Delany, 1976). Is it possible to estimate the freezing efficiency based on atmospheric lidar observations of an ash-influenced cirrus cloud? Can the cloud clearly be identified as ash-induced cirrus?

4. *What is the impact of a high amount of heterogeneous efficient IN and is it of significance for the atmosphere?*

   Typical IN concentrations of 0.01 to 0.03 cm^{-3} at northern mid-latitudes are often found in in situ measurements (DeMott et al., 2003) and imply an impact on cirrus clouds via heterogeneous freezing. A high amount of IN can modify the microphysical properties by changing the size and number of ice particles (small and many ice particles). Thus, heterogeneous frozen ice particles reduce ice supersaturation by particle growth and could prevent homogeneous freezing from occurring as suggested by Kärcher and Lohmann (2003). An even higher IN concentration above 0.03 cm^{-3} could strongly modify the cirrus development. However, the role of IN and heterogeneous freezing in the atmosphere is largely unknown. An important question is therefore, whether it is possible to identify the impact of IN on cirrus microphysical properties.

2 Cirrus clouds

Cirrus clouds consist solely of ice particles. The formation process of these ice particles in the atmosphere is determined by the interplay of temperature, pressure, available water vapor, aerosol particle properties, and cooling rate. The best conditions for ice formation are found in the upper part of the troposphere up to the UT/LS region (Upper Troposphere and Lower Stratosphere). The versatility of different ice formation processes including the interaction of aerosols causes a large uncertainty in predicting climate effects of cirrus clouds. A general overview of cirrus clouds and ice formation in the atmosphere is given in the following sections.

2.1 Microphysical properties of cirrus clouds

The properties of a cirrus cloud are defined by microphysical quantities such as number concentration, size, and shape of ice particles. These microphysical quantities vary from cloud to cloud and depend mainly on the cloud dynamics and available water vapor.

Number concentration and size distribution are important parameters determining the radiative properties of cirrus clouds. Typical values for the total number concentration of ice particles are between 0.005 to 100 cm^{-3} and the mean radii range from 1 to 50 µm (Krämer et al., 2009). In general, the number concentration is strongly influenced by vertical updraft velocity (see Section 2.2 and 2.3.1). The weaker the updraft, the smaller the number concentration and vice versa. In general, number concentration as well as the mean radius increases with increasing temperature.

Ice particles can have different shapes influencing the radiative forcing of the cirrus cloud. The shape mostly depends on temperature and supersaturation. Temperature determines the basic shape of the ice particles formed, whereas supersaturation influences the particle complexity. While in a slightly supersaturated environment only simple particle forms like columns or plate crystals develop, complex dendritic structures occur in regions with higher supersaturations. Complex shapes occur in the temperature range from 0 to −38°C, where both ice crystals and liquid drops can exist. In cirrus altitudes with temperatures below −38°C the most likely particle shapes are simple ones, because of the low water vapor concentration available. In addition, at cold temperatures round forms are favored, whereas at high vertical velocities the complexity increases again (Bailey and Hallett, 2004). Complex shapes can also form due to collision and coalescence processes between several ice particles.

The ice water content (IWC) is the integral over the size distribution (number in specific size intervals) and therefore represents an important quantity for the characterization of cirrus cloud microphysics. The IWC represents the total amount of frozen water and is proportional to optical properties such as effective radius and extinction coefficient or optical depth. IWC is mainly determined by ice particle volume defined by a certain particle size. However, climatological cirrus observations show that the ice particle number is the crucial quantity representing IWC as ascertained by in situ measurements (Luebke et al., 2012). Typically values of IWC are spread over several orders of magnitudes from 10^{-3} to 10^{3} ppmv. It can be directly measured for example by aircraft in situ total water instruments (Schiller et al., 2008; Krämer et al., 2009; Davis et al., 2007; Luebke et al., 2012).

The optical depth is a radiative quantity which describes the transparency of cirrus cloud. While average cirrus optical depths rarely exceed a value of 5, optical depths in the range from around 10 to 50 are produced by cirrus clouds generated by strong convection. Thin cirrus clouds reach an optical depth of around 0.1 to 0.5, while sub-visible cirrus in contrast to the blue sky have values below 0.03.

2.2 Dynamics and occurrence

Cirrus clouds are classified by the WMO (World Meteorological Organization) mainly into three different types: cirrus, cirrocumulus, and cirrostratus. This classification is based on macrophysical properties and visual appearance. Further types are subvisible cirrus clouds, which are optically very thin, and contrails, ice clouds produced by aircraft. In general, cirrus clouds exist at altitudes above 6 km up to the tropopause region (12 to 18 km), where the temperatures are cold enough to form pure ice clouds. At temperatures below $-38°$C liquid cloud drops no longer from, but ice particles directly arise from the gas phase since the relative humidity at which ice forms is below water saturation. The global mean cirrus height is 9 km and the thickness is 1.5 km (Lynch et al., 2002; Schiller et al., 2008). The global coverage is on average about 30 % of the Earth's surface, where the occurrence above land masses - especially mountain regions - is larger compared to the oceans (Dean et al., 2005). Seasonal variations in the tropics and subtropics are related to cycles of convective activity and movement of the ITCZ (Inter-Tropical Convection Zone), whereas the seasonal variation at mid-latitudes is weaker and linked to synoptic dynamics (Stubenrauch et al., 2006).

Ice formation can only happen with a decrease in temperature and a respective increase in relative humidity due to either the presence of vertical updraft of air masses (which corresponds to an adiabatic cooling rate), turbulent mixing of air parcels caused by dynamic instabilities, or diabatic effects from long-wave heating or shortwave cooling. The vertical updraft and adiabatic cooling represent the most generating mechanism important for ice particles (Kärcher and Spichtinger, 2009). With a constant amount of water vapor in the air mass the relative humidity increases with decreasing temperature as shown in Figure 2.1. When the saturation

level of the air mass (relative humidity with respect to ice of 100 %) is reached, ice formation can occur in principal. With further cooling of the air mass, supersaturation increases up to a critical threshold (yellow star in Figure 2.1), where ice nucleation starts. The value of this supersaturation threshold depends on the aerosol properties (see Section 2.3). Ice particles nucleate as long as supersaturation is above this threshold and starts to reduce the available water vapor in the air mass. By direct freezing of water molecules from the gas phase on the crystal surface, the ice particles grow and the relative humidity decreases again to the thermodynamic equilibrium of around 100 % or dynamic equilibrium (steady state) of $\geq$100 %. At these stages, the microphysical properties (i.e. size distribution, number concentration etc.) of the cirrus cloud remain constant.

The time between the start of ice nucleation and reaching thermodynamic or dynamic equilibrium between the solid and the gas phase is called relaxation time. The relaxation time depends on the vertical updraft velocity and ranges from less than one minute in convectively generated cirrus clouds to several hours and days in the case of synoptically generated cirrus clouds. The higher the ice particle number concentration is, the faster the supersaturation within the cloud is reduced and the shorter the relaxation time.

If the temperature increases, the ice particles begin to sublimate as long as the relative humidity is subsaturated. If the temperature decreases, ice particles become larger until they sediment out of the air mass to lower heights with warmer temperatures, where they start to sublimate. This behavior is shown in Figure 2.1 (without the evaporation phase), where the idealized life cycle of a cirrus cloud is depicted. Sedimentation constitutes an important factor

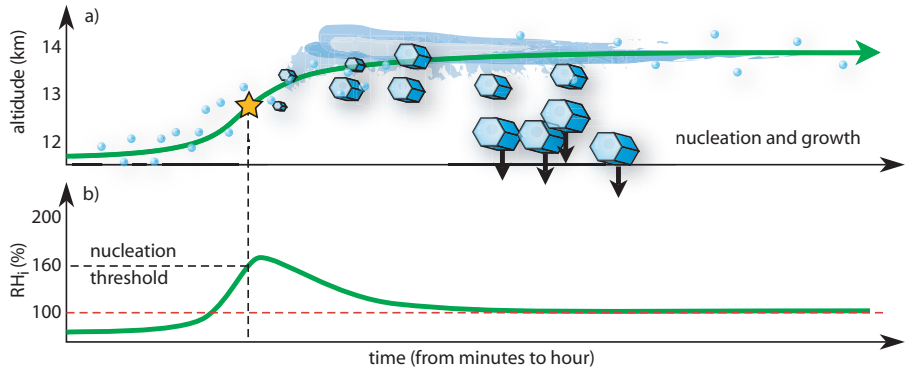

Figure 2.1: Schematic illustration of cirrus formation along the adiabatic ascent of an air mass. Panel a) shows the vertical movement of an air mass with respect to time and the ice particles formed, panel b) displays the corresponding relative humidity with respect to ice (RH_i). Adapted from Peter et al. (2006).

in determining cirrus morphology and development as outlined in Section 3.1.3.

As mentioned above, cirrus clouds develop at high altitudes below the tropopause and at a cooling rate caused by vertical updraft. The strength of the vertical updraft affects the increase of supersaturation with respect to ice per time and therefore the microphysical properties of the resulting cirrus cloud. In the atmosphere, mainly three cirrus-generating mechanism exist. Synoptic cirrus clouds generated from large-scale advection (i.e. warm front, jet stream, etc.) with relatively slow updraft velocities of below 10 cms^{-1} contain ice particles with a small number concentration of around $1 \cdot 10^{-1}$ cm^{-3} and mean radius of 10 µm and larger. Cirrus clouds generated by orographic waves as well as thunderstorms have considerably stronger updraft velocities of up to 25 ms^{-1}. This results in highly concentrated but smaller ice particles as can seen in a study by Kärcher and Lohmann (2002) (see next Section).

2.3 Ice formation in the atmosphere

Different pathways of ice formation and cirrus development exist in the atmosphere, and the nucleation pathway is crucial for the resulting microphysical properties of the cirrus. Ice formation is divided into heterogeneous and homogeneous freezing in general and is described in detailed in Lynch et al. (2002). At temperatures above −38°C (i.e. in mixed phase clouds), ice formation is initiated heterogeneous by insoluble IN, while homogeneous freezing of supercooled solution droplets additionally occurs in the cirrus temperature range below −38°C. It is believed that the most likely pathway for cirrus formation is homogeneous ice nucleation due to the overall availability of soluble supercooled aqueous sulfuric acid particles. Figure 2.2 illustrates all possible cirrus freezing pathways in the troposphere. Heterogeneous freezing in cirrus clouds can be further distinguished into two pathways depending on temperature and relative humidity with respect to ice. In general, heterogeneous freezing starts at lower supersaturation than homogeneous nucleation. In the next two sections both freezing mechanisms are described.

Besides classical ice formation due to heterogeneous and homogeneous freezing, additional processes exist which can change the number concentration of ice particles. In mixed phase clouds, ice multiplication with rime splintering, fragmentation during evaporation, or collision between ice particles is important, but is much less relevant for understanding ice formation in cirrus as mentioned in Cantrell and Heymsfield (2005); Kärcher and Spichtinger (2009). Therefore these processes, as well as the Bergeron-Findeisen process, are not further considered in this study concerning pure cirrus clouds.

2.3.1 Homogeneous freezing

Water can exist in the supercooled liquid phase below temperatures of 0°C without freezing. At a temperature of −38°C homogeneous freezing occurs spontaneously, depending on the size of the liquid droplet and dissolved components. In general, a stable embryonic crystallized

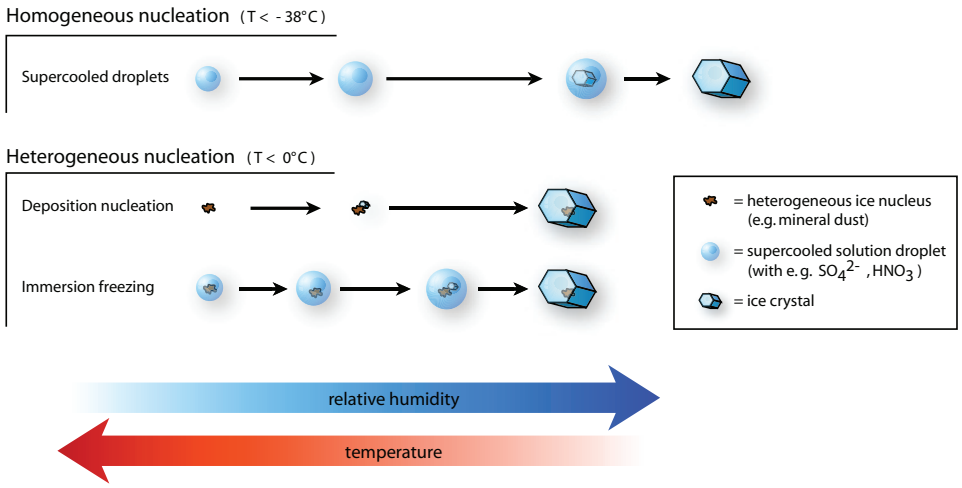

Figure 2.2: Cirrus freezing pathways of ice crystals in the atmosphere, mainly separated into homogeneous and heterogeneous freezing.

cluster in the supercooled liquid droplet is the starting point for homogeneous freezing. The statistical thermodynamic formation of these embryonic clusters depends strongly on the temperature. Due to thermodynamic fluctuations, embryos are formed until they reach a critical size, where the embryo is stable and its growth is favored. Then, the whole droplet starts to freeze. According to this, homogeneous nucleation is a stochastic process, where a certain probability of forming a stable embryo is given over the free energy, which is composed of the activation (Δg) and nucleation (ΔF_g) energy. The sum of both energies represents a barrier, which has to be exceeded in order to allow a phase transition from liquid to solid. While the activation energy is released when a water molecule aggregates on the more stable ice phase, the nucleation energy is the amount of energy which must be supplied by fluctuations in the liquid phase in order to let nucleation occur. The resulting nucleation rate coefficient J in units of $\mathrm{cm}^{-3}\mathrm{s}^{-1}$ after Pruppacher and Klett (1997) defines the number of critical embryos formed per time and volume and is given as:

$$J = 2N_c \left(\frac{\rho_{water}}{\rho_{ice} \cdot h}\right) \left(\sigma_{ice/water}\, k_B T\right)^{\frac{1}{2}} exp\left[-\frac{\Delta g}{RT} - \frac{\Delta F_g}{k_B T}\right] \tag{2.1}$$

where N_c is the concentration of monomers of water molecules, ρ_{ice} and ρ_{water} are the respective densities of ice and water, k_B is the Boltzmann constant, $\sigma_{ice/water}$ is the surface tension between ice and water surface, h is the Planck constant, R is the universal gas constant, and T is the temperature. While the nucleation energy is more or less temperature-independent, the activation energy depends strongly on temperature and supersaturation with respect to ice. Thus, the nucleation rate J increases exponentially even at temperatures below −38°C, when the exponent becomes positive, by releasing activation energy. The resulting ice particle number concentration depends on the cooling rate / vertical velocity and freezing temperature (see Figure 2.3). The different vertical velocity ranges correspond to the three cirrus-generating mechanisms (synoptic, gravity waves, and convection) as introduced in Section 2.2. The ice number concentration increases with increasing vertical velocity and decreasing freezing temperature . As mentioned in Chapter 1, only a very high amount of aerosols can influence homogeneous ice microphysics under certain temperature and cooling rate conditions. Under high vertical updrafts and low formation temperatures more ice particles arise as predicted by the analytical solutions (see deviation of the symbols from the lines in Figure 2.3). Conditions with high aerosol concentration, low temperatures, and high updrafts are very rare in the atmosphere, but can occur, for example, due to the emission of a high amount of sulfuric acid during volcanic eruptions.

Supercooled liquid droplets are mostly composed of dissolved sulfuric acid (H_2SO_4), but could contain also other solution like organics or ammonium. Laboratory studies by Koop et al.

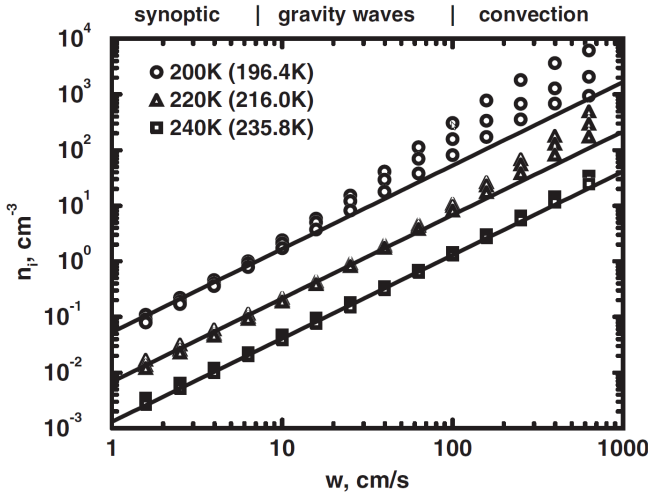

Figure 2.3: Cirrus ice crystal number concentration as a function of vertical velocity at different temperatures from analytical solution (lines) and from numerical simulations (symbols) using different aerosol particle concentrations and the Koop parametrization. Adapted from Kärcher and Lohmann (2002). Reproduced by permission of American Geophysical Union.

(2000); Koop (2004) pointed out that the freezing thresholds of different aqueous solutions are independent of their solutes. The homogeneous freezing threshold can be parametrized as a function of temperature and is widely used in models (see Figure 2.4). The necessary relative humidity with respect to ice relating to homogeneous freezing is between 140 and 170 % as confirmed in freezing chamber (Moehler et al., 2003) and field measurements (Krämer et al., 2009).

2.3.2 Heterogeneous freezing

The formation of ice particles with the involvement of insoluble substances is called heterogeneous freezing. These non-soluble substances act as IN and cirrus ice formation occurs in two different ways as shown in Figure 2.2. These processes are differentiated into various combinations of temperature and relative humidity with respect to ice (RH_{ice}), but occur only under conditions where RH_{ice} is above 100 %.

In general, the non-soluble IN facilitate the formation of stable ice embryos. Therefore, heterogeneous freezing is able to arise at lower RH_{ice} and always before a possible homogeneous freezing event at temperatures below −38°C. However, compared to homogeneous freezing this effect is not independent of the material properties and depends on size, morphology, solubility, epitaxial, and active site distribution of the IN (Kulkarni and Dobbie, 2010). These particle properties decrease the nucleation energy F_g in Equation 2.1 and raise the probability of ice formation at higher temperatures or lower supersaturation. The efficiency depends mostly on the IN type. Mineral dust or volcanic ash are good IN, whereas the efficiency of coated soot, for example, is only moderate. A simple parametrization between temperature and freezing threshold of IN is not possible as in the case of homogeneous freezing. It is rather the case that each type of IN has its own parametrization of temperature-depending freezing threshold (see Figure 2.4). Kärcher and Lohmann (2003) present a shifted activity method, which is derived from laboratory freezing experiments with mineral dust. The nucleation rate of homogeneous freezing is shifted to lower freezing thresholds for a specific IN. This method, extended to represent different IN types (see Figure 2.4), is implemented in the microphysical box model MAID (used in this study) to represent heterogeneous freezing.

In cirrus regions, the most likely freezing processes are immersion and deposition freezing (Kärcher and Lohmann, 2003). *Immersion freezing* occurs when an IN is immersed in a liquid particle. The solution droplet grows by water uptake below RH_{water} until ice formation starts, triggered by the IN surface. With respect to Figure 2.2, *deposition freezing* represents ice formation directly on the dry surface of the IN by deposition of water molecules. This is basically possible as soon as RH_{ice} is above 100 %, but the exact freezing threshold depends on the IN properties.

Normally, deposition freezing requires the presence of dry surfaces at which ice nucleates directly. These dry IN are probably very rare at cirrus level, because they act as cloud

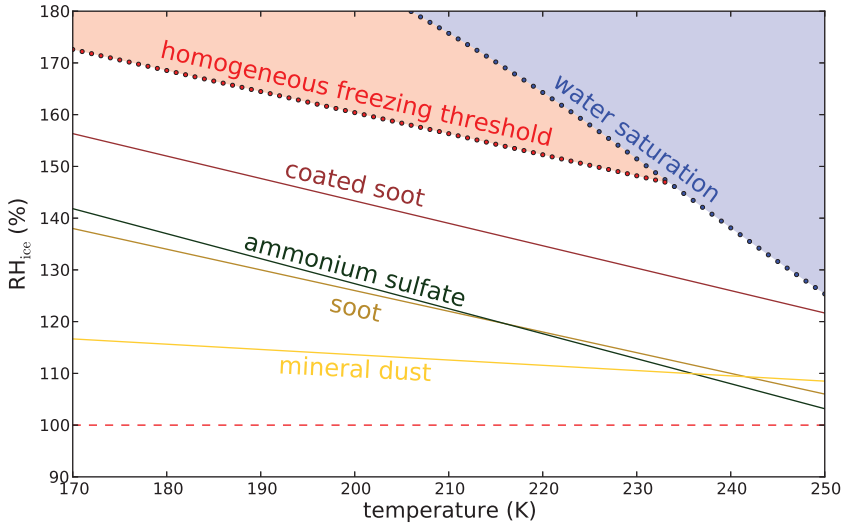

Figure 2.4: Freezing thresholds for heterogeneous freezing. Derived from AIDA chamber experiments (Mangold et al., 2005).

condensation nuclei (CCN) on the way from the Earth's surface to the upper troposphere and are therefore mostly removed from the atmosphere (Kärcher and Spichtinger, 2009). Nevertheless, very efficient dry IN can occur in the upper troposphere that permit deposition freezing as shown in Chapter 6, where deposition freezing is observed caused by volcanic ash from the Eyjafjallajökull eruption.

As already mentioned, heterogeneous freezing can change the cirrus evolution and microphysics. If an air mass including a small amount of IN is moderately cooled, heterogeneous freezing occurs before a potential homogeneous freezing event. These heterogeneously formed ice particles halt the increase in RH_{ice} by water uptake and ice particle growth. Thus, homogeneous freezing could either be totally prevented or leads to fewer homogeneously frozen ice particles. The total number of ice particles can therefore be reduced by the presence of IN up to a factor of 10. This effect is mentioned as the "negative Twomey effect" by Kärcher and Lohmann (2003), referring to the normal Twomey effect in warm clouds. The microphysical properties of the resulting cirrus cloud are changed and the extinction and optical depth are therefore reduced. A typical number concentration of IN at cirrus level in the northern hemisphere is about 0.01 to 0.03 cm^{-3} (Haag et al., 2003; DeMott et al., 2010). Heterogeneously formed ice particles with these typical concentrations cannot prevent homogeneous freezing, but probably modify the cirrus microphysical properties. This can be seen in Figure 2.5, where the ratio of ice crystal numbers from heterogeneous + homogeneous freezing to pure homogeneous

freezing is shown. The ice crystals number from heterogeneously plus homogeneously freezing is in most cases lower than the ice crystal number from pure homogeneous freezing for a wide range of vertical updrafts.

In some cases, more ice particles can be formed if the IN number is higher than the number of crystals that would appear from pure homogeneous freezing (see Figure 2.5). This may happen at low cooling rates corresponding to updrafts of 1 - 3 cm/s and warmer temperatures (where N_{ice} from homogeneous freezing is low, see Figure 2.3) . This is referred to as the "positive Twomey effect" and is believed to be inferior to the negative Twomey effect in general. However, an unusually high amount of volcanic ash particles (0.1 cm^{-3}) can produce a strong positive Twomey effect as will be shown in Chapter 6. Altogether, the roles of heterogeneous and homogeneous freezing in cirrus formation under different atmospheric conditions is one of the open questions in cirrus research.

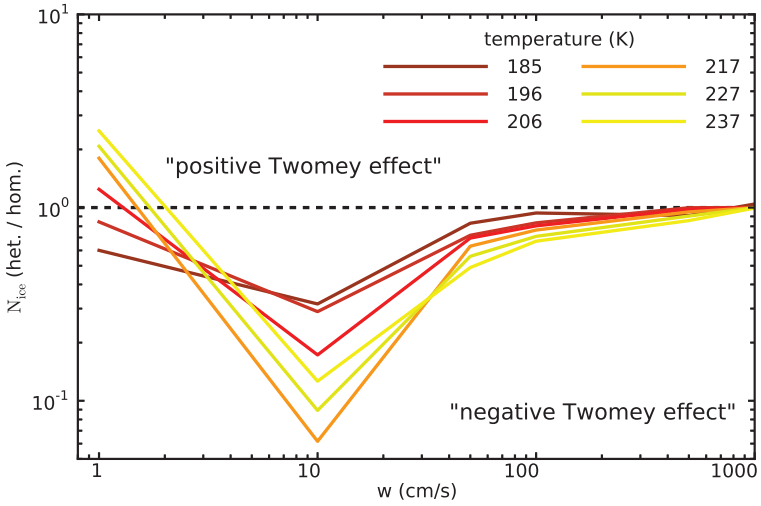

Figure 2.5: Ratio of ice crystal numbers from heterogeneously (IN number 0.01) plus homogeneously and pure homogeneously formation vs. vertical velocity w (cm/s) and six formation temperatures (Krämer and Hildebrandt, 2010). The calculations are performed by MAID (see Chapter 3).

3 Cirrus modeling with MAID

The kinetic microphysical box model MAID (Model for Aerosol and Ice Dynamics) is used for investigations of ice formation in comparison to lidar observation of cirrus clouds and is described further in this chapter. The detailed specification is given in publications of Bunz et al. (2008) and Gensch et al. (2008). MAID was originally developed at the Forschungszentrum Karlsruhe to simulate ice formation in the AIDA (Aerosol Interaction and Dynamics in the Atmosphere) chamber and then further developed at Jülich into a Lagrangian version to operate MAID along realistic air parcel trajectories in the atmosphere.

The model MAID calculates the equilibrium state of trace gas components between the gas phase, ice and aerosol particles. The microphysical ice processes implemented in MAID are as follows (see Section 3.1): First, heterogeneous freezing after Kärcher and Lohmann (2003) with variable numbers of IN in the deposition freezing mode is integrated. Second, homogeneous freezing after Koop et al. (2000) is included, which allows homogeneous freezing to occur after a heterogeneous freezing event. Further, microphysical processes consider diffusional ice growth, evaporation, sublimation and Lagrangian ice particle tracking. As part of this thesis, sedimentation of ice crystals was included after Spichtinger and Gierens (2009a). The box model is driven by temperature and pressure changes, either artificially generated or realistic atmospheric air parcel trajectories. The crucial parameters for ice formation are set in the model initialization (see Section 3.3).

In the next Sections the basic principle of MAID is outlined. Especially the process of sedimentation, which is now included as a new module in MAID, is described in more detailed in Section 3.1.3. The model initialization is explained in Section 3.3 and the trajectory preparation for use in MAID in Section 3.2. Finally, all relevant MAID output variables are described shortly in Section 3.4.

3.1 Basic principle of MAID

3.1.1 Aerosol particles

The liquid aerosol particles which are implemented in MAID are supercooled ternary solutions (STS) consisting of H_2O, H_2SO_4, and HNO_3. These aerosols are the most dominant type in the UT/LS region and play a primary role in homogeneous ice formation (see Section 2.3). MAID balances the amount of these three trace gases between the liquid and the gas phase

in dependence on temperature, saturation pressure, and the partial pressure gradient of each species. The total amount of all three species is fixed within one model run and is set in the model initialization. MAID uses a kinetic approach, whereby the mass flow is proportional to the partial pressure gradient and a kinetic factor depending on aerosol size, mean free path, diffusivity, and the accommodation coefficient of the gas species. If the partial pressure gradient is positive, the aerosol particle grows (condensation). It shrinks (evaporation) if this value is negative.

MAID represents a population of aerosols with the help of discrete size classes (size bins). All processes in MAID are applied for each size bin separately, which makes this model applicable for detailed investigations of cirrus evolution. These size bins are not fixed and are adjusted after each time step according to changes in the aerosol size distribution caused by underlying microphysical processes (i.e. condensation, evaporation, sublimation, and ice formation). This dynamical representation of aerosol size distribution is called "Lagrangian particle tracking".

3.1.2 Ice formation and sublimation

As outlined in Section 2.3 ice formation occurs both homogeneously and heterogeneously. In MAID the simulation of homogeneous ice nucleation follows the parametrization provided by Koop et al. (2000) and Koop (2004). This parametrization supplies ice nucleation rates depending on temperature, STS size, and the water activity, which can be expressed as the water saturation pressure. The ice nucleation rate yields a correlated ice particle number concentration depending on a certain cooling rate and by reaching a critical saturation pressure or freezing threshold. The number concentration of the resulting ice particles increases with decreasing temperature and increasing water activity (see Figure 2.3).

The heterogeneous ice formation is represented by the deposition freezing pathway (see Section 2.3). For this purpose the "shifted activity" parametrization from Kärcher and Lohmann (2003) is included in MAID. The same nucleation rate is used as homogeneous freezing, but only shifted to lower water activities or lower freezing thresholds depending on the type of IN. Different heterogeneous freezing thresholds varying with temperature are selectable (Gensch et al., 2008; Krämer and Hildebrandt, 2010), which differ concerning the critical relative humidity with respect to ice. Figure 2.4 presents the different freezing thresholds, which are implemented in MAID in dependence of the temperature. In addition to these fixed freezing thresholds, a manually adjustable value can also be used. These freezing thresholds for mineral dust, soot, ammonium sulfate, and coated soot are derived from freezing experiments at the AIDA chamber (Mangold et al., 2005; Moehler et al., 2005).

If a certain freezing threshold is reached in the model, the ice nucleation starts as long as all available IN are depleted. In this case, a further heterogeneous ice nucleation is suppressed. A possible homogeneous ice nucleation could start if the cooling rate and the relative humidity increase is large enough despite the favored growth of present ice particles. While a small

number of present ice particles reduce the relative humidity increase inefficiently, many ice particles take up larger amounts of water vapor and can suppress relative humidity increase despite of the further cooling. The resulting ice particles begin to sublimate when the relative humidity drops below saturation. The water vapor molecules evaporate from the ice particles with a rate depending on their partial pressures. The particle tracking and dynamical size classification are also applied for ice particles as well as for the liquid aerosols.

3.1.3 Sedimentation

Sedimentation of ice particles is an important factor in determining cirrus development and microphysical properties. Moreover, the falling of large ice particles is responsible for the fall-strikes (virga) which creates the typical feathery appearance of cirrus clouds. The ice particles leave the saturation area in which the cirrus was formed and reach mostly subsaturated air masses below. Large ice particles can survive very long times up to several tens of minutes in this subsaturated area and enlarge therefore the vertical extent of the initial cirrus. As cirrus ice particles trap aerosol particles and soluble trace gases, the sedimented ice particles sublimate and lead to a vertical redistribution of both water and these substances (Kärcher and Spichtinger, 2009). In addition, as mentioned in Section 1, the radiative forcing of cirrus is also very sensitive to the vertical structure. While small ice particles are predominately observed in the upper cloud layers where the cirrus is formed, larger ice particles typically occurs in the lower region due to sedimentation.

Classical box models like MAID are zero-dimensional, i.e. the considered air parcel is moved along a trajectory and ice formation is driven through temperature and pressure variations. Thus, without sedimentation all resulting ice particles are kept in this box. The impact of heterogeneous freezing could be overestimated by neglecting sedimentation because the ice particles formed from IN would stay in the box, can deplete water vapor efficiently, and grow to unlikely very large ice particles. Thus a small amount of IN could suppress further homogeneous nucleation as described in Spichtinger and Cziczo (2010). As sedimentation turned out to be an important factor, MAID has to deal with this process in order to reproduce cirrus clouds in the atmosphere. A two-moment (ice particle number and IWC) sedimentation scheme is adapted from the box model as described in Spichtinger and Gierens (2009a). First, a vertical extend of model box is defined with a typical value of $\Delta z = 50$ m. To calculate the sedimentation of ice particles a one-dimensional implicit advection scheme is used. The evolution of a quantity ψ (i.e. number concentration N or IWC) from time step t_{n-1} to t_n is described as:

$$\psi(t_n) = \psi(t_{n-1}) \cdot e^{-\alpha_\psi} + \frac{R_\psi}{\rho \cdot v_\psi} \cdot \left(1 - e^{-\alpha_\psi}\right), \tag{3.1}$$

where v_ψ represent the terminal velocity of the quantity ψ, $\alpha_\psi = \frac{v_\psi \cdot (t_n - t_{n-1})}{\Delta z}$ denotes the

Courant number for convergence of the partial differential equation, ρ is the density of air, and R_ψ represent the flux from above inside the box. The size dependent weighed terminal velocities v_N for the crystal number and v_{IWC} for the ice water content (or mass) are given as:

$$v_N = \frac{1}{N}\int_0^\infty f(m)v(m)\,\mathrm{d}m, \qquad v_{IWC} = \frac{1}{IWC}\int_0^\infty f(m)mv(m)\,\mathrm{d}m, \tag{3.2}$$

with the IWC distribution of ice particles $f(m)$ and the terminal velocity for single ice particle $v(m)$. The size dependent single particle velocity is given by a parametrization of Heymsfield and Iaquinta (2000). The approach of using two different terminal velocities ensure that larger ice particles fall out earlier than smaller ones, since the terminal velocity weighted by mass is always larger than that weighted by number.

The only unknown quantity is the flux into the box represented by R_ψ because the model box is isolated from the environment. There is no information about which ice processes or sedimentation rates occur above the box or at which position the model box is within the real cirrus cloud. The quantity R_ψ is estimated by assuming that the incoming flux of ice particles of the top of the box is a fraction of the outgoing flux at the bottom of the box:

$$R_\psi = \psi\rho v_\psi \cdot f_{sed}, \tag{3.3}$$

where the "sedimentation factor" f_{sed} represent the ratio of the flux through the top (f_{top}) divided by the flux through the bottom (f_{bottom}):

$$f_{sed} = \frac{f_{top}}{f_{bottom}}. \tag{3.4}$$

Then Equation 3.1 from the advection scheme can be expressed as:

$$\psi(t_n) = \psi(t_{n-1}) \cdot \left(f_{sed} + (1 - f_{sed}) \cdot e^{-\alpha_\psi}\right). \tag{3.5}$$

The strength of the sedimentation depends on the location of the model box within the cloud and can be adjusted with the help of f_{sed}. In case of $f_{sed} = 0$, there is no flux from above into the model box and all ice particles will fall out through the bottom. This represents a sink for ice particles and is related to a very strong sedimentation directly on the top of a cirrus cloud.

A sedimentation factor varying between 0 and 1 represents the normal case within a cloud layer:

$$\text{cloud top} : 0 < f_{sed} < 1 : \text{cloud bottom}. \tag{3.6}$$

There is a certain flux from above into the box, but the flux on the bottom is larger and produces a net loss of ice particles. The loss is decreasing for increasing sedimentation factor. No sedimentation occurs, if the factor reaches the value of one ($f_{sed} = 1$). The flux from above is then equal to the downward flux from the bottom and the number concentration as well as IWC is not affected by sedimentation. This is mostly the case directly for the lowest layers of the cirrus. A factor larger than one represent a generation of ice particles due to sedimentation. This behavior is not expected within a cirrus since it is unphysical. The region where net gain is meaningful is in a subsaturated region below the cirrus where sedimenting ice particle sublimate within the time. In this study the same sedimentation factors are used as in Spichtinger and Gierens (2009b) and Spichtinger and Cziczo (2010), yielding values of $f_{sed} = 0.5$ for simulation at the cloud top and $f_{sed} = 0.9$ for simulations within the cloud.

As mentioned above sedimentation changes the cirrus development and its microphysical properties. Figure 3.1 illustrates this effect by applying three MAID runs with varying sedimentation strength allowing for homogeneous freezing with vertical updraft of 0.1 m/s. Panel a) shows $\mathrm{RH_{ice}}$ versus time in case of considering no ($f_{sed} = 1$, blue), slight ($f_{sed} = 0.9$, dashed red), and strong ($f_{sed} = 0.5$, dotted red) sedimentation. Panel b) displays the total number concentration of ice particles for the three cases. All three simulations are equal until reaching the homogeneous freezing threshold of 152 % $\mathrm{RH_{ice}}$ at a time of around 80 min, producing a moderate amount of ice particles (0.16 $\mathrm{cm^{-3}}$). The strong negative slope in $\mathrm{RH_{ice}}$ is caused by the growth of ice particles. In case of no sedimentation, $\mathrm{RH_{ice}}$ stays almost constant near the thermodynamic equilibrium of 100 %. The number concentration decreases slowly due to the adiabatic extent of the air parcel, but the total number in the model box stays constant. In case of sedimentation, large ice crystals are removed from the air parcel and the ice number concentration decreases stronger. Thus, the remaining ice particles cannot reduce efficiently the water vapor supersaturation by ice growth and thus the relative humidity increases again. In case of strong sedimentation (near cloud top), the homogeneous freezing threshold is reached again and new ice crystals are formed. The second freezing event produces less ice crystals than the first, because of a slightly smaller relative humidity rate ($\frac{\mathrm{dRH_{ice}}}{\mathrm{dt}}$). The stronger the sedimentation the faster is the occurrence of further freezing events, as can be seen in Figure 3.1 when comparing slight and strong sedimentation.

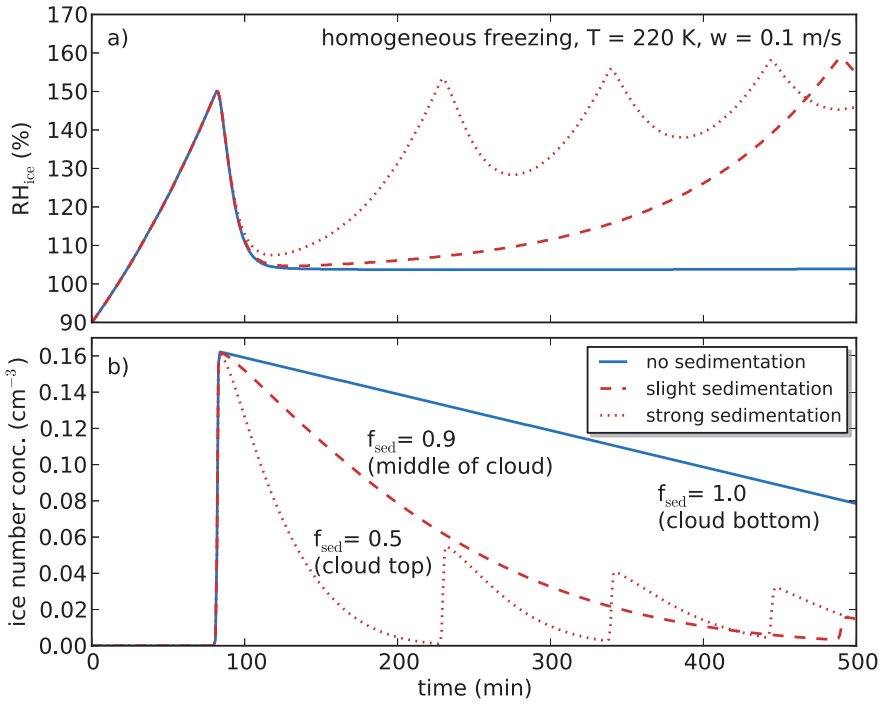

Figure 3.1: Impact of sedimentation on cirrus evolution on a) relative humidity with respect to ice (RH_{ice}), b) ice crystal number concentration considering homogeneous freezing with an initial temperature of 220 K and a constant cooling rate due to an updraft of 0.1 m/s.

3.2 Trajectory preparation

In this study, MAID is run along atmospheric air parcel trajectories. For this purpose we used the trajectory module of the Chemical Lagrangian Model for the Stratosphere (CLaMS) (McKenna et al., 2002). Trajectories are calculated - using a hybrid vertical coordinate zeta as reported in Konopka et al. (2007) - based on ECMWF analyses data with a vertical resolution of around 600 m in the altitude range from 7 to 12 km, a horizontal resolution of 1 x 1 degree, and time resolution of 6 h. Trajectories are calculated from the site of the lidar (Jülich) backwards in time to locate where the measured air mass originated.

Along the trajectory coordinates, temperature, pressure and humidity are provided which are necessary for box model simulations. The ECMWF data does not well represent small-scale temperature and pressure fluctuations caused by gravity waves as reported in Schroeder et al. (2009). Especially mesoscale fluctuation with wavelengths smaller than the ECMWF grid resolution are not represented in the data. Hoyle et al. (2005) showed that these natural adiabatic fluctuations due to atmospheric wave activity are crucial for the formation of ice crystals and for the resulting ice particle properties (number size distribution and IWC).

The integration and implications of temperature fluctuations in MAID is shown in the next subsection.

For cirrus simulations, it is verified that the temperature along the trajectory remains below −38°C. Above this temperature immersion freezing of water drops, which is not implemented in MAID, could exist in addition to direct ice nucleation by deposition freezing, which is the formation mechanism of cirrus clouds. MAID is started at the warmest trajectory point (implying cirrus free conditions) to save computational time and to avoid starting with a supersaturation over ice. Starting the model with a relative humidity above 100 % overestimates the ice production. This cut of trajectories also reduces increased uncertainties due to multiple cirrus life cycles (formation and sublimation etc.) within the model simulation.

3.2.1 Temperature fluctuations

For the reproduction of observed cirrus clouds it is essential to include temperature fluctuations caused by atmospheric waves in the simulations (Hoyle et al., 2005). Here, we superimpose a Gaussian distributed temperature noise with a respective standard deviation (σT) to the trajectory temperature. The typical peak-to-peak fluctuation frequency is around 10 minutes and reaches frequencies up to 10 h^{-1} as reported in Hoyle et al. (2005). Thus, all quantities described by the trajectory are linearly interpolated from 1 hour to 10 minutes time resolution. After that, a Gaussian distributed offset is added on temperature and pressure every time step. Finally, the trajectory is further interpolated with cubic spline function to 1 minute time resolution, which can applied as MAID input. The cubic spline interpolation produces a more realistic behavior of the temperature and pressure progress than a linear interpolation as shown in Appendix B.2. All these steps make the trajectory and the model behavior more consistent with real atmospheric conditions. Nevertheless, this Gaussian temperature distribution is arbitrary and generates a somewhat random behavior of ice formation. For that reason, we made several (mostly 5) model runs for each trajectory, each with newly generated temperature fluctuations. The result of the MAID runs is only considered to be meaningful and robust if more than 50 % of the model runs yield a similar result, i.e. similar ice particle number concentration and size distribution.

The temperature amplitude (σT) constitutes an important quantity in ice formation models. The microphysical quantities depends strongly on the magnitude of these fluctuations. Figure 3.2 shows idealized MAID sensitivity runs for one set of temperature fluctuations with different temperature amplitudes (same as Figure 3.1, blue line; no sedimentation). Four different temperature amplitudes (0, 0.5, 1.0, 2.0 K) are superimposed to the temperature and corresponding pressure as shown in panel a). Panel b) shows RH_{ice} values for all simulations and it is noticeable that the largest differences between the simulations happen during the first 100 min where ice nucleation occurs. The higher the temperature fluctuation amplitude is, the earlier ice formation starts by reaching the desired freezing threshold in comparison to the

undisturbed case (black line). Panel c) shows the corresponding number concentrations of ice particles and it is obvious, that also higher ice number concentration are reached with higher fluctuation amplitudes. However, due to larger cooling rates more ice particles are created (see also panel c)). After ice nucleation the development of all four cirrus clouds is similar but with a certain offset in ice number concentration and mean radius. By comparing ice number and size of the undisturbed and the 2 K amplitude case, the ice number differs by two orders of magnitude and the size by a factor of 3. This shows, that ice formation is very sensitive to the temperature fluctuation amplitude and that thus an estimate as accurate as possible is crucial for cirrus modeling.

Here, mesoscale temperature fluctuation are computed after a parametrization provided by Gary (2006), where the temperature amplitude σT depends on altitude, geographic latitude, longitude and season. This parametrization is based on hundreds of aircraft microwave temperature profiler measurements, which are analyzed for vertical displacement of isentrope surfaces. Under the assumptions that air parcels flow along isentrope surfaces and change temperature adiabatically while undergoing altitude displacements, it is possible to compute mesoscale temperature fluctuations that are not present in synoptic scale back trajectory temperature histories (Gary, 2006). By using a statistical analysis of surface displacements, the full-width mesoscale fluctuation amplitude (MFA) in m is given by:

$$MFA = (112. - 1.21 \cdot lat + 2.2 \cdot wint \cdot lat + 29. \cdot top) \cdot (\frac{p}{58.85})^{-0.4} \tag{3.7}$$

where p is the pressure in hPa, top is the underlying topography roughness varying from 0 to 1, lat is the latitude in degree and wint is the seasonal parameter called the "wintriness". This parameter varies also from 0 to 1 depending on the day of the year (doy) and is represented by:

$$wint = \frac{1}{2} \cdot \left(1 + sin\left(\frac{\pi}{2} \cdot \frac{doy - 295}{365}\right)\right). \tag{3.8}$$

The temperature amplitude σT in K is given by converting half of the full-width mesoscale fluctuation amplitude in meter to temperature by assuming dry adiabatic conditions with a temperature lapse rate of 0.01 K/m:

$$\sigma T = \frac{1}{2} \cdot 0.01 \cdot MFA. \tag{3.9}$$

The corresponding pressure fluctuations, consistent with the air parcels movement, are calculated via temperature dependent adiabatic expansion. The topography parameter is the only unknown quantity in this parametrization. This value reaches from 0 for very flat regions like the ocean, over 0.4 for flat land, 0.6 for coastal regions, and 0.6 to 1.0 for

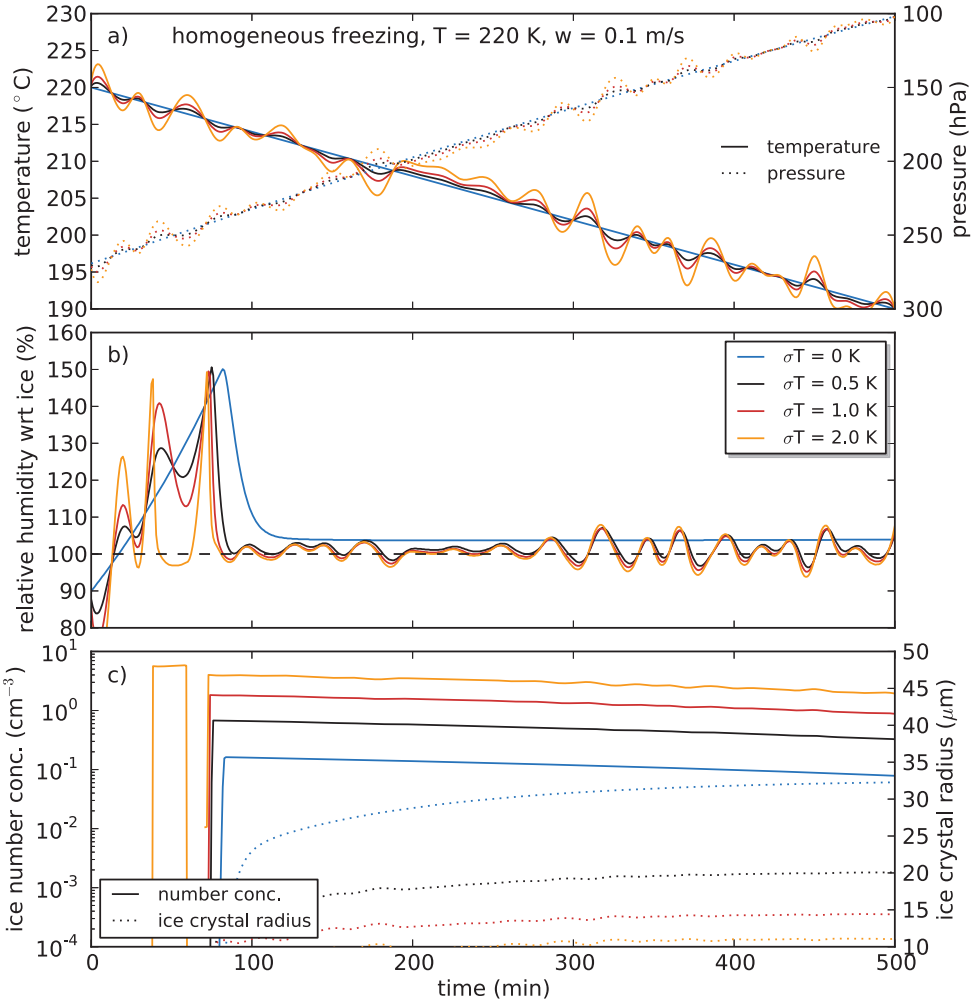

Figure 3.2: Influence of temperature amplitudes σT on microphysics and evolution of a homogeneously frozen cirrus cloud (blue curve: same scenario as Figure 3.1): a) adiabatic temperature and pressure fluctuations b) relative humidities with respect to ice, and c) resulting ice particle concentrations and mean radii.

continental mountains (Gary, 2006). The trajectories used in this study are examined where they originates and values appropriate for underlying surface are chosen. Typical amplitude values for mesoscale temperature fluctuations in mid-latitudes in the near of Jülich at cirrus level are around 0.5°C.

3.3 Model initialization

MAID is initialized separately for each trajectory or respective model run. In the initialization file, aerosol and IN properties (i.e. freezing threshold, aerosol / particle size, concentration etc.), and trace gas concentrations are set.

First, the time resolution of the trajectory is chosen. Then, the freezing type has to be selected as either pure homogeneous freezing or heterogeneous with possible further homogeneous freezing. The size resolution of the size distributions of the liquid aerosol and ice particles is then defined. Normally, the number of size bins are fixed at a value of 40. A higher value would increase the computational time of the model runs considerably. The existing background aerosol particles concentration is normally set to 300 cm^{-3}, the typical value of soluble supercooled aqueous sulphuric acid particles in the upper troposphere (see Section 2.3). The log-normal particle size distribution is defined over the mean radius (typical value of 200 nm) and the width of the distribution given as the standard deviation (typical value of σ =600 nm). The aerosol composition, consisting of H_2O and H_2SO_4, is defined in the initialization as well, where HNO_3 is not considered in this study. Further important parameters are the microphysical properties of IN, where the number concentration, minimum and maximum radius, the width of the log-normal size distribution, and the freezing threshold has to be specified. The freezing threshold can be either selected by a temperature based parametrization of a certain species or fixed as a certain value as described in Section 3.1.2. The IN properties are either available by measurements or have to be assumed. The parameter concerning sedimentation has to be specified and a sedimentation factor of 0.9 (see Section 3.1.3) is assumed for the most model runs. This is a typical value for most of the trajectories moving within a cirrus cloud layer with a normal vertical extent of few 100 m.

The trace gas concentration of H_2O is one of the most important quantity with respect to ice formation in the atmosphere. MAID works with a constant value of water vapor during the whole simulation. The amount of H_2O can be either determined by measurements (e.g. aircraft or balloon soundings) or is provided from the trajectory itself. In most cases there are no direct measurements available and the trajectory humidity based on ECMWF data has to be used. The water vapor mixing ratio should be nearly constant along each trajectory (no mixing with other air parcels). The length of the trajectories is set to be smaller than 48 hours -which is less than the typical timescale of air parcel mixing- to minimize the influence of air masses with different amounts of water vapor. Additionally, trajectories have to be checked for strong vertical winds or passing convective systems which can imply mixing. Moreover, ECMWF

data often show a dry bias of H_2O in the upper troposphere (Luo et al., 2008). The amount of the trajectory water vapor has to be checked for consistency with other observational data, e.g. radiosondes as described in Section 4.4.1. The initialized water vapor is normally set to the mean mixing ratio along each trajectory, but could be further shifted if general discrepancies appear between radiosonde data and the corresponding ECMWF data.

3.4 Model output

MAID stores all microphysical quantities of one model run every minute along the trajectory. These are the concentrations of H_2O and HNO_3 in the gas, liquid, and ice phase, where the ice phase of H_2O represents the IWC. The gas phase H_2O is related to the relative humidity with respect to ice. Furthermore, the total number concentration of aerosol and ice particles is given. The whole size distribution of resulting ice particles is provided by MAID as well as three mean radii, which are explicitly explained in the Appendix B.1. First, the count median radius (CMR), which marks the radius with the largest amount of particles. Then, the surface mean radius or effective radius, which represents the mean cross section of an ice particle ensemble reacting with radiation. This radius is therefore important to relating MAID results to optical measurements with the lidar, or to calculate extinction values of ice particles. Finally, the mass mean radius, implying the particle size where the average mass of the distribution is, is provided. This radius is typically larger than the mass median radius (MMR) where the most of the mass contribute to the distribution. MAID also provides extinction values of resulting ice particles calculated using Equation 4.25.

4 Lidar measurements

Lidar stands for light detection and ranging and is an active remote sensing method for investigations of atmospheric molecules and particles that scatter light. An overview of the lidar principle is given in Section 4.1, while a more detailed description of light scattering processes in the atmosphere can be found in the Appendix A.1. The lidar instrument used for this work is introduced in Section 4.2. The different aspects of molecular and particle scattering and determination of particle optical properties are introduced in Section 4.3. Finally, the cirrus detection method and the evaluation of cirrus properties like ice water content (IWC) or optical depth is explained in Section 4.4.

4.1 The LIDAR principle

A lidar system mainly consists of a transmitter and a receiver. The transmitter is usually a pulsed laser which emits monochromatic, linear polarized, and coherent electromagnetic

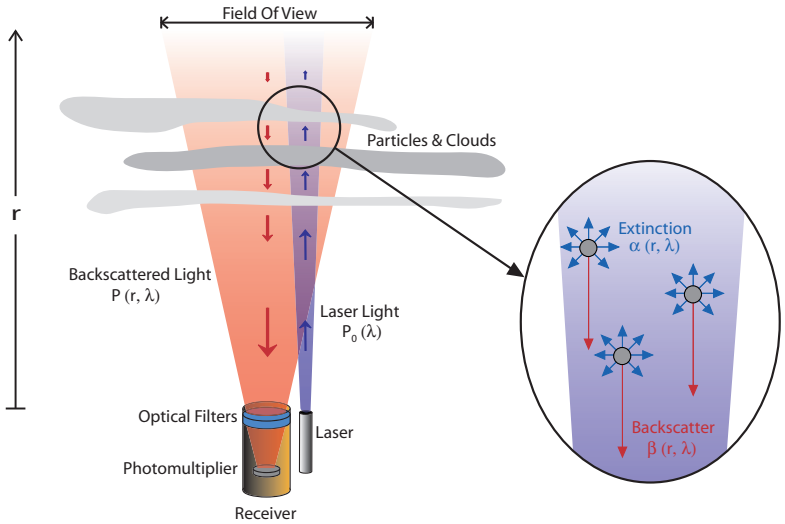

Figure 4.1: Lidar principle with laser, detection unit, the laser pulse (blue shaded), and the detection field of view (FOV) (red shaded). In addition, the scattering process is illustrated on the right.

radiation vertically from the ground into the atmosphere (see Figure 4.1). The laser wavelength is typically in the spectral range of ultra violet, visible, or near infrared. Aerosol and cloud particles as well as air molecules in the laser beam interact with the radiation by scattering and absorption of the laser light. The scattering process related to the molecules occur as Raman and Rayleigh scattering, while particular scattering relates to the aerosol and cloud particles, if the size of the scatterer is in the same order as the wavelength λ of the incident light.

The receiver detect the backscattered light and is composed of a telescope to focus the backscattered light to the detector. The range r of the scatterer from the instrument can be determined by a simple time measurement Δt between emitted laser pulse and detected backscattered light with the relation $\mathrm{r} = \mathrm{c} \cdot \Delta\mathrm{t}/2$, with c speed of light. This basic principle is shown in Figure 4.1 with the laser pulse in blue and the telescope or the detector field of view (FOV) in red. The laser and detection unit are shown on the bottom. All molecules and particles, which are within the laser beam can scatter the light and all backscattered photons which are within the FOV can reach the detector.

The backscattered light intensity $\mathrm{P(r,\lambda)^p}$ detected by the lidar is described by the lidar equation (Eq. 4.1), where the intensity depends on the range r from the receiver to the scattering volume, the wavelength of the laser, and the polarization of light. Moreover, the lidar equation contains different system parameters like the geometry of the detection system and can be written in the notification of Wandinger (2005) as:

$$P(r,\lambda)^p = P_0(\lambda)^p \underbrace{\frac{O(r)}{r^2}}_{\mathrm{I}} \underbrace{E(\lambda)}_{\mathrm{II}} \underbrace{\beta(r,\lambda)^p}_{\mathrm{III}} \underbrace{exp\left[-2 \int_0^r \alpha(\tilde{r},\lambda)\,\mathrm{d}\tilde{r}\right]}_{\mathrm{IV}} \tag{4.1}$$

where

λ	=	wavelength of the emitted laser light,
r	=	range from the lidar receiver (m),
p	=	polarization of laser light,
$P(r,\lambda)^p$	=	the received power,
$P_0(\lambda)$	=	the emitted pulse power,
$O(r)$	=	the overlap function,
$E(\lambda)$	=	system efficiency (m^3),
$\beta(r,\lambda)^p$	=	the backscatter coefficient ($\mathrm{m}^{-1}\mathrm{sr}^{-1}$), and
$\alpha(r,\lambda)$	=	the extinction coefficient (m^{-1}).

The lidar signal depends on four terms that attenuate the emitted laser power $\mathrm{P_0(\lambda)^p}$.

Term I represents the measuring geometry. The emitted laser power decreases proportional to the inverse squared range, due to the detection of backscattering from a fixed solid angle (FOV). The function $O(r)$ describes the fraction of the overlap between the laser beam and

the telescope FOV. Thus, the function increases from 0 at ground to 1 at range level, where a complete overlap is reached.

Term II includes the range independent parameters of the lidar system and is called the system efficiency. The system efficiency is specified by:

$$E(\lambda) = \frac{c \cdot t_{pulse}}{2} \; A \; \eta(\lambda)^p \tag{4.2}$$

where

$\eta(\lambda)^p$ = transmission efficiency of the lidar receiver,
t_{pulse} = the temporal laser pulse length in (s), and
A = the area of the receiver telescope (m^2).

The optical transmission efficiency η of the lidar receiver cover the detector efficiency, optical transmission from telescope to the detector, and filter efficiency. This quantity is mostly unknown. However, the constant system parameter can be estimated experimentally.

Term III denotes the backscatter coefficient $\beta(\mathrm{r},\lambda)^{\mathrm{p}}$ from range r and polarization p. The backscatter coefficient describes the capability of a certain medium to scatter radiation back into the incident direction. Only the backscatter event with an angle of about 180° can be detected by the receiver (Figure 4.1, red arrows).

Term IV describes the transmission of light along the path through the atmosphere from the laser back to the receiver. The light is attenuated by scattering and absorption processes along this path. All scattering directions which are not directed to the detector, are combined to an extinction of the incident beam (Figure 4.1, blue arrows). The extinction characterizes the exponent of the well known Lambert-Beer's law with the exponential dependence on the optical depth (integration of extinction coefficient along the optical path). The extinction coefficient depends on concentration, shape, size, orientation, and chemical composition of particles and molecules as well as the wavelength of the incident radiation. The factor of two in Term IV arises from the fact that the light pass the optical path from laser to scattering volume twice.

The two quantities, the extinction coefficient α and the backscatter coefficient β are coupled and contain information about the optical properties of the measured air mass. In the atmosphere, where different scattering partners (molecules or particles) in the measurement volume exists, the extinction and backscatter coefficient cannot be addressed to one single object with one shape. The lidar measures the mean optical quantities of all scattering partners in the measurement volume. Both coefficients can be split up into one part belonging to interaction with air molecules (Raman and Rayleigh scattering), marked as (ray), and one part belonging to the scattering of particles and aerosols, marked as (aer).

The extinction and backscatter coefficients are denoted as:

$$\alpha(r,\lambda) = \alpha_{ray}(r,\lambda) + \alpha_{aer}(r,\lambda) \tag{4.3}$$

and

$$\beta(r,\lambda) = \beta_{ray}(r,\lambda) + \beta_{aer}(r,\lambda). \tag{4.4}$$

Another important quantity derived from lidar measurements is the depolarization. The polarization of the incoming laser light can be changed by the scattering process in dependence of particle shape. The amount of polarization changes is called depolarization. Thus, the depolarization is a measure of the asphericity of the scattering particles. The determination of the depolarization is done by measuring usually two polarization states of backscattered light of the measurement volume. This quantity is therefore called the volume depolarization (δ_{vol}). The depolarization and its determination is explained in more detail in Section 4.3.4 and in Appendix A.1.

The retrieval of $\alpha(r)$, $\beta(r)$, and $\delta_{vol}(r)$ from the lidar measurements is described in Section 4.3.

4.2 Leo-Lidar instrument

The mobile elastic backscatter lidar instrument named Leo-Lidar is used for cirrus cloud or aerosol observation. The commercial lidar instrument is manufactured by Leosphere under the type designation ALS 450. The integrated Nd:YAG laser emits frequency tripled laser pulses at a wavelength of 355 nm with a duration of 4 ns, and a frequency of 20 Hz. The laser pulse duration defines the range resolution and results in a raw data resolution of 1.5 m. Normally, detector and electric noise as well as background light in the same wavelength reduce the range resolution to 30 m during night and 60 m during day time due to signal averaging. The best achievable time resolution is 0.5 minutes (average over 600 single laser pulses) during nighttime and 5 minutes during daytime (average over 6000 single laser pulses). This values are the lower limits for deriving optical particle properties and can be larger depending on atmospheric conditions (i.e. aerosol loading etc.). The lidar head including the laser and receiver can be tilted. The receiver telescope has a diameter of 15 cm with a field of view of around 1.5 mrad. The overlap region between laser and FOV is therefore at range levels from 52 m (first overlap) to 510 m (full overlap). The whole overlap function $O(r)$ is determined in the Appendix A.4. The altitude coverage of the Leo-Lidar is 0.05 to 15 km, where the detector starts to receive backscattered photons (first overlap) and the upper limit depends on a sufficient signal to noise

ratio. All specifications and properties are combined in Table A.1 in the Appendix.

The laser emits parallel polarized light. Two detectors measure the parallel and the perpendicularly polarized backscattered light in photon counting as well as analogous mode. The depolarization of the scattering particles can be measured with this two detectors using the methods presented in Section 4.3.4. The analogous signal of each detector is used for the high backscatter intensity normally within the denser and particle rich lower part of the atmosphere and the photon counting signal for the weaker backscattering of the higher atmosphere including cirrus clouds. To get a full backscatter profile both signals are "glued" together in an altitude range where both signals are valid (cloud free range between 3 and 6 km).

Only the polarization independent backscatter and extinction coefficient is usually used to determine characteristics of cirrus clouds. To omit the polarization dependency p of the backscatter / extinction coefficient in the lidar equation, the total backscatter signal has to be determined. This means, the summation of all measured polarization states of the backscatter intensity, which are parallel and perpendicular in case of the Leo-Lidar, to a total signal $P(r,\lambda)$. This cannot done directly by summation because the different system efficiency has to be taken into account. The explicit realization is described later in Section 4.3.4.

For the laser wavelength of 355 nm the absorption of molecules and aerosols in the troposphere and lower stratosphere can be omitted. Thus, only scattering contributes to the measured backscatter and extinction coefficient. The amount of detected Rayleigh scattering depends strongly on the detection system and the used filters of the lidar instrument. For a full width half maximum (FWHM) of the interference filter between 0.2 and 1.0 nm only the Cabannes line, which is the pure inelastic part of the spectrum without rotational Raman lines (see Appendix A.1), contribute to the detected Rayleigh scattering. The Leo-Lidar instrument has

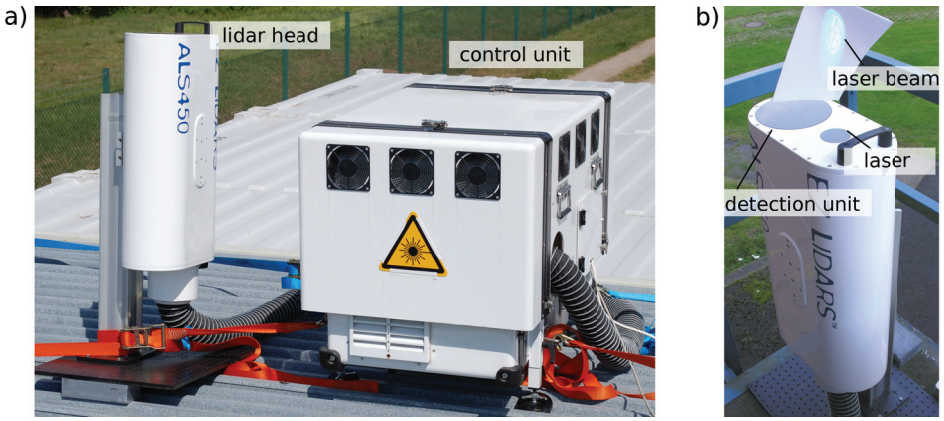

Figure 4.2: a) Picture of the mobile backscatter Leo-Lidar (Leosphere ALS 450) with lidar head and lidar control box. b) Picture of lidar head with black small laser window, large detection window, and the outgoing widened laser beam.

an interference filter with a FWHM of 0.5 nm. Thus, only the impact of the Cabannes line is considered as molecular scattering.

In Figure 4.2, pictures of the mobile backscatter lidar are shown. The laser is placed behind the small black filter window at the lidar head (visible in panel b). Moreover, the telescope with both detectors and a polarization beam separation unit is located behind the larger black window. The laser control, laser cooling system, and data acquisition is placed in the lidar control box (visible in panel a) of Figure 4.2). The whole system is weather protected with the help of the white casing and an additional cover. This lidar instrument is therefore suitable for 24/7 outdoor use and can be easily transported through the compact setup. This allows the support of aircraft measurement campaigns from the ground.

4.3 Retrieval of lidar optical parameters

4.3.1 Particle backscatter coefficient

Different methods are available to determine α and β, which depend on the lidar system. In case of an elastic backscatter lidar, which is used in this study, both coefficients have to be determined from only one parameter, the detected backscatter intensity P(r). Therefore, the lidar equation 4.1 is under-determined and the particle backscatter as well as extinction coefficient cannot be derived independently. Klett (1981) and Fernald (1984) developed a stable analytical solution for inversion of the under-determined lidar equation. This method is referred to as Klett-Fernald algorithm. In order to use the Klett-Fernald algorithm a further assumption is necessary. The lidar ratio L_{aer} (see Eq. 4.5) which represents the fraction between α_{aer} and β_{aer} has to be assumed. A Raman lidar by contrast provide an independently derived extinction profile with the help of the inelastic scattering of molecular nitrogen. The right choice of L_{aer} is very important and is assumed to be constant in height for the use of the Klett-Fernald algorithm. This is normally not the case due to various optical properties of aerosols in the atmosphere. However, it is possible to assume one L_{aer} constant for a particular height with mainly one type of aerosols as for instance volcanic ash or ice particles with similar microphysical properties.

$$L_{aer} = \frac{\alpha_{aer}(r)}{\beta_{aer}(r)}. \tag{4.5}$$

For further considerations, the lidar equation 4.1 is simplified by assuming the overlap function equal to one (O(r) = 1). This means full overlap of FOV and laser beam. The wavelength dependency is also neglected by using only the wavelength of the used lidar system (λ = 355 nm). In following the backscatter coefficient is derived from the total backscatter signal $P(r) = P^{\parallel}(r) + P^{\perp}(r)$ and the polarization index p is neglected.

Thus, Equation 4.1 results in

$$P(r) = \frac{P_0}{r^2} \cdot E \cdot [\beta_{ray}(r) + \beta_{aer}(r)]\, exp\left[-2 \int_0^r \alpha_{ray}(\tilde{r}) + \alpha_{aer}(\tilde{r})\, \mathrm{d}\tilde{r}\right]. \tag{4.6}$$

Equation 4.6 can be written as differential equation by applying the logarithm and the derivative according to the height r (Klett, 1981, 1985):

$$\frac{d}{dr} ln(P(r)r^2) = \frac{d}{dr} ln\left(\beta_{ray}(r) + \beta_{aer}(r)\right) - 2\left[\alpha_{ray}(r) + \alpha_{aer}(r)\right], \tag{4.7}$$

where $\mathrm{P(r)} \cdot \mathrm{r}^2$ is called the range corrected signal. Equation 4.7 has the structure of a Bernoulli differential equation and is solvable for β_{aer} as:

$$\beta_{aer}(r) = \frac{A(r_{ref}, r)}{N(r_{ref}, r)} - \beta_{ray}(r) \tag{4.8}$$

with the numerator $\mathrm{A(r_{ref},r)}$ and denominator $\mathrm{N(r_{ref},r)}$:

$$A(r_{ref}, r) = P(r)\ exp\left[-2\ (L_{aer} - L_{ray}) \int_{r_{ref}}^r \beta_{ray}(\tilde{r})\, \mathrm{d}\tilde{r}\right] \tag{4.9}$$

$$N(r_{ref}, r) = B\ -\ 2\ L_{aer} \int_{r_{ref}}^r A(r_{ref}, \tilde{r})\, \mathrm{d}\tilde{r}. \tag{4.10}$$

The denominator $\mathrm{N(r_{ref}, r)}$ contains the integration constant $\mathrm{B = P(r_{ref})/(\beta_{ray}(r_{ref}) + \beta_{aer}(r_{ref}))}$ which includes the known and assumed initial conditions of the reference hight $\mathrm{r_{ref}}$. The particle backscatter coefficient of this reference height is assumed and should be preferably near to the true value in this range of the atmosphere. Thus, only altitude regions with notably low particle loading are chosen, where the particle backscatter coefficient is close to zero and smaller than the Rayleigh backscatter coefficient ($\beta_{\mathrm{aer}} \ll \beta_{\mathrm{ray}}$). Below and above free tropospheric clouds this assumption is valid for wavelengths $\lambda \leq 532$ nm as reported in Ansmann (2002) and a low value of $1 \cdot 10^{-8}\ \mathrm{sr^{-1}m^{-1}}$ is chosen as a first guess. Normally the signal is very noisy in higher altitudes and should be smoothed and averaged before use in the integration constant. Thus, the reference height is practical not a single height, but rather a mean reference value of a certain altitude range. Without this, the Klett inversion gets instable. If the reference height is chosen directly below the cloud, the Klett inversion is done by a forward integration. In case of a reference height above the cloud, a backward integration is used and the integrals in the Klett inversion (Eq. 4.8) are reversed. Klett (1985) showed the numerical stability of the

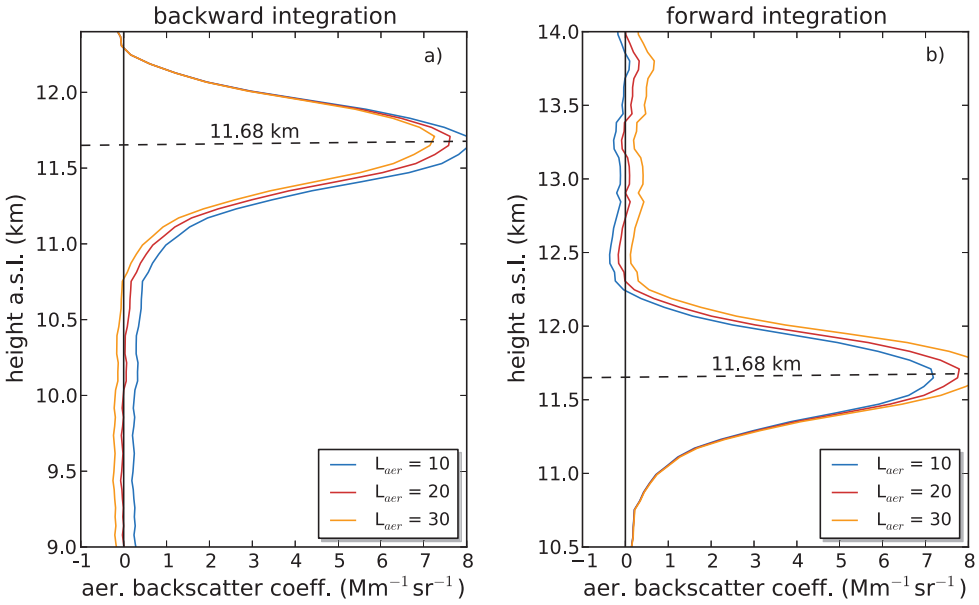

Figure 4.3: Profiles of backscatter coefficients for different lidar ratios L_{aer} from a cirrus cloud profile on 10.08.2011 at a height of 11.68 km. Averaged backscatter data from 07:00 to 08:30 UTC. Panel a) results of the backward integration, panel b) results of the forward integration.

integration is only given for the backward integration considering signal noise and incorrect lidar ratios. The Klett inversion is applied several times by adjusting the first guess of particle backscatter coefficient in the reference height. The iteration procedure converged very fast to the best solution and is appropriate after 3 iterations in general.

The right choice of the lidar ratio L_{aer} is important as described above. For the right lidar ratio forward and backward integration should result in the same particle backscatter profile for a cirrus cloud. Therefore, the combination of backward and forward integration can be used to estimated and validate the assumed lidar ratio. Figure 4.3 shows profiles of backscatter coefficients for a cirrus cloud at 11.68 km altitude. Profiles are derived with different lidar ratios with a reference height around 13 km for backward integration shown in panel a) and with a reference height around 10 km for forward integration in panel b).

The shape of the cirrus backscatter profile is similar in both cases, but varying with different lidar ratios. The best choice for the lidar ratio by applying the backward and forward integration is a value of 20 sr by obtaining a backscatter coefficient close to zero below and above the cirrus. While a lower lidar ratio of 10 sr results in an overestimation below the cloud in case of backward integration, a value of 30 sr results in negative values of backscatter coefficient. In case of forward integration this behavior regarding over- and underestimation with respect to the lidar ratio is vice versa. Therefore, the determination of true lidar ratio is only possible, if

forward and backward integration provide similar profiles.

The required Rayleigh backscatter (β_{ray}) and extinction (α_{ray}) coefficients can be estimated using the molecular particle density in range r. This is done with the ideal gas law and the knowledge of the temperature and pressure profile along the lidar FOV (see Eq. A.13 in the Appendix). Both values, the Rayleigh backscatter and extinction coefficient are important for the analysis of lidar data and has to be known as accurate as possible to separate the molecular and particle scattering from the total backscatter signal. In Section 4.4.1, the determination of backscatter and extinction coefficient profiles based on ECMWF data, radiosonde data, and a standard atmosphere profile is discussed.

Overall, the Klett-Fernald algorithm provide the particle backscatter coefficient in the range r to the lidar. For a realization onto a computer the height has to be exchanged into explicit height bins $\mathrm{r_i}$ and the integrals into sums.

4.3.2 Particle extinction coefficient

Cirrus cloud properties can be mainly determined with the particle extinction coefficient α_{aer} which cannot be derived directly from the lidar data. However, the extinction coefficient can be calculated from the definition of the lidar ratio (Eq. 4.5), the particle backscatter coefficient provided by the Klett method, and the assumed lidar ratio:

$$\alpha_{aer}(r) = L_{aer} \cdot \beta_{aer}(r). \tag{4.11}$$

The optical depth or optical thickness is the integral over the extinction along a certain optical path as shown in Eq. 4.12. The optical depth is therefore a measure for the transparency of a atmospheric particle or cloud layer. The optical depth is a dimensionless quantity and represent the exponent in the Lambert Beer's law. Greater optical depth is associated with stronger scattering along the optical path and therefore less transmittance of light. In case of cirrus clouds the optical path goes from cloud base height denoted as $\mathrm{r_{base}}$ to the top height $\mathrm{r_{top}}$:

$$\tau = \int_{r_{base}}^{r_{top}} \alpha_{aer}(\tilde{r})\,\mathrm{d}\tilde{r}. \tag{4.12}$$

4.3.3 Errors of particle backscatter and extinction coefficient

The error of the particle backscatter coefficient in range r can be calculated with the normal Gaussian error propagation from Equation 4.8. Three different quantities, the lidar ratio L_{aer}, the Rayleigh backscatter coefficient $\beta_{aer}(r)$, and the backscatter signal P(r) itself contribute to the total error and result in:

$$(\Delta\beta_{aer}(r))^2 = \int_{r_{ref}}^{r} \left(\frac{\partial\beta_{aer}(r)}{\partial P(\tilde{r})}\Delta P(\tilde{r})\right)^2 \mathrm{d}\tilde{r} + \int_{r_{ref}}^{r} \left(\frac{\partial\beta_{aer}(r)}{\partial\beta_{ray}(\tilde{r})})\Delta\beta_{ray}(\tilde{r})\right)^2 \mathrm{d}\tilde{r} + \left(\frac{\partial\beta_{aer}(r)}{\partial L_{aer}}\Delta L_{aer}\right)^2. \tag{4.13}$$

The explicit representations of the difference quotients in Equation 4.13 are shown in the Appendix A.2. The partial errors of the signal and the Rayleigh backscatter coefficient has to be integrated from the reference height r_{ref} to the current analyzed range r. This means, larger distances from reference height imply larger uncertainties in the resulting backscatter coefficient. Thus, it is important to select the reference height as near as possible at the interesting height range. The relative uncertainty of the signal P(r) is estimated by the standard deviation and the mean value of one cloud free profile. The partial error of the backscattered signal does not exceed 3 % below a range of 15 km. The partial error in the Rayleigh backscatter coefficient is estimated in Section 4.4.1 and remains below 2 %. The partial error of the lidar ratio represent the largest uncertainty in the determination of particle backscatter coefficient. It is minimized by accurate investigations of each cirrus cloud profile by forward and backward integration. Nevertheless, the lidar ratio uncertainties can be conservatively estimated to be around 20 %. Especially, for thin cirrus clouds this high uncertainty is justified, because the Klett inversion is not sensitive to the lidar ratio of optical thin cirrus clouds. In this case, all assumed lidar ratios produces almost the same profile of backscatter coefficient. Seifert et al. (2007) reports a similar relative uncertainty of the estimated lidar ratio below 25 % for optical thin cirrus clouds.

Figure 4.4 displays the impact of each error on the total uncertainty of the backscatter coefficient profile and the extinction profile for a typical cirrus cloud observation. Panel a) displays the same backscatter coefficient profile obtained from backward integration as shown in Figure 4.3. The single partial errors are illustrated in panel b). The smallest error is caused by the uncertainties in the backscatter signal, while the largest error outside the cirrus is caused by the uncertainties in the Rayleigh backscatter coefficient and inside the cirrus through the uncertainties in the lidar ratio. All three errors give the total error of the particle backscatter coefficient (dotted line) with a maximum in the cirrus cloud.

The uncertainty in the estimation of the lidar ratio affects the accuracy of the extinction coefficient linearly. While the impact of the lidar ratio uncertainty on the backscatter coefficient

has only a moderate proportion (∼4 % in cirrus range), the effect on uncertainties in the extinction coefficient profile are obvious larger (∼21 % in cirrus range, panel c). This increased uncertainty has to be taken into account for the determination of cirrus properties.

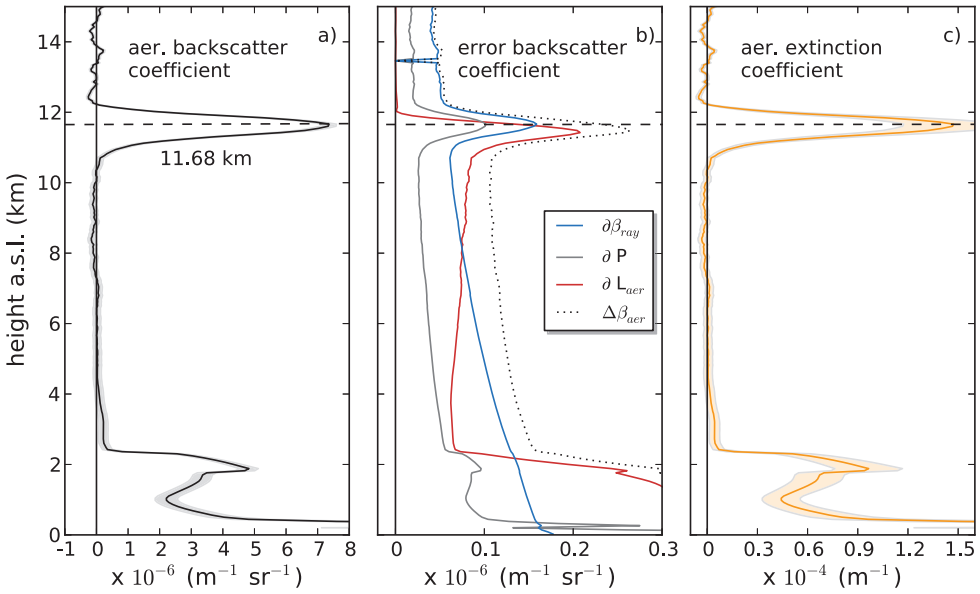

Figure 4.4: Profiles of backscatter and extinction coefficients with associated errors of an observed cirrus cloud on 10.08.2011 from 07:00 to 08:30 UTC at 11.68 km height. a) gray shaded area: Backscatter coefficient with a lidar ratio of 20 sr and resulting error. b) Contribution of single errors of Rayleigh backscatter coefficient ($\partial\beta_{\mathrm{ray}}$), signal ($\partial$P), and lidar ratio ($\partial$L$_{\mathrm{aer}}$) to the total error of backscatter coefficient (dotted line). c) Extinction profile with errors (orange shaded area).

4.3.4 Depolarization

The state of polarized light can change by scattering on molecules and particles. This modification is called depolarization. Microphysical properties of aerosol, clouds, and precipitation can be derived from the depolarization signal. The magnitude of depolarization is representative for the asphericity of the scattering particles. While ice particles or other aspherical particles mostly create a large signal in the depolarization, because of their non spherical shape, spherical particles create a depolarization close to zero. The depolarization of atmospheric gas molecules is not zero caused by their anisotropy of charge carriers (see Appendix A.1.1). The molecular depolarization δ_{ray} is rather small with a value of around 0.00395 considering only the Cabannes line (see Section 4.2). However, the molecular depolarization dominates the volume depolarization signal even in the presence of particles with low concentrations.

The depolarization can be measured by the use of a linear polarized laser and two detectors measure the parallel and the perpendicularly polarized backscattered light related to the emitted laser polarization. The depolarization is described after Schotland et al. (1971) by:

$$\delta^{vol}(r) = \frac{P^{\perp}_{Tel}(r)}{P^{\parallel}_{Tel}(r)} = \frac{\beta^{\perp}(r)}{\beta^{\parallel}(r)} exp\left(\tau^{\parallel} - \tau^{\perp}\right), \tag{4.14}$$

where $\mathrm{P}^{\perp}_{\mathrm{Tel}}$ and $\mathrm{P}^{\parallel}_{\mathrm{Tel}}$ are the backscatter intensities of each polarization state directly arrived at the telescope of the lidar system. The quantities $\beta^{\perp}$ and $\beta^{\parallel}$ are the total backscatter coefficients of the respective polarization states in range r. The optical depths $\tau^{\parallel}$ and $\tau^{\perp}$ are assumed to be equal so that the transmission term in Equation 4.14 can be set to one (Sassen, 2005). The depolarization with total backscatter coefficients ($\beta = \beta_{\mathrm{ray}} + \beta_{\mathrm{aer}}$) is referred to as linear volume depolarization δ^{vol}, due to the backscattered light receiving from all molecules and particles in the measurement volume. While the volume depolarization can be directly derived from the backscatter signals, the determination of particle depolarization ratio requires the knowledge of the particle backscatter coefficient from the Klett inversion. In clouds and particle layers where $\beta_{\mathrm{ray}} \ll \beta_{\mathrm{aer}}$ the volume depolarization corresponds nearly to the particle depolarization. In general, the particle depolarization can be determined with the Rayleigh depolarization δ^{ray} (see Appendix A.1.1) and the volume depolarization δ^{vol} (Cairo et al., 1999):

$$\delta^{aer}(r) = \frac{\beta^{\perp}_{aer}(r)}{\beta^{\parallel}_{aer}(r)} = (\delta^{vol}(r) + 1)\left(\frac{\beta_{ray}(r)(\delta_{ray} - \delta^{vol}(r))}{\beta_{aer}(1 + \delta_{ray})} + 1\right)^{-1} - 1. \tag{4.15}$$

Due to different efficiencies in both detection channels (parallel and perpendicular), it is not possible to detect $\mathrm{P}^{\parallel}_{\mathrm{Tel}}$ and $\mathrm{P}^{\perp}_{\mathrm{Tel}}$ directly. In addition, each detector measures a combination of both polarization states due to instrumental and optical effects within the detection unit. The measured backscatter signal of detector i is composed of a parallel and a perpendicular backscatter component ($\mathrm{P}^{\parallel}$ and $\mathrm{P}^{\perp}$) and can be described with different transmission efficiencies $\eta^{\perp}_{\mathrm{i}}$ and $\eta^{\parallel}_{\mathrm{i}}$ of the signal directly received at the telescope by

$$P_i(r) = P^{\parallel}_i(r) + P^{\perp}_i(r) = \eta^{\parallel}_i \; P^{\parallel}_{Tel}(r) + \eta^{\perp}_i \; P^{\perp}_{Tel}(r). \tag{4.16}$$

The calculation of the volume depolarization can be done either in an idealized or non-idealized way. If the depolarization properties of the system and especially the detectors is known, the exact way is the non-idealized calculation of the depolarization. Both techniques are used in the further data analysis and are described in the next subsection.

Idealized Systems

In case of an idealized detection system, it is assumed that the parallel detector, denoted as $\mathrm{P_h}$, measures only the parallel light ($\mathrm{P_h^{\perp}} \ll \mathrm{P_h^{\parallel}}$ and $\eta_{\mathrm{h}}^{\perp} \ll \eta_{\mathrm{h}}^{\parallel}$). Moreover, the perpendicular detector, denoted as $\mathrm{P_v}$, measures only the perpendicular light ($\mathrm{P_v^{\parallel}} \ll \mathrm{P_v^{\perp}}$ and $\eta_{\mathrm{v}}^{\parallel} \ll \eta_{\mathrm{v}}^{\perp}$). The quantities $\mathrm{P_h(r)}$ and $\mathrm{P_v(r)}$ represent the actual measured signals in range r from the parallel and perpendicular detector, respectively. By inserting Equation 4.16 with the assumptions above in Equation 4.14 the depolarization ratio results in:

$$\delta_{ideal}^{vol}(r) = \frac{\eta_{\mathrm{h}}^{\parallel} P_{\mathrm{v}}(r)}{\eta_{\mathrm{v}}^{\perp} P_{\mathrm{h}}(r)} = C_{ideal} \frac{P_{\mathrm{v}}(r)}{P_{\mathrm{h}}(r)}. \tag{4.17}$$

According to this equation the calculation of the volume depolarization is done by devision of the perpendicular and parallel measured signal normalized by the constant $\mathrm{C_{ideal}}$ (Schotland et al., 1971). The constant $\mathrm{C_{ideal}}$ includes the detection efficiencies of parallel and perpendicularly polarized light of the detectors. In general, the efficiency parameters $\eta_{\mathrm{h}}^{\parallel}$ and $\eta_{\mathrm{v}}^{\perp}$ are not directly available and are unknown. The constant $\mathrm{C_{ideal}}$ can be determined by normalizing the volume depolarization to an area in the atmosphere where virtually no particle scattering but only the known molecular depolarization δ_{ray} (see Appendix A.1.1) occurs. This calibration constant is calculated by:

$$C_{ideal} = \delta_{ray} \frac{P_{\mathrm{h}}(r)}{P_{\mathrm{v}}(r)}. \tag{4.18}$$

The free troposphere above 3 km with negligible particle concentrations is therefore a good choice for this calibration. Additionally, the particle free region can be estimated more precisely from the minimum in backscatter coefficient profile determined by the Klett method.

As mentioned in Section 4.3.1 the total backscatter signal ($\mathrm{P_h(r) + P_v(r)}$) is used in the Klett method. The total signal can also be derived by the use of the ideal calibration constant C_{ideal} to account for different detector efficiencies and Equation 4.16, yielding

$$P(r) = \frac{P_h(r)}{C_{ideal}} + P_v(r). \tag{4.19}$$

The ideal calibration constant is determined every day to avoid a shift in the depolarization measurements. The mean constant from all depolarization calibrations measured with this lidar system is 0.007. This means, that the contribution of the detected perpendicular polarized light to the total signal is only around 0.7 % in particle free regions, where the contribution of the parallel polarized light is around 99.3 %. The effect of perpendicular detected light on the total signal is therefore rather small and plays only a role in strong depolarizing particle layers

(e.g. cirrus clouds) where the perpendicular signal increases significantly in comparison to the parallel signal.

Non-idealized Systems

Usually, every detection system is not ideal and the suppression of the unwanted polarization component in each detector is limited. Therefore, the parallel detector $\mathrm{P_h}$ measures also a small amount of perpendicular polarized light and the other detector vice versa. This process is called cross-talk and leads to an underestimation of the volume depolarization, if an idealized system is assumed. It is crucial to take this effect into account for an accurate measurement of volume as well as particle depolarization ratio. By inserting Eq. 4.16 into Eq. 4.14 the real measured total signal of detector i with i = {h,v} results in (Mattis et al., 2009):

$$P_i(r) = \eta_i^{\parallel}\ P_{Tel}(r) \left(\frac{1 + D_i\ \delta^{vol}(r)}{1 + \delta^{vol}(r)} \right), \tag{4.20}$$

with

$$D_i = \frac{\eta_i^{\perp}}{\eta_i^{\parallel}}. \tag{4.21}$$

$\mathrm{D_i}$ represents the transmission ratio of all optical elements on the light path between telescope and detector i. It describes the ratio of the transmission efficiencies $\eta_\mathrm{i}^\mathrm{p}$ of each polarization component introduced in the lidar equation (Eq. 4.1). If the transmission ratio is not equal one ($\mathrm{D_i} \neq 1$), the detected signal depends on the volume depolarization. The ratio of the two detection channels $\mathrm{P_h(r)}$ and $\mathrm{P_v(r)}$ in respective versions of Eq. 4.20 and different transmission ratios $\mathrm{D_h}$ and $\mathrm{D_v}$ yielding the depolarization in range r by(Mattis et al., 2009):

$$\delta_{h,v}^{vol}(r) = \frac{C_{h,v} - v_{h,v}(r)}{D_h\ v_{h,v}(r) - D_v\ C_{h,v}}, \tag{4.22}$$

where the signal ratio is defined as $\mathrm{v_{h,v} = P_v(r)/P_h(r)}$ and the calibration constant represented by $\mathrm{C_{h,v}}$. The determination of calibration constant follows from Eq. 4.22:

$$C_{h,v} = \frac{v_{h,v}(r)\,[D_h\ \delta_{ray} + 1]}{D_v\ \delta_{ray} + 1} \qquad \text{and} \qquad v_{h,v} = \frac{P_v(r)}{P_h(r)}. \tag{4.23}$$

The explicit determination is done with same procedure as described in the ideal case (Section 4.3.4). By assuming an ideal detection system with $\eta_\mathrm{h}^{\perp} \to 0$ and $\eta_\mathrm{v}^{\parallel} \to 0$ this equation can be transformed back into Equation 4.18. Practically, the only unknown quantities are the

transmission ratios (D_h and D_v), which have to be determined experimentally as described in the Appendix A.3.

4.4 Cirrus detection with Leo-Lidar

This section describes the determination of optical, macrophysical, and microphysical properties of cirrus clouds. The optical properties i.e. depolarization, backscatter and extinction coefficients, as well as the macrophysical properties i.e. cloud base height, cloud top height, and cloud thickness can be estimated with the Leo-Lidar. However, several aspects and influences concerning cirrus cloud detection with a lidar system has to be taken into account. In the first subsection the best sources for the required meteorological parameters (i.e. temperature and pressure) are discussed. Furthermore, two effects, the specular reflection and the multiple scattering, interfere the determination of optical properties of cirrus clouds. In Section 4.4.2, specular reflection in cirrus clouds and the way to prevent this effect on lidar determined quantities is described. Section 4.4.3 introduces multiple scattering of laser light in clouds and a scheme to correct the derived particle extinction and backscatter coefficient for this effect. Subsequently, the determination of cirrus cloud ice water content is explained in Section 4.4.4. Finally, the whole cirrus detection and analysis scheme is described in Section 4.4.5.

4.4.1 Meteorological data

The determination of backscatter and extinction profiles requires input of temperature and pressure profiles. In addition, microphysical properties of cirrus clouds as well as the relative humidity also depends on these parameters. Therefore, it is essential to have this information as accurate as possible. Several sources can be used to get adequate meteorological data.

We use global meteorological data provided by the ECMWF (European Centre for Medium-Range Weather Forecasts). This data are available every 6 hours (00, 06, 12, 18 UTC) in a high horizontal resolution of 0.1 x 0.1 degree and a vertical resolution of 100 m, providing temperature, pressure, specific humidity and a modeled cloud ice water content. Interpolation of the data to the location and time where the lidar observation are performed, provides the most appropriate profiles. Certainly, ECMWF data often show a dry bias of H_2O in the upper troposphere (Luo et al., 2008) and mesoscale temperature fluctuations are not well represented (see Section 3.2). Therefore, small discrepancies between ECMWF and radiosonde data can be found despite assimilation of satellite and radiosondes data. Nevertheless, the best choice for temperature, pressure, and humidity data are the ECMWF data due their good coverage and frequency of availability. But it is advisable to use radiosonde measurements to evaluate the ECMWF data at the time of observation.

Radiosonde soundings from the nearest station of the DWD (German Meteorological Service) located in Essen, 70 km north west of Jülich (station code 10410) are used. These soundings

are provided every 12 hours (00 UTC and 12 UTC) and include measurements of temperature, pressure, and relative humidity in each hight level. The DWD normally uses Vaisala RS92 radiosondes that directly measures relative humidity. Vömel et al. (2007) identified a dry bias in these radiosondes in comparison to the CFH (Cryogenic Frostpoint Hygrometer), especially in daytime measurements. Therefore, a correction scheme is suggested in Vömel et al. (2007), which is also applied to the radiosonde data used in this study. The temperature, pressure, and relative humidity data are in situ measurements and should provide the best agreement to real values in the atmosphere. However, the radiosonde data are unsuitable for lidar data analysis because the location of the profiles does not exactly coincide with the lidar in Jülich. But it is appropriate to use the radiosonde data for evaluation of the ECMWF data. If the radiosonde profile is comparable to the interpolated ECMWF profile over Essen, the ECMWF data can also most likely be used for lidar data analysis at Jülich. If there are larger discrepancies especially in temperature and pressure, the ECMWF data have to be used with caution and the effect on resulting lidar data (i.e. backscatter / extinction coefficient) has to be considered.

For a quick analysis of the lidar data the U.S. standard atmosphere from 1976 (NOAA et al., 1976) is used. This idealized atmosphere represents the mean values of temperature and pressure at mid-latitudes (around 40°) with a ground temperature of 15°C and a ground pressure of 1013.25 hPa. The relative differences to the true annual mean values are comparatively small and in the range of few percent. However, these profiles are not sufficient describing local weather variations or other dynamic effects and are not used for cirrus cloud investigations.

For a general point of view, the radiosonde and ECMWF data for Essen are compared to show how large the actual discrepancies are. Here, all available radiosonde soundings within one year (from April 2011 to April 2012, in total 725) are used and directly compared with the corresponding ECMWF data. The annual mean of temperature and pressure with the corresponding standard deviation at each height level is shown in the upper panels of Figure 4.5 for radiosonde (left) and ECMWF data (right). In addition, the U.S. standard atmosphere from 1976 is plotted with black dots and shows a rather good agreement with the mean profiles of both data sets. Between 4 and 6 km the mean temperature profiles are slightly (1 - 2 K) above and in the planetary boundary layer (0 to 2 km) slightly below (3 - 4 K) the standard atmosphere. The mean pressure fits well to the standard atmospheric pressure curve. In general, both datasets have a very similar appearance even with regard to the standard deviation in temperature. The absolute deviations of each parameter (i.e. temperature, pressure and relative humidity with respect to water) are shown in the middle panels of Figure 4.5 to illustrate the discrepancies. The annual mean deviation is represented by solid lines and the standard deviation by light shaded areas.

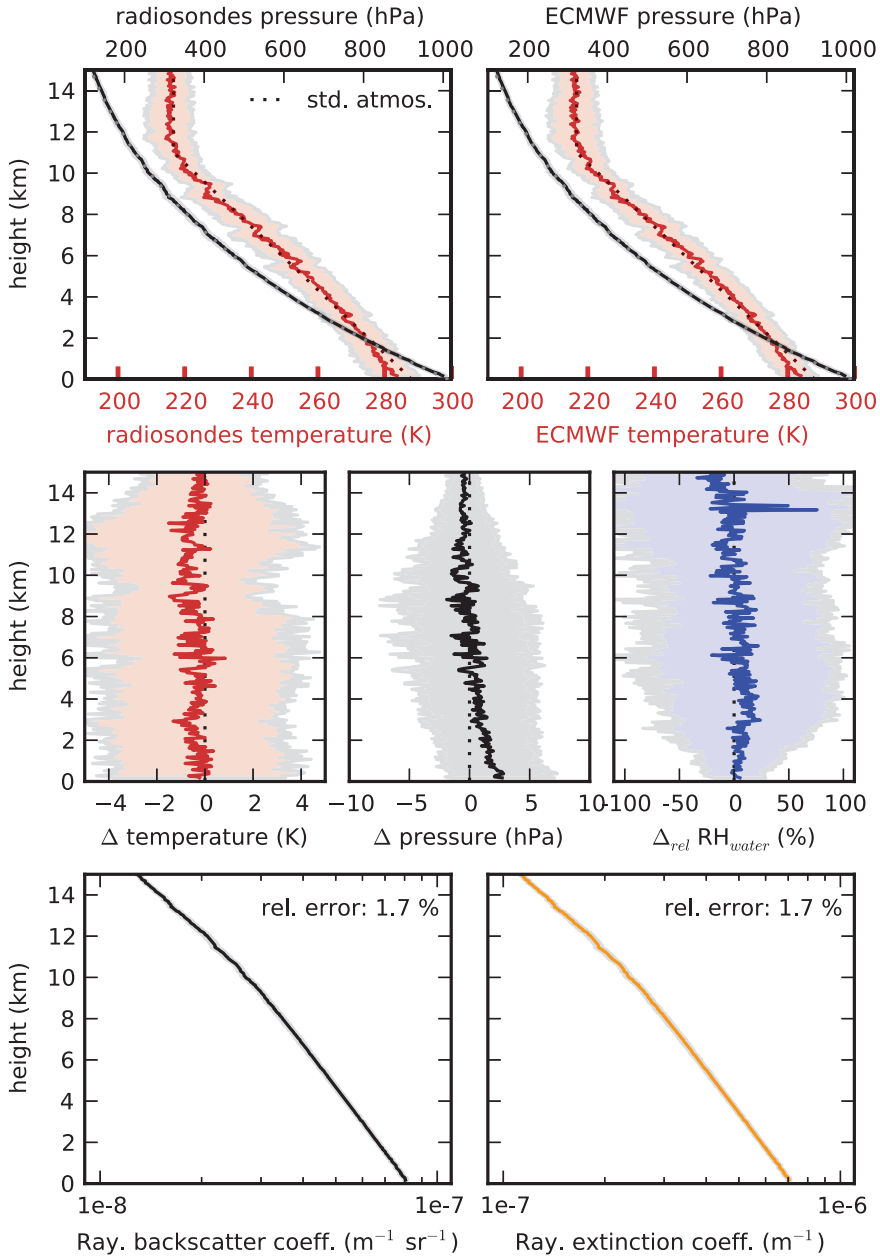

Figure 4.5: Upper panels: one year mean and standard deviation of radiosondes (left) and ECMWF (right) high resolution temperature and pressure data. Middle panels: difference of temperature (left), pressure (middle), and relative humidity (right) between radiosonde and ECMWF data. Lower panels: Rayleigh backscatter and extinction coefficients derived from radiosondes mean temperature and pressure profile with calculated error.

The mean differences Δ for one parameter χ are calculated with:

$$\Delta\chi(r) = \overline{Radiosonde_{\chi}(r) - ECMWF_{\chi}}, \tag{4.24}$$

where a negative deviation means the ECMWF data are larger than the measured radiosonde data. The differences in temperature are rather small and ECMWF data are generally in accordance to the radiosonde profiles. Only between 8 and 12 km the radiosonde measures $\sim$0.6 K colder temperatures in the annual mean. The standard deviation stays almost constant around 3 to 4 K in all height levels. This shows, that in individual profiles larger discrepancies between ECMWF and radiosonde data exist. These discrepancies are most likely related to missing small scale temperature fluctuations.

The relative pressure differences are somewhat smaller, but show a shift from lower ECMWF pressure (2.5 hPa) in comparison to radiosonde data in the boundary layer region to slightly higher values (1 hPa) above 10 km. The best agreement of both mean profiles is between 5 and 10 km but with the largest standard deviation of up to 5 hPa.

In contrast to temperature and pressure data the relative humidity differences are generally much larger. Due to the large range of possible relative humidity values existing in the atmosphere, the relative differences between radiosonde and ECMWF data are shown in this case. The standard deviation is around 70 % between 2 and 10 km and show a slight increase from 10 to 15 km in the tropopause region. The mean profile shows a good agreement between both datasets in general (deviations close to zero). Only between 3 and 5 km the ECMWF data are dryer than the radiosonde data and above 13 km the radiosondes show a dry bias. However, at these altitudes the relative humidity is quite low and precise measurements can only be done by more sophisticated instruments.

The resulting Rayleigh backscatter and extinction coefficient are shown in both lower panels of Figure 4.5, calculated from the annual mean ECMWF temperature and pressure profile with Equation A.13. The uncertainties in both coefficients can be estimated with the comparison between radiosonde and ECMWF data by using the standard deviation as error for temperature and pressure. The error in both coefficients can be calculated with normal Gaussian error propagation and is plotted as gray shaded area around the solid lines. The relative error is estimated to be around 1.7 %. Therefore, an uncertainty in Rayleigh backscatter and extinction coefficient of at most 2 % is used for error estimation of particle backscatter coefficient described in Section 4.3.3.

In conclusion, the ECMWF data are overall sufficient for estimation of Rayleigh backscatter and extinction coefficient and are also used for further cirrus cloud analysis at the site of observation (Jülich). Temperature and pressure are good represented with only small discrepancies in comparison to the radiosonde data. The humidity data should be handled with care due to frequently appearance of large differences and a direct comparison between

radiosonde and ECMWF data is advisable before an use of ECMWF humidity data.

4.4.2 Specular reflection

Specular reflections can distort the lidar measurements when observing mixed-phase or cirrus clouds. This 'mirror-like' reflections are observed as the laser beam is directly reflected to the receiver, without performing a real scattering process and occur if large ice crystals align horizontally (Platt et al., 1978; Westbrook et al., 2010). Lidar observation of this horizontally aligned ice crystals are distinguished by a low depolarization signal and a high backscatter coefficient, as shown in Figure 4.6. The depolarization is similarly low as for spherical particles or water droplets. The unambiguous identification of ice clouds, as introduced in Section 4.3.4, is not possible anymore.

The formation of layers with horizontally aligned ice particles depends mostly on temperature, supersaturation, and the location within the cloud. The crucial microphysical properties are shape and size of ice particles. If ice particles are small with a diameter of about few µm, they are mostly randomly oriented due to Brownian turbulent motion of the air (Hallett et al., 2002). If ice crystals are larger, sedimentation occurs. Particles can align horizontally during falling, if they have a plate like shape. Platt et al. (1978) presented the first study of specular reflection during observations with a scanning lidar system and showed the existence of rather large ice particles with diameter of 74 µm, at warm temperatures of −9°C to −13°C, and a maximum departure of the ice particle axis from the horizontal of 0.5°. In agreement to other studies, Thomas et al. (1990) found in a three year record of lidar data that 50 % of ice clouds observation were affected by specular reflection, mostly at 9 km altitude in a similar

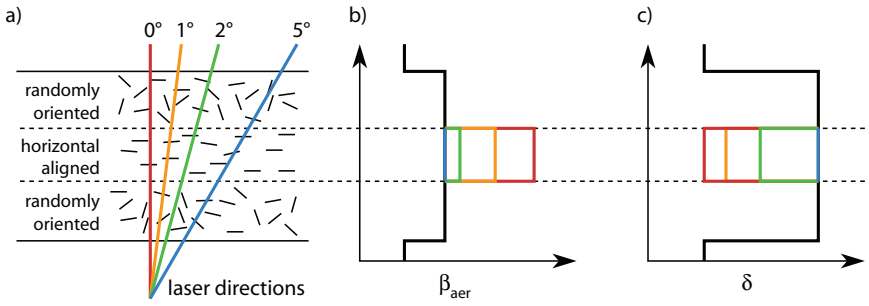

Figure 4.6: Schematic diagram of specular reflection caused by a three layered cirrus cloud with randomly oriented ice crystals and horizontal aligned planar ice crystals depending on lidar zenith angle. Panel b): backscatter coefficient β_{aer}; Panel c): depolarization δ. Adapted from Seifert (2010).

temperature range (−8°C to −25°C). In this range the most appearing ice particle shape is plate-like (Bailey and Hallett, 2002), which provide the best conditions for the appearance of specular reflection. The effect of specular reflection mostly vanishes at the cloud base as reported in Westbrook et al. (2010). Normally, the temperatures at the cloud base are the warmest within a cloud layer. If large ice plates sediment into this inceptive sub-saturated environment, they begin to melt and lose there plate-like shape, which is necessary for specular reflection.

The strength of the specular reflection effect depends on the zenith angle of the lidar beam. Figure 4.6 illustrates the effect of specular reflection for a three layered cirrus cloud with randomly oriented ice particles above and below a layer containing oriented ice particles. In panel b) and c) of Figure 4.6 the corresponding backscatter coefficient and depolarization signal is shown exemplarily, where the black and blue colored lines represent the unaffected measured signals for a complete equally distributed cirrus cloud with randomly oriented ice particles. While a zenith angle of 0° (Figure 4.6, red colored) creates the largest effect in the obtained measurement quantities, the effect vanishes completely for zenith angles above 3° (Figure 4.6, blue colored) and depolarization as well as backscatter coefficient approach a value not influenced by this effect as shown in Seifert (2010).

The zenith angle can practically be adjusted by titling the whole lidar head including the laser and detector unit of the Leo-Lidar. A zenith angle of about 5° is used to avoid a distortion of cirrus depolarization and backscatter coefficient measurements due to specular reflections. For that reason the measured range of the backscattered light does not correspond to the altitude of the scattering volume and has to be corrected for the titled angle.

4.4.3 Multiple scattering

The lidar equation 4.1 describes only single scattering processes in the atmosphere. Thus, it is assumed that the detector receives solely photons that were scattered only one time by a single particle which either leads to extinction or backscattering of the photon. This assumption is valid for all optical thin particle layers with small effective particle radii. But, with increasing optical depth and increasing size of particles the probability of multiple scattering events raises. Due to the strong forward scattering of large particles, single photons remain in the field of view of the detector and increase the residence time in the particle layer (Bissonnette, 1996; Wandinger, 1998; Bissonnette et al., 2005). Figure 4.7 demonstrates the possible pathways of photons within a cloud layer. Beside single scattering (red line) on cloud particles with direct backscattering in an angle near 180°, multiple scattering (black lines) occurs. If a photon is scattered forward, which is equivalent to an extinction event, the photon remains in the particle layer and is available for an additional backscatter process. Even at the borders of the FOV the photon could leave and reenter it again due to multiple scatter processes. Thus the backscatter coefficient is overestimated with increasing multiple scattering. Rather more

photons reach the detector from a specific altitude range than in single scattering appearance. The extinction as well as the optical depth is therefore underestimated. The extinction coefficient is underestimated by up to 50 % at the cloud base (Wandinger, 1998).

The main parameters contributing to the strength of multiple scattering are on one hand the geometry of the detection system and on the other hand the optical properties of the scattering medium itself (Wandinger, 1998; Bissonnette et al., 2005). The divergence of the detector or FOV is crucial for the multiple scattering effect resulting from the geometry of the detection system. The effect is not negligible for a FOV larger than 1 mrad and increase strongly with rising divergence or increasing distance to the detector. This is obvious, because the scattering volume and the amount of scattering particles increases for a larger FOV or increasing distance. Further, the optical depth and effective particle radius influence the multiple scattering. More photons are scattered into the forward direction with increasing particles size in comparison to the laser wavelength (see panel b) of Figure A.1). This effect increases the residence time in the FOV and increases the probability of a multiple scattering process.

The multiple scattering effect leads to an underestimation of extinction values up to 50 % and optical depth of about 20 to 30 %. The strength of correction of the measured extinction profile increases with the particle effective radius and the divergence of the FOV (see Appendix A.6). The multiple scatter effect has to be corrected even in the case of the used Leo-Lidar with a relative large FOV of 1.5 mrad. We use a fast lidar and radar multiple-scattering model described in Hogan (2008) for the correction of the particle extinction profiles. This model is explicitly developed for cirrus cloud observation with ground-based and space-borne lidars. Input parameters are the observed cloud heights, particle extinction coefficients with the connected lidar ratio, effective particle radius, and the optical geometry of the lidar e.g.

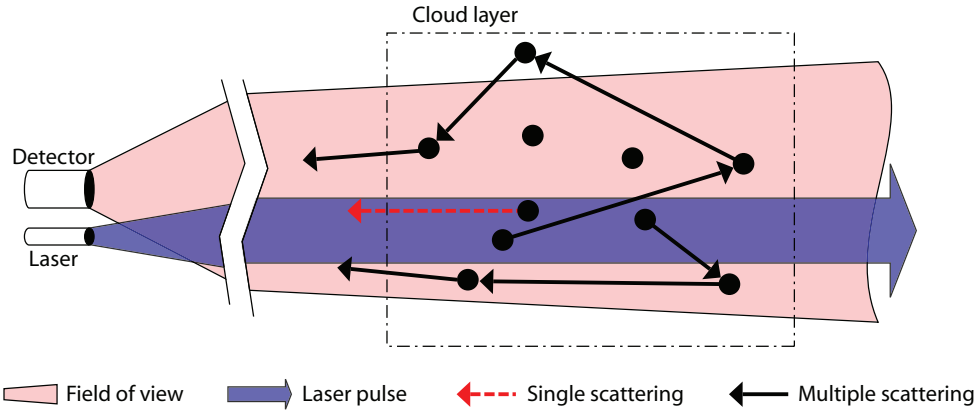

Figure 4.7: Scattering pathways of single photons within a cloud layer. Single and multiple scattering occurs (black and red lines) on cloud particles (black dots) from the laser pulse (blue shaded area) and stay in the FOV (red shaded area). Adapted from Bissonnette et al. (2005).

FOV divergence. The particle size is relevant considering the effect of multiple scattering as explained. However, this quantity is not directly available from the lidar measurements itself and a parametrization from Boudala et al. (2002) derived from in situ ice microphysics aircraft measurements is therefore used to get the mean effective radius of ice particles. This parametrization depends only on temperature and can easily be used for calculation of a vertical ice particle radius profile with the help of ECMWF temperature profiles at the lidar location. The multiple-scattering model is a forward model, this means that the model calculates from an unaffected extinction profile a profile of backscatter coefficients (single scattering) affected by multiple scattering. The model is inverted with an iterative method described in Wandinger (1998) for the correction of an extinction profile affected by multiple-scattering. This is done exemplary in Appendix A.6 for different particle sizes and cloud optical thicknesses.

Beside the influence on the backscatter and on the extinction coefficient, multiple scattering influences also the depolarization of water clouds. The linear depolarization of spherical particles is very close to zero, but this is only true for a scatter angle of exactly $\theta = 180°$. In case of multiple scattering, photons are scattered in forward direction and scattered back to the detector with different angles in a range from around 177 to 180°. This deviation of only few degree from the exact backscatter angle results in a linear depolarization of spherical particles i.e. water droplets of up to 60 % (Sassen and Zhao, 1995). With increasing penetration depth of the laser beam into the cloud, the amount of forward scattering events raises and thus the number of backscattered photons different from a backscatter angle of 180° increases. The depolarization increases therefore from cloud base towards cloud top.

For this study the depolarization is used to discriminate between aspherical particles especially ice clouds and liquid water clouds (spherical particles). If a water cloud produces a high depolarization, it can be incorrectly considered as cirrus cloud. However, a wrong classification can be avoided by neglecting all clouds with increasing linear depolarization within the cloud. In Figure 4.8 two boundary layer water clouds visible in the time period from 18 to 18:20 UTC and 20 to 21 UTC in the range corrected signal (top panel) at a temperature around 5 °C. The second cloud attenuate the backscatter signal stronger than the first cloud. This is clearly visible due to low backscatter values above 2.3 km. Thus the second cloud is obvious optical thicker than the first cloud and produces an overestimation of the depolarization (bottom panel) up to 1.5 % due to multiple scattering. The effect of increasing depolarization signal towards cloud top is clearly visible in the mean depolarization profile on the left side. This effect allows to exclude all cloud observations from further investigations with this obvious appearance in the depolarization profile. The multiple scattering doesn't affect the depolarization of a cirrus cloud because all ice particles are normally randomly oriented, except for the case of specular reflection explained in Section 4.4.2. This means the backscatter angle doesn't play a large role and the depolarization occurs independently of strong forward scattering.

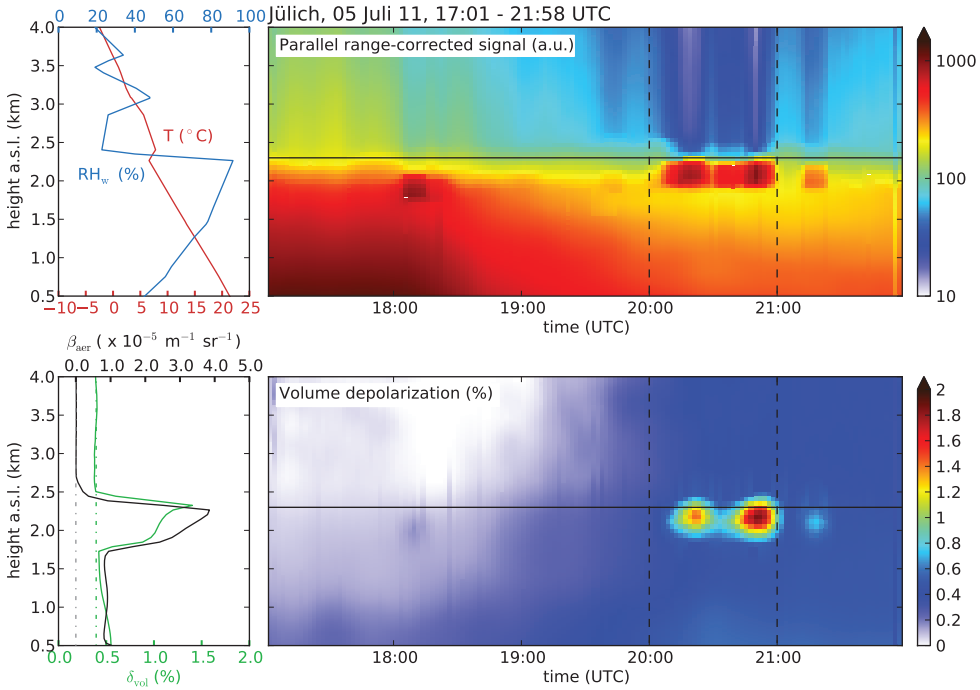

Figure 4.8: Lidar observations of two liquid water clouds between 1.7 and 2.3 km altitude on 05 July 2011 are displayed. Top panel: parallel range corrected signal with profiles of temperature and relative humidity with respect to water from radiosonde data (00 UTC) located at Essen. Bottom panel: volume depolarization in percent with mean backscatter coefficient profile and mean depolarization profile between 20 and 21 UTC (marked with dashed black lines).

4.4.4 Determination of cirrus ice water content

The ice water content (IWC) is a crucial quantity to describe a cirrus cloud and represents the amount of frozen water. It can be directly measured by aircraft in situ instruments (Schiller et al., 2008; Krämer et al., 2009) and is proportional to optical properties like effective radius and extinction coefficient or optical depth. Measurements of IWC with different techniques can easily compared with simulation results of ice formation models using respective IWC values. Due to the proportionality to optical quantities, it is possible to determine the IWC from the particle extinction coefficient measured with a lidar. The extinction is converted into IWC using a parametrization provided by Heymsfield et al. (2005), which is derived from extinction and IWC aircraft in situ measurements for determining IWC from CloudSat radar and Calipso lidar data:

$$IWC = a \cdot \sigma^b, \tag{4.25}$$

with IWC in g/m^3, extinction σ in m^{-1}, and the constants a = 89. + 0.6204 · T(°C) g/m^2 and b = 1.02 − 0.00281 · T(°C)). Using this parametrization, IWC from ice model simulations with MAID as well as in situ IWC measurements can be compared to extinction observations with the Leo-Lidar. The IWC error is given by the uncertainties of the extinction profile and is calculated by Gaussian error propagation. The detection limits of cirrus IWC are discussed in Section 5.3.3 by using climatological lidar cirrus measurements.

4.4.5 Analysis scheme

In this section, the analysis scheme to derive the particle extinction as well as IWC profiles from the cirrus cloud observations is described as developed in this thesis. Figure 4.9 illustrates the analysis scheme for a single cirrus cloud. **Step 1** is the signal processing with data averaging and smoothing of both detection channels to a resolution of 1 min in time (i.e. 1200 single laser shots) and 30 m in altitude. After this, the volume depolarization is calculated from the two channels by normalizing the signal ratio of an aerosol free region as described in Section 4.3.4 (**step 2**). If an enhanced depolarization signal and range corrected backscatter signal is found, the area is marked as potential cirrus cloud (step 3). Multiple scattering in water clouds and specular reflection are taken into account (see Sections 4.4.2 and 4.4.3). In **step 3**, the temporal extent of the cirrus cloud is determined from the first to the last lidar profile with high depolarization and backscatter signal in the selected area. By determination of extinction values out of a noisy backscatter signal the Klett method can get instable and can overestimate backscatter and extinction values. Therefore, all lidar profiles within this evaluated time range are averaged over time to get one representative and low noise mean lidar profile, which is used for further analysis. The cirrus base and top heights are estimated with this mean lidar profile by taking the heights where the signal starts to increase or finished decreasing to the background value, respectively. The cloud thickness can be easily derived from the base and top heights. This selection process is shown in Figure 4.10, where the analysis of one cirrus cloud is shown exemplarily. In case of several cirrus clouds occurring during one time period, each cloud is analyzed separately. Two clouds with a temporal distance of 10 min or height distance of 300 m are considered to be different. Furthermore, a cloud is only considered if the cloud top is clearly identified. If a cloud is optically thick, so that no signal from above the cloud reached the detector, the cloud is not further considered. This effect is also associated with a low signal to noise ratio (SNR) above the cloud.

After determination of the macrophysical cirrus cloud properties the optical properties can be obtained from the lidar signals. **Step 4** in the analysis scheme (see Figure 4.9) is the calculation of the total signal as described in Section 4.3.4. **Step 5** depicts the calculation of Rayleigh backscatter coefficient profile from the high resolution ECMWF data. The reference height directly below and above the investigated cirrus cloud is chosen in **step 6** by assuming particle free conditions. In the vicinity of clouds this assumption is valid for wavelengths

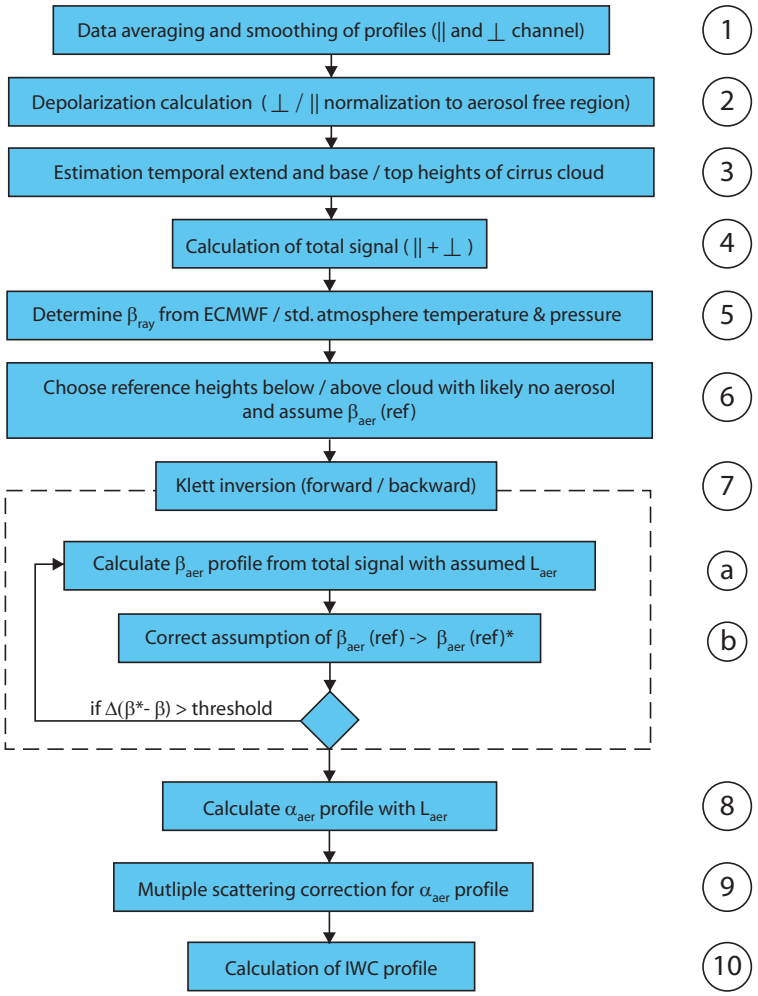

Figure 4.9: Schematic overview of the data analysis process of a single cirrus cloud.

$\lambda \leq 532$ nm as reported in Lynch et al. (2002). **Step 7** constitute the Klett inversion with forward and backward integration for an optimal estimation of the lidar ratio L_{aer} and profile of backscatter coefficients (see Section 4.3.1 and 4.3.3). This estimated lidar ratio is usually constant for a uniform ice particle composition, shape and particle size distribution within a cirrus layer (Seifert et al., 2007). Cirrus clouds with larger vertical extent could have different microphysical properties of ice particles and lead to increased uncertainties of the lidar ratio and extinction coefficient. In this cases, it is not possible to determine an extinction coefficient profile but rather a mean extinction coefficient within the cirrus cloud can be estimated. The Klett inversion (step 7) provide the profile of backscatter coefficients from which the extinction coefficients are estimated in **step 8** (see Section 4.3.2). **Step 9** depicts the application of the multiple scattering correction (see Section 4.4.3). The last step (**step 10**) is the calculation of the IWC profile of the cirrus cloud using Equation 4.25 (see Section 4.4.4).

Figure 4.10 shows lidar measurements of a cirrus cloud observed on the June 5, 2011 over Jülich. In the top panel the parallel range corrected signal is shown, where the investigated cirrus cloud is marked by a black box according to the requirements mentioned above. In addition, meteorological data i.e. profiles of temperature and relative humidity with respect to ice are shown on the left. Between 8 and 11 km a humidity saturated region with temperatures below $-30°$C is visible.

The volume depolarization is shown in the middle panel. The resolution is reduced to 5 min (i.e. 6000 single laser shots) in time and 100 m in altitude to minimize the appearance of noise, especially in the higher altitudes above 10 km. The averaged low-noise profiles of volume and particle depolarization are shown on the left. The jump in particle depolarization at 8.4 km shows the existence of aspheric ice particles. The particle depolarization stays almost constant with values around 17 % over the whole vertical extent of the cirrus and suggests the presence of similar ice particle shapes. Thus, the assumption of a constant lidar ratio is confirmed. The volume depolarization is somewhat lower at the cloud border, where only few ice particles exist. In this areas the contribution of molecular scattering to the volume depolarization is greater than the particle scattering.

In the bottom panel of Figure 4.10 the particle extinction obtained from 5 min averaged data is plotted. The cirrus extinction is characterized by enhanced values around $1 \cdot 10^{-3}$ m^{-1}. A second cirrus layer directly below the investigated cirrus cloud between 7 and 8 km is also visible. In addition, the planetary boundary layer with high particle concentrations and related high extinction values is noticeable between 0 and 1.5 km. In the left panel, the averaged profiles of extinction as well as IWC profile is displayed. This cirrus show a maximum IWC value of 40 ppmv with a total optical depth of 0.5, which represents a typical mid-latitude cirrus cloud (Sassen and Comstock, 2001).

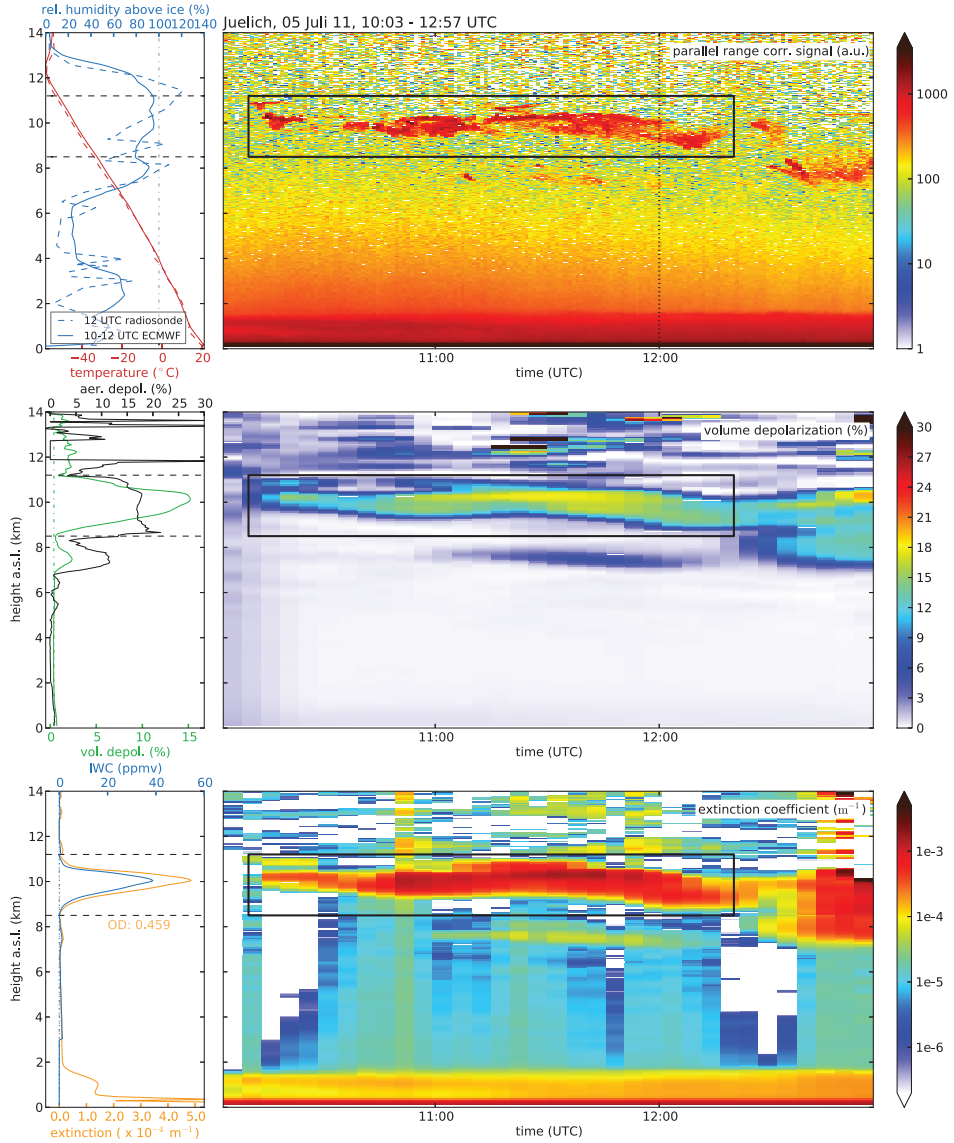

Figure 4.10: Cirrus cloud observation on 5 November 2011 between 10 and 13 UTC. Top panel: range corrected signal of the parallel channel; Left top panel: ECMWF (averaged 10:10 - 12:20 UTC) and radiosonde (12 UTC, station Essen) temperature and relative humidity profiles; Middle panels: volume depolarization (right) and profiles of volume and particle depolarization averaged over cirrus cloud (left); Bottom panels: extinction coefficient (right) and averaged profiles of extinction and IWC (left). The regarded cirrus cloud is marked with a black frame. The obtained cirrus bottom and top heights are displayed as dashed lines in the profile panels.

5 Lidar cirrus climatology

In the period from spring 2011 to spring 2012, 143 cirrus clouds were observed with the ground-based Leo-Lidar over mid-latitude Jülich. The cirrus climatology can be divided into 89 summer observations in the months from May to October 2011 and 54 winter observations in the months from November 2011 to April 2012. All cloud observations were analyzed with the cirrus detection scheme described in Section 4.4.5. In the following sections, the climatological results of this study are shown and compared with earlier lidar and in situ cirrus climatologies, e.g. by Sassen and Campbell (2001) in Salt Lake City, USA (40° 49' North, 111° 49' East), Goldfarb et al. (2001) at the Observatoire Haute Provence, France (43° 54' North, 5° 42' East), Immler and Schrems (2002) in Prestwick, Scotland (55° 31' North, 4° 36' West), and Schiller et al. (2008) as well as Luebke et al. (2012) at a broad geographical range.

The macrophysical and synoptic properties of all cirrus observations are shown in Section 5.1, the radiative properties in Section 5.2, and the IWC climatology in Section 5.3.

5.1 Macrophysical and synoptic cirrus properties

The macrophysical properties of a cirrus cloud, i.e. cloud base and top height as well as physical thickness, are directly provided by the lidar measurements. They can be compared to other measurements to show whether the Leo-Lidar climatology is representative of a mid-latitude cirrus cloud dataset.

Figure 5.1 displays the frequencies of occurrence of cirrus cloud base height, cloud top height, and thickness, and the height below the thermal tropopause. In addition, climatological results from Sassen and Campbell (2001), measured at Salt Lake City ($\sim$ 1288 m a.s.l.), are shown (black dots). Panel a) shows the frequency of cloud base height derived from each averaged cloud profile. Base heights from below 4 km up to 12.5 km are observed, with the highest frequencies occurring between 6.5 and 10.5 km. The distribution is basically in accordance with the results of Sassen and Campbell (2001). In contrast, it is clearly visible that the distribution of the cirrus top height, displayed in panel b), is shifted to higher values by about 0.5 km. However, the shape of the two distributions does not differ significantly. Both have a distinct peak at around 12 km, where the tropopause is normally located at mid-latitudes. This is because the tropopause region with the coldest temperatures gives the best conditions for cirrus formation. The shift is most likely related to a generally lower tropopause height over

Salt Lake City, which can be explained by the closer distance to the location of the subtropical jet.

Panel c) shows the heights of cirrus below the tropopause derived from ECMWF temperature profiles according to the WMO criterion for the thermal tropopause. The thermal tropopause is defined as where the temperature lapse rate is first below 2 K/km and stays below this value for at least 2 km. The mean summer tropopause height is around 11.5 km, while the winter tropopause height is lower (around 10.9 km). It can been seen in panel c) that most cirrus clouds exist directly ($\pm$ 500 m) around the tropopause regardless of the season. Nevertheless, the summer distribution accumulates more around the tropopause (50 % of summer cirrus are within 0.5 km around the tropopause) than the winter distribution. In winter an accumulation of 25 % of cirrus clouds can be found around 3 km below the tropopause. Most summer cirrus clouds over the west of Germany are produced by a strong westerly frontal pattern which creates advection and hence high cirrus clouds directly below the tropopause. In addition, anvil cirrus clouds formed by strong convection also produce high cirrus clouds in summer. In contrast, the winter cirrus clouds are characterized by cold polar frontal outbreaks which generate lower cirrus clouds. Furthermore, cirrus generation by local orographic waves is uncommon for Jülich, since there is no mountainous terrain, especially in the westerly direction where the wind normally originates. The cases where cirrus clouds are observed above the tropopause are most likely due to tropopause heights in the ECMWF data which are not clearly defined or could be related to a weak first tropopause followed by a higher stronger second tropopause.

The cirrus physical thickness directly derived from cloud base and top height is shown in panel d) of Figure 5.1. Most clouds (22 %) have a thickness of around 2.25 km, but thicker cirrus up to 6 km are also observed. The observed cirrus clouds have a mean value of around 2.8 km, which is comparable to Sassen and Comstock (2001) (2.79 km), but are rather thick compared to Immler and Schrems (2002) (1.2 km) or Goldfarb et al. (2001) (1.4 km). The distribution fits well in comparison to the Sassen and Comstock (2001) climatology, despite the lack of physically thin cirrus clouds observed below 1.5 km. This lack is in accordance with observations dominated by cirrus clouds generated by advection, which creates mostly thicker cirrus (Sassen and Comstock, 2001). However, this effect could also be explained by the analysis scheme for cirrus determination used in this study. As explained in Section 4.4.5, a mean cloud profile is used and the thickness therefore corresponds to the maximum top minus the minimum base height of a cirrus layer, which might lead to an overestimation of the thickness in the case of cirrus clouds with varying top and base heights.

Figure 5.2 shows the frequencies of occurrence of temperatures at cirrus base (panel a) and top (panel b) height. Both distributions are again divided into summer and winter observations. Most cloud base temperatures are grouped around -40 to -30°C, whereas in winter there is a trend to colder temperatures. The cloud top temperatures are mostly around -60 to -50°C, particularly in summer months. In winter again colder temperatures down to -75°C

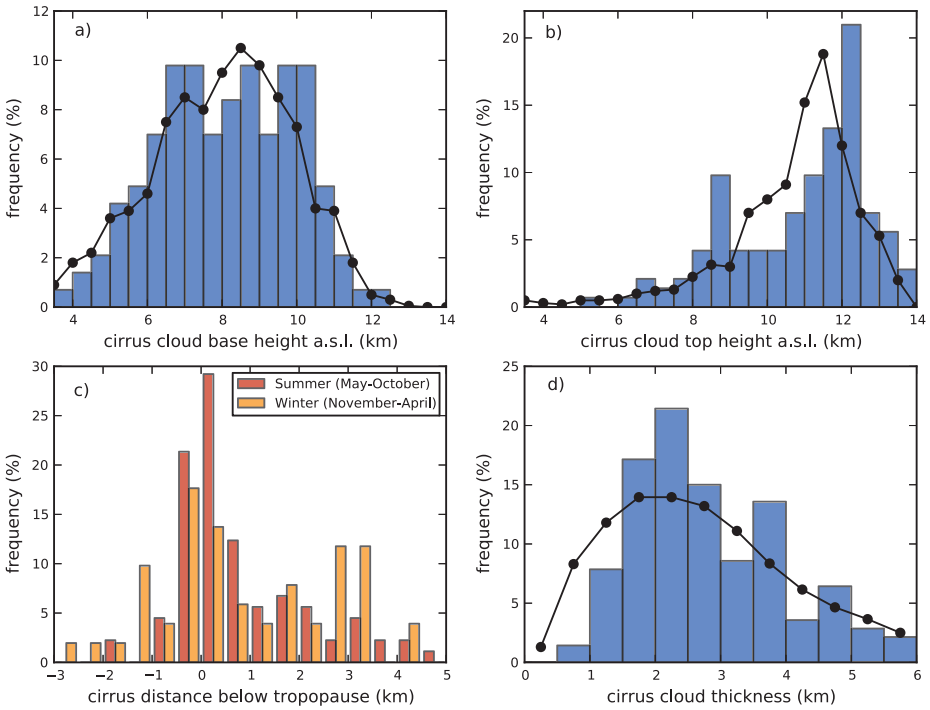

Figure 5.1: Frequency of occurrence of cirrus cloud heights using 0.5 km intervals derived from ECMWF data: a) cloud base height, b) cloud top height, c) height below tropopause divided into summer (May to October) and winter (November to April) observations, and d) thickness of cloud. Black dots represent the climatological results of Sassen and Campbell (2001) and Sassen and Comstock (2001).

are observed, since then the whole troposphere is colder. This also affects the cloud mid temperature (panel c), where the same temperature shift between summer and winter is visible. Note here that all observations at cloud mid temperatures above −35°C are related to mixed-phase clouds (see Section 2.3). Sassen and Comstock (2001) found a general increase of cloud thickness with increasing cloud mid temperature, as illustrated by the black curve in panel d). This general trend can only be partly confirmed by the Jülich observations. While thicknesses are larger than those from Sassen and Comstock (2001) for cloud mid temperatures below −50°C, they are smaller at temperatures above −30°C. However, in between the two distributions agree well. The observed larger thicknesses of cold cirrus clouds are most likely related to the above mentioned partial overestimation of physical cirrus thickness due to the cloud detection scheme and the general low data frequency at cold temperatures.

From the macrophysical point of view, the Jülich lidar climatology is largely comparable to the Sassen and Campbell (2001) climatology, despite the limited dataset of 143 observed cirrus clouds.

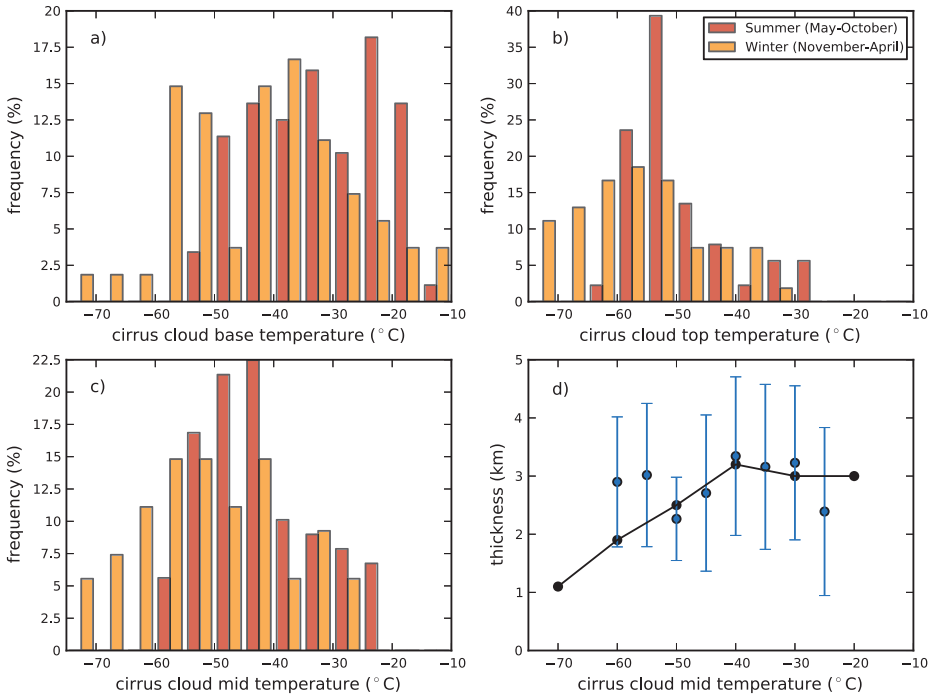

Figure 5.2: Frequency of occurrence of cirrus cloud temperatures (from ECMWF) divided into summer (red) and winter (orange) observations: a) cloud base temperature, b) cloud top temperature, c) cloud mid temperature, and d) correlation between cloud mid temperature and mean thickness of the cloud. Error bars represents the standard deviation and the black curve denotes mid-latitude cirrus from Sassen and Comstock (2001).

5.2 Cirrus radiative properties

Cirrus cloud optical depth (integrated extinction coefficient) is a crucial quantity with respect to the impact on climate (see Section 1). In general, cirrus optical depth varies over a wide range ($1 \cdot 10^{-4}$ to 50) and is extremely sensitive to the size distribution and number concentration of the ice particles. Following the classification from Sassen and Cho (1992), three different categories of cirrus optical appearance can be defined, depending on their optical depth: $\tau \lesssim 0.03$ for sub-visual, $\tau \lesssim 0.3$ for thin, and $\tau \gtrsim 0.3$ for opaque cirrus clouds. The optical depth of cirrus over Jülich is estimated by the analysis of Leo-Lidar backscatter data (see Section 4.4) and is compared to the results of the other three lidar climatologies (Sassen and Comstock, 2001; Goldfarb et al., 2001; Immler and Schrems, 2002). In addition, the lidar ratios of the Jülich observations, which constitute the important relation between extinction and backscatter coefficient, are also investigated and compared to the results of other studies.

In panel a) of Figure 5.3 the bin-normalized distribution of all observed optical depths is

displayed on a logarithmic scale. The results of the three other climatologies are also shown, (black: Sassen and Comstock (2001); orange: Goldfarb et al. (2001); red: Immler and Schrems (2002)). The detection limits of the optical depth for the Leo-Lidar are estimated to be $3 \cdot 10^{-4}$ and 3 as discussed later in Section 5.3.3. This limits the distribution, especially for higher optical depths. Smaller values are not affected since no cirrus clouds were detected below an optical depth of $2 \cdot 10^{-3}$. By comparing this distribution to the other climatologies, a generally good agreement is found. It is in especially good agreement with the distribution of Immler and Schrems (2002). The distribution of Goldfarb et al. (2001) seems to underestimate the optical depths in comparison to all the others. This is most likely because it neglects the effect of multiple scattering, which underestimates extinction or optical depth in measuring thicker cirrus cloud (see 4.4.3). This is also reflected by the mean values, where Immler and Schrems (2002) found a mean value of 0.28, Sassen and Comstock (2001) a value of 0.75, and Goldfarb et al. (2001) a value of 0.07 compared to 0.3 found in this study. More optically thick cirrus clouds are present in the climatology of Sassen and Comstock (2001), which is most likely affected by different cirrus generating mechanisms or by neglecting thin and sub-visible cirrus clouds. In this study as well as in Immler and Schrems (2002) or Immler et al. (2008), 50 % of the cirrus clouds are found to be thin or sub-visible ($\tau \lesssim 0.3$).

Sassen and Comstock (2001) reported a linear increase between cirrus physical thickness and optical depth illustrated as a black curve in panel b). Immler and Schrems (2002) found an exponential relationship of optical depth with cloud thickness, but the relation was not explicitly mentioned in their study. They suggested that optical depth is rather a function of ice particle number and/or size than of the physical thickness. In this study, the exponential relationship up to thicknesses of 4.5 km seems to be confirmed (see panel b). Above this value, lower mean optical depths are observed. However, these thick clouds are not well represented in our climatology. The significance of the values above 4.5 km thickness is therefore rather low.

In Figure 5.3 (panel c) the increase of optical depth with cloud mid temperature is shown (Jülich observation in blue; Sassen and Comstock (2001) in black). Sassen and Comstock (2001) suggested a linear trend, which is also observed here, though at somewhat lower optical depths. Hence, the slope of the relation is found to be somewhat lower, which is most likely related to the generally optically thicker clouds observed by Sassen and Comstock (2001). At cloud mid temperatures above -30°C, lower optical depth values are observed over Jülich, which could be again related to the low data frequency.

The distribution of all lidar ratios used is displayed in panel d). The mean lidar ratio is 25.2, which is in agreement with the other climatologies (e.g. 24.4 in Sassen and Comstock, 2001). The distribution is grouped very sharply around the mean value, implying that cirrus clouds with similar radiative properties concerning backscatter coefficient, extinction coefficient, and optical depth are observed.

In summary, the cirrus climatology of Immler and Schrems (2002) fits best with the dis-

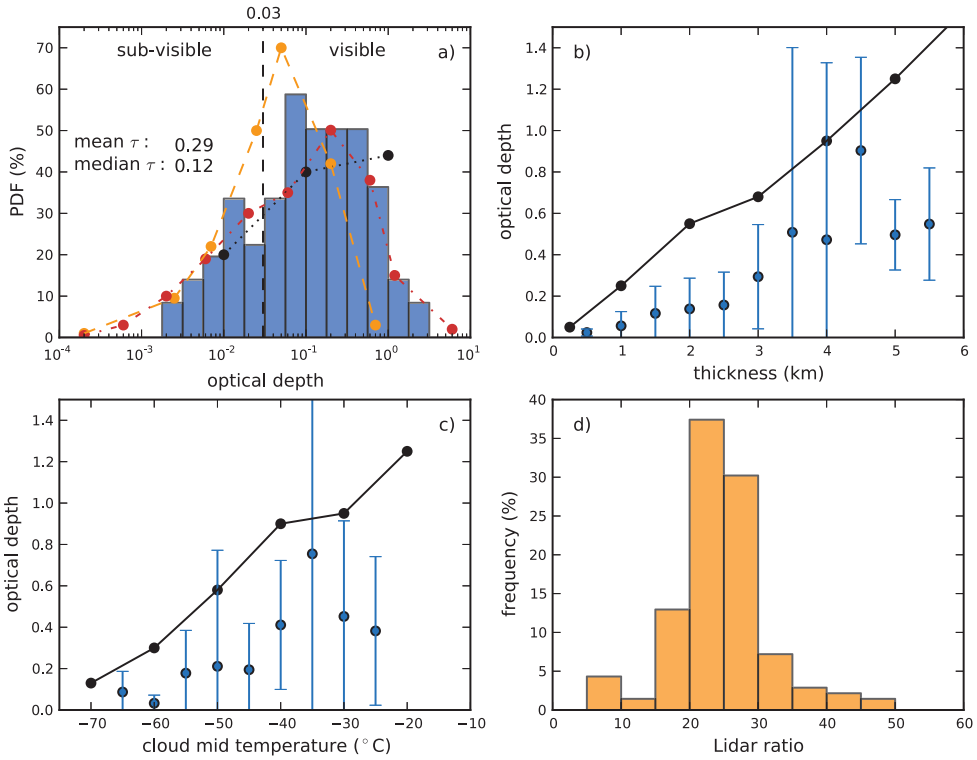

Figure 5.3: Cirrus optical properties: a) PDF of cirrus optical depth normalized to dlogτ (blue bars). Black dots represents the climatological results of Sassen and Campbell (2001), orange dots of Goldfarb et al. (2001), and red dots of Immler and Schrems (2002). Black dashed line marks the sub-visible region of 0.03 optical depth. b) Correlation between cirrus thickness in 0.5 km intervals and mean optical depth with respective standard deviation as error bar. c) Correlation between cirrus mid temperature in 5°C intervals and mean optical depth with respective standard deviation as error bar. d) Frequency of occurrence of all used lidar ratios L_{aer}.

tribution of optical depths in this study implying that the cirrus at Prestwick, Scotland, are comparable to those over Jülich and represent the whole spectrum of mid-latitude cirrus, while Goldfarb et al. (2001) underestimates thicker cirrus and Sassen and Comstock (2001) thin cirrus.

5.3 Ice water content

As shown in the last section, our data set of mid-latitude cirrus clouds is representative of all macrophysical and radiative cirrus quantities. Thus, the mean cirrus extinction profiles are used to determine cirrus IWC profiles (as described in Section 4.4.4) and to create a climatology of IWC for the respective time interval. The results of the Leo-Lidar IWC climatology are shown in Section 5.3.1. The lidar IWC data are then compared to aircraft in situ climatologies of FISH (Schiller et al., 2008; Krämer et al., 2009) and CLH (Davis et al., 2007; Luebke et al., 2012) in Section 5.3.2. Finally, the detection limits for extinction and IWC are estimated in Section 5.3.3.

5.3.1 IWC climatology

The mean IWC profiles of all observed cirrus clouds are merged to a climatology. Figure 5.4 depicts the IWC as function of temperature. Panel a) illustrates IWC occurrence frequencies for all temperatures (black). The distribution is further divided into three temperature ranges also used by Salzmann et al. (2010) and Luebke et al. (2012) for the cirrus data set presented by Schiller et al. (2008) and Krämer et al. (2009). IWC values are found in the range from the lower (0.01 ppmv) up to the upper detection limit (400 ppmv), where the most frequently observed IWC (∼9 %) is around 5 ppmv. A second smaller peak (∼6 %) can be found around 0.1 ppmv. For temperatures above 227 K, the larger IWC peak is represented more strongly than for colder temperatures (205 - 227 K), where both peaks are of the same size. Similar bimodal IWC distributions are also reported by Schiller et al. (2008) and Luebke et al. (2012), revealing two peaks at low and high IWC values. The reason for this is not clear, but is most likely caused by different cirrus generation mechanisms. Synoptically generated cirrus clouds are characterized by slow vertical velocities during evolution and result in a small ice particle number (see Section 2.2). If they are freshly formed and ice particle growth is slow, they yield rather low IWC values. Orographic or anvil cirrus clouds with stronger vertical velocities form higher ice particle numbers, which create higher IWC values. However, the exact origin of the two modal distributions can only be determined by examining the cirrus evolution of all clouds based on trajectory calculations.

The distribution of very low temperatures below 205 K is not really meaningful due to the small number of observations. Potentially existing peaks cannot therefore be determined. Nevertheless, the shift of the distribution to lower IWC values is still apparent. The temperature-dependent IWC distributions shown in panel c) reveal a general increase of IWC values with rising temperature as also reported in Schiller et al. (2008) and Krämer et al. (2009).

An estimate of the appearance of sub-visible cirrus as a function of mean cirrus IWC is shown in panel b). The mean IWC values of each cirrus profile are correlated to the cirrus optical depth divided into three temperature ranges as in panel a), but the lowest temperature interval limit is enhanced to 215 K for a better representation of the colder temperatures. Log-linear

fits for cirrus optical depth and mean IWC are shown in panel b) for each temperature interval. The sub-visible limit with an optical depth of 0.03 (dashed line) intersects the fitted functions of each temperature range. It can be seen that a temperature-dependent critical mean cirrus IWC exists, dividing the cirrus into visible and sub-visible: 0.26 ppmv for temperatures $<$ 215 K, 0.55 ppmv for temperatures 215 - 227 K, and 0.95 ppmv for temperatures $>$ 227 K.

IWC frequencies are shown in panel c) as a function of temperature divided into 2-K temperature bins. The IWC threshold for cirrus visibility is also plotted (dotted line), showing that a large part of the detected cirrus is sub-visible (32.2 %), whereas 67.8 % can be seen by eye from the Earth. Most sub-visible cirrus clouds have rather low IWC values ($<$ 0.5 ppmv) mostly at cold temperatures ($<$ 220 K), which confirms the hypothesis that frequently observed low IWC values of 0.1 ppmv are synoptically generated at cold temperatures directly below the tropopause.

5.3.2 Comparison of FISH, CLH, and Leo-Lidar IWC climatologies

The aircraft in situ IWC climatologies presented in this study were measured with the CLH instrument (Closed-path Laser Hygrometer) of the University of Colorado Boulder and the FISH instrument (Fast In-situ Stratospheric Hygrometer) of Forschungszentrum Jülich, Germany. Both instruments measure total water (gas phase + IWC) and determine IWC by subtracting the gas phase from total water as described by Krämer et al. (2009) and Luebke et al. (2012). A detailed description of the CLH and FISH instruments is given in Davis et al. (2007) and Zöger et al. (1999), respectively. Each instrument took part in several field campaigns measuring cirrus IWC. The IWC climatology of the FISH instrument is published in Schiller et al. (2008). The two IWC climatologies have been merged by Luebke et al. (2012), resulting in IWC data from 13 aircraft campaigns, comprising 67 flights and sampling approximately 38 hours of cirrus observations.

In Figure 5.5 the complete CLH and FISH IWC climatologies are shown with respect to temperature in blue and gray, respectively. Also plotted is the median IWC from Schiller et al. (2008) (confirmed by Luebke et al. (2012)) as well as the Schiller et al. (2008) maximum IWC and the minimum detectable IWC for both FISH and CLH (red dotted curves). Below this IWC, it is uncertain whether the signal stems from instrument uncertainties or from a cloud (see Krämer et al. (2009)). The Leo-Lidar measurements are plotted in orange. There is a lack of high IWC values measured with the Leo-Lidar caused by the upper IWC detection limit, which is below those of CLH and FISH. In addition, possible higher IWC values are smoothed with lower values in the same cirrus altitude due to the necessary temporal average of the lidar extinction and IWC profiles. Small IWC values are only slightly affected by this temporal averaging because of their most probable existence at cloud base and top.

The lower Leo-Lidar IWC values coincide nicely with those of the in situ dataset for temperatures $>$ 225 K. Most notably is the agreement of the data below the red dotted line,

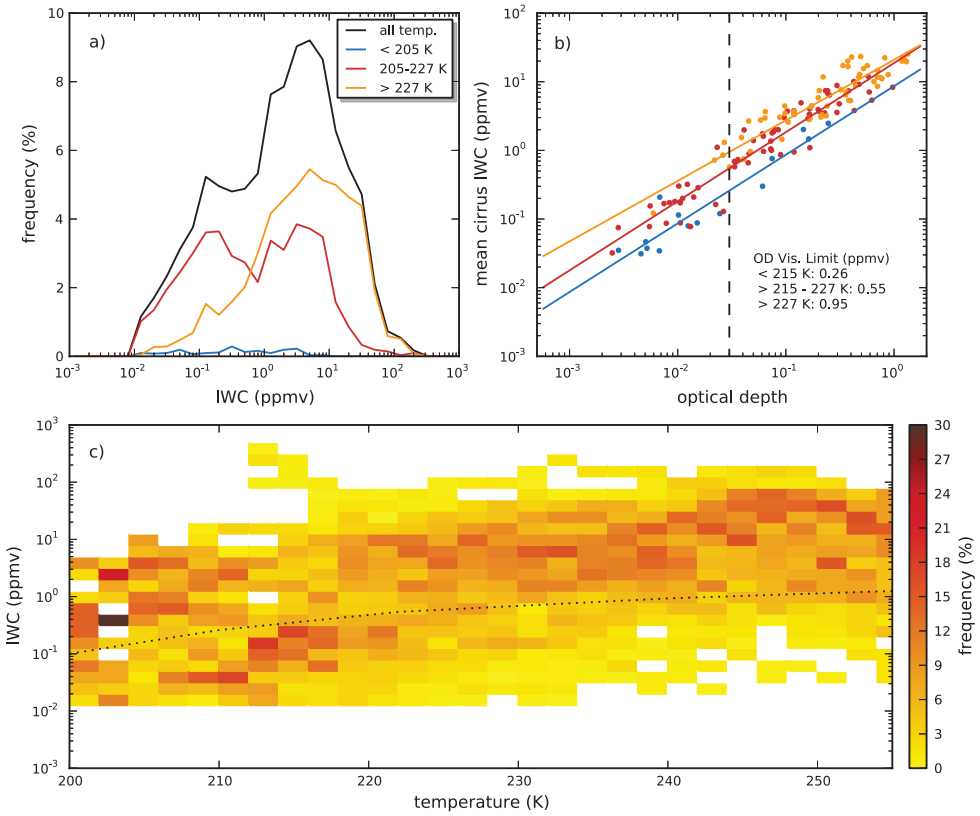

Figure 5.4: a) IWC frequency of occurrence divided into three different temperature intervals: < 205 K, 205 K - 227 K, > 227 K. b) Correlation between optical depth and mean cirrus IWC for the three temperature intervals; dashed line: sub-visible limit of 0.03. c) IWC frequencies of occurrence in 2-K temperature and 30 log equal IWC intervals; dotted line: sub-visible optical depth limit.

the minimum IWC that can be detected with a high degree of confidence by CLH and FISH. For lower temperatures, CLH and FISH measured with low certainty IWCs even smaller than those detectable by the Leo-Lidar. The whole atmospheric range of IWC values found in situ can hardly be compared, since averaged IWC profiles are considered in the Leo-Lidar observations and thus high IWC values are not included, thin cirrus could be missed in the temperature range 200 - 225 K and no measurements exist below 200 K.

However, from the comparison of the lidar and in situ IWC climatologies, there is a strong indication that the low IWC data measured with the in situ instruments are cirrus clouds and not artificial instrument effects. Moreover, it seems that the in situ instruments do not miss very thin cirrus clouds but cover the whole atmospheric cirrus IWC range.

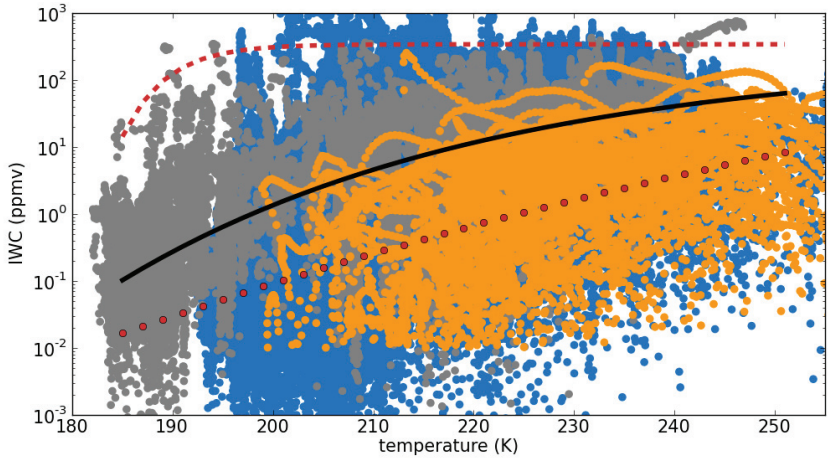

Figure 5.5: IWC as a function of temperature for CLH (blue), FISH (gray) and Leo-Lidar (orange). The red dotted lines represent the IWC maximum and minimum that can be detected with certainty by CLH and FISH (Schiller et al., 2008; Krämer et al., 2009), respectively. The back solid line is the median of the merged CLH and FISH data set.

5.3.3 Cloud detection limits

Here, the detection limits are estimated for the climatological cirrus measurements, considering that the extinction coefficient has a certain error stemming from the Klett inversion (see Section 4.3 and 4.4). In panel a) of Figure 5.6 the cirrus extinction is plotted versus its relative error. The colors of the dots also indicate relative errors. Most of the extinction data have a relative error of around 10 %. The extinction detection limit is set to a value of $6 \cdot 10^{-7}$ m^{-1} consistent with a relative error of at most 100 %. This value has the same order of magnitude as the Rayleigh extinction coefficient (see Figure 4.5). A similar value is also used in Immler et al. (2008). Therefore, the detection limit is physically meaningful, since the backscatter signals in this range are dominated by Rayleigh and no longer by particle scattering. The optical depth relative error is shown in panel b). Due to the integration over the extinction profile, the relative error is reduced to approximately 2 % for optical depths above 0.1, but increases with decreasing optical depth up to 15 %.

In panel c) the detection limits of IWC are shown. With the lidar instrument, it is not possible to detect cirrus clouds with an optical depth above 3, as also reported by Immler and Schrems (2002). Such clouds are optically so thick that no backscatter radiation from the cloud top can reach the detector. The maximum delectable IWC is determined by plotting the maximum detected IWC within each cloud profile from the climatology (orange dots) against its optical depth. Obviously, the maximum IWC is proportional to the optical depth and

a straight line can be determined which describes the maximum IWC values. This orange line crosses the limit of an optical depth of 3 (black dashed line) and thus the intersection constitutes the upper detection limit of IWC of 400 ppmv. The lower IWC detection limit is estimated by the point of intersection between the orange straight line and the lowest values of mean IWC error (blue dots), which are approximately equal to the measured IWC itself. This results in a lower IWC detection limit of $1.5 \cdot 10^{-2}$ ppmv at an optical depth of about $3 \cdot 10^{-4}$. However, obviously no cirrus cloud with such a small optical depth was observed with the Leo-Lidar over Jülich. The minimum value is found to be $2 \cdot 10^{-3}$. The lower detection limit fits well with the estimated extinction detection limit of $6 \cdot 10^{-7}$ m^{-1} by assuming a thin 500 m thick strati-formed cirrus cloud (denoted as black dashed line). In addition, the mean IWC of each cirrus profile is also displayed against the optical depth in gray dots. The mean IWC values are located between the maximum IWC values (orange dots) and the mean IWC error (blue dots).

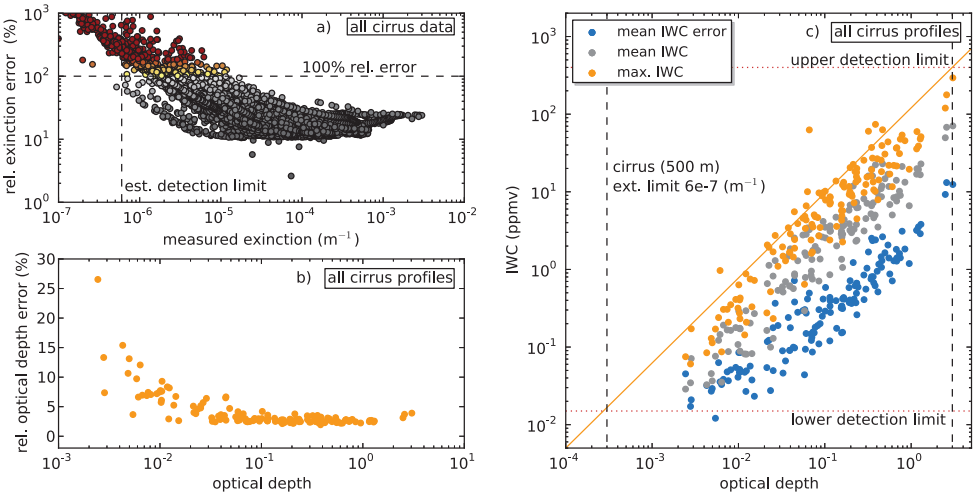

Figure 5.6: Upper and lower detection limits of cirrus extinction, optical depth, and IWC. Relative errors of: a) extinction; lower extinction detection limit is $6 \cdot 10^{-7}$ m^{-1} (dashed lines), b) optical depth. c) Maximum (orange), mean (gray), and mean error (blue) of IWC versus optical depth; minimum and maximum measurable optical depth (black dashed lines) and resulting IWC detection limits (red dashed lines).

6 Lidar observation and model simulation of a volcanic-ash-induced cirrus cloud during the Eyjafjallajökull eruption

The Eyjafjallajökull volcano in Iceland ejected a large ash cloud during its eruptions in April 2010. The cloud spread out over central Europe in a period of 6 days and severely disrupted the air traffic. The ash cloud was observed from ground (e.g. Ansmann et al., 2010; Gross et al., 2012; Seifert et al., 2011) and aircraft (e.g. Johnson et al., 2012; Schumann et al., 2011) and is well documented in several special issues (ACP, JGR, and Atmospheric Environment). Two days after the first large eruption on 14 April, we detected the ash cloud with a backscatter lidar system over Jülich, western Germany (50° 54' N, 6° 24' E). Embedded in the ash plume a cirrus cloud is also observed.

The volcanic ash event provides a good opportunity to investigate the impact of volcanic ash particles on cirrus cloud formation in the atmosphere. At the moment, there is a lack of observations, and the influence of volcanic ash on heterogeneous freezing is a matter of controversy. Some studies state that volcanic ash particles act as good ice nuclei (IN) (e.g. Isono et al., 1959; Durant et al., 2008; Fornea et al., 2009; Prenni et al., 2009), while others suggest that the volcanic ash particles have no further impact as IN (e.g. Langer et al., 1974; Schnell and Delany, 1976). The heterogeneous freezing efficiency of the Eyjafjallajökull ash particles has been investigated in two previous studies (Hoyle et al., 2011; Steinke et al., 2011). Both studies used particle probes from ground near the volcano and found only moderate effects on atmospheric ice formation. Another study by Bingemer et al. (2012) shows a large increase of the IN concentration during the Eyjafjallajökull events on two sites near the surface. All these studies are based on IN that are directly sampled from the ground or using filter probes. IN efficiency was analyzed in a laboratory simulation chamber under controlled conditions. Seifert et al. (2011) studied the influence of Eyjafjallajökull ash on cloud formation using a lidar and found periods with induced cirrus clouds embedded in ash layers. They showed the existence of very efficient IN, which form ice crystals in an environment that is relatively dry and only few percent supersaturated. The study by Seifert et al. (2011) focuses on a real atmospheric observation of an ash-induced cirrus cloud with a lidar, whereas the present paper also shows lidar observation extended by investigations on the microphysical properties of induced cirrus clouds by model simulations. The formation of the cirrus cloud is analyzed by

microphysical simulations along backward trajectories. The simulation provides information on the microphysical properties of the ash-induced cirrus cloud and conditions for the development of such clouds.

The lidar (short for light detection and ranging) measures optical properties (i.e. backscatter and extinction coefficient) and depolarization of particles at one wavelength with a high vertical resolution. In the depolarization channel, it is possible to distinguish various shapes of observed particles.

Periods with or without volcanic ash occurred in accordance with the dynamic situation. The largest amount of ash was found above the planetary boundary layer, below seven km, in the free troposphere (Ansmann et al., 2010; Schumann et al., 2011). However, during some periods, our measurements show an increased depolarization and particle extinction signal at higher altitudes. This may have been due to pure volcanic ash, ice crystals or a mixture of the two. In this study, we investigate in detail one of the observed cirrus cloud embedded in a volcanic ash layer. First, the origin of the observed air mass is assigned by calculating ECMWF (European Centre for Medium-Range Weather Forecasts) backward trajectories. With our detailed microphysical box model MAID (Model for Aerosol and Ice Dynamics) (Bunz et al., 2008), we simulate the ice formation along these trajectories. Thus it is possible to distinguish observations from pure volcanic ash, natural cirrus, and induced cirrus clouds. Furthermore, microphysical and optical properties of the resulting ice crystals where investigated with this combination of lidar and model simulations.

In the first section, methodology details of the lidar measurements and the model simulation relating to the volcanic ash period are described. In Section 6.2, the observation of the main Eyjafjallajökull volcanic ash cloud and the induced cirrus on 16 April 2010 is presented. The origin of the air masses is analyzed based on trajectory calculations. Subsequently, the IN concentration is estimated from lidar data. The simulation of induced cirrus with MAID, including two sensitivity studies, is described and discussed accordingly.

6.1 Instrumentation and methodology

The Leo-Lidar is used for the observation of the induced cirrus cloud (for details see Section 4.2). The lidar measure profiles of extinction coefficients and depolarization which is representative for the asphericity of the scattering particles. Cirrus clouds or ash particles mostly create a large signal in the depolarization because of their non-spherical shape. The depolarization of Eyjafjallajökull ash particles is somewhat lower than for ice crystals (Ansmann et al., 2011). The extinction is approximately proportional to the concentration and effective particle size of volcanic ash, but also proportional to the ice water content (IWC) of a cirrus cloud. To determine the particle backscatter and extinction coefficient from the backscatter signals we have to assume the lidar ratio L_{aer} (see Section 4.3). During the Eyjafjallajökull eruption, many lidar stations in Europe measured the ash cloud and the lidar ratio with Raman lidar

systems. Ansmann et al. (2010) specified a lidar ratio of 55 to 65 sr for a wavelength of 355 nm. We therefore assume a lidar ratio of 60 sr for the conversion of backscatter coefficient into particle extinction in our analysis. The multiple-scattering correction (see Section 4.4.3) is applied for pure ash extinction profiles with an effective radius of 1 µm figured out in Gasteiger et al. (2011). For ice crystals and the induced cirrus cloud, the effective radius from model simulation was used and is around 10 µm. Finally, we use at least an average over 12000 single laser pulses measured in a time interval of 10 minutes with 150 m vertical resolution for determination of extinction profiles.

To investigate the effect of ice formation on volcanic ash particles in the atmosphere, we combined lidar measurements with additional information obtained from microphysical simulations with the model MAID (see Section 3). For this work, the important initialization input parameters are the amount of water vapor as well as the number concentration, the size distribution, and the freezing threshold of the IN. MAID simulations are performed along ECMWF backward trajectories, where trajectory preparation is done as described in Section 3.2 by considering possible dry bias of ECWMF data and temperature fluctuations which have an amplitude of around 0.3 to 0.5°C in this study. The comparison of the model output with the lidar observations over Jülich is based on the modeled IWC. Equation 4.25 in Section 4.4.4 is used to calculate extinctions which can be directly compared to observed extinctions.

6.2 The Eyjafjallajökull ash plume

6.2.1 Lidar observation

Shortly after news of the Eyjafjallajökull eruption and the propagation of a volcanic ash cloud over central Europe on 16 April 2010 we started to operate the lidar at Jülich. And once low-level clouds over Jülich disappeared completely at around 18:00 UTC it was possible to observe the volcanic ash up to 10 km. The lidar measurements are shown in Figure 6.1 by particle backscatter coefficients derived from five-minute averaged data. Starting from the ground to the top, one can see the planetary boundary layer (PBL) up to 1.6 km altitude. It is characterized by an increased backscatter coefficient below the main volcanic ash layer (MVL) in the 1.6 to 3 km altitude range. Both the high backscatter values in the PBL and MVL indicate a high concentration of particles. Mixing of volcanic ash with boundary layer air or sedimentation of larger ash particles has probably taken place and created a high particle loading in the upper part of the boundary layer. High particle depolarization values of 32.5 % are observed in the MVL and are similar found by others with values of 35 to 38 % (Ansmann et al., 2011; Chazette et al., 2012; Gross et al., 2012).

Above this main ash layer, a weaker secondary layer is visible around 4 - 5.5 km. Above this weak second layer, an apparent third layer with an increased backscatter coefficient exists. This structured layer represents a cirrus cloud embedded in an ash layer (marked as volcanic-ash-

induced cirrus). This layer differs from the other ash layers below, with a concurrent increased volume depolarization, which indicates more or larger aspherical particles such as ice crystals. Another aspect also implies the presence of ice crystals. The Klett inversion is either done with forward and backward integration assuming reference heights about 11-12 km and 7 - 7.5 km, respectively. The Klett inversion with backward integration results in negative backscatter and extinction coefficient if a lidar ratio of 60 sr (pure volcanic ash) is assumed. This lidar ratio indeed suggests the presence of a cirrus cloud instead of pure volcanic ash. Only a lower lidar ratio of 25 sr, often found in cirrus, provides realistic results for both Klett solutions. For later considerations, the extinction of the cirrus is determined with this lidar ratio.

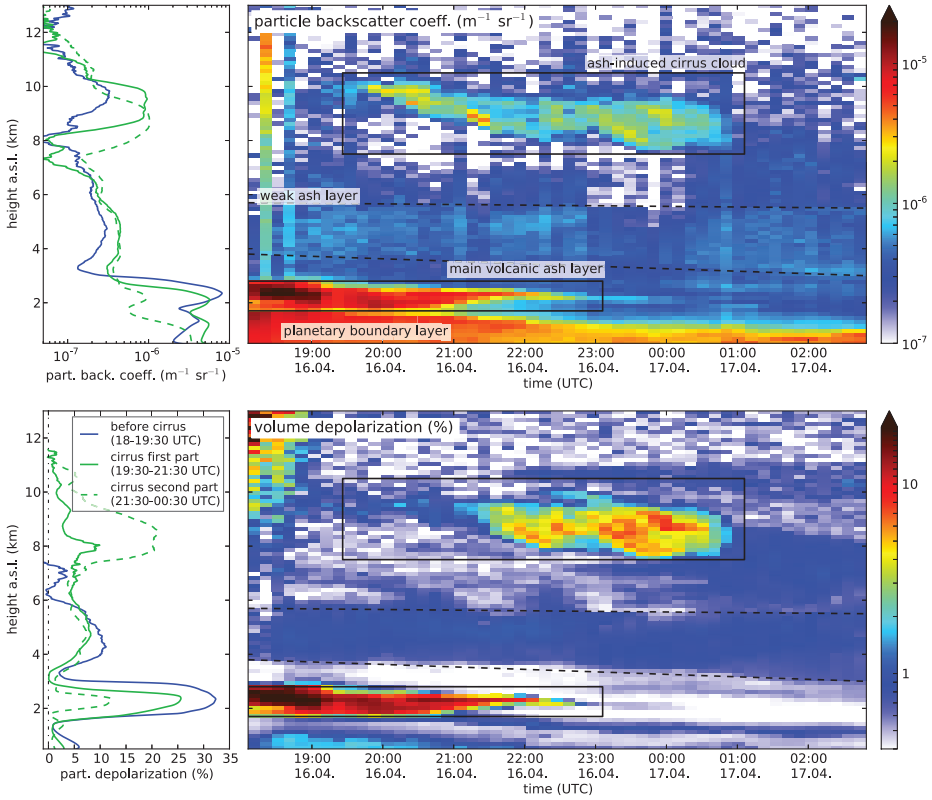

Figure 6.1: Particle backscatter coefficient (assuming a lidar ratio of 25 sr) and volume depolarization measured with backscatter lidar Leo-Lidar on 16. - 17.04.2010 (18:00 - 03:00 UTC) averaged over 5 min of data. Three layers of particles are visible: the main volcanic ash layer between 1.6 - 3.0 km, a second weak layer in 4 - 5.5 km, and a layer in the 8 - 10 km region, which includes a cirrus cloud. In addition, profiles of backscatter coefficient and particle depolarization are shown in the left panels obtained from averaged data before cirrus occurrence (18-19:30 UTC, lidar ratio of 60 sr) and two profiles of the first (19:30 - 21:30 UTC) and second (21:30 - 00:30 UTC) part of the induced cirrus cloud (lidar ratio 25 sr).

Between 19:30 and 21:30, only a weak particle depolarization lower than 5 %, but a high backscatter signal is found in cirrus cloud between 8 and 10 km. This is unusual for ice crystals. In comparison, the particle depolarization after 21:30 is around 20 %. The low volume depolarization in the early phase of observation suggests spherical particles such as droplets. However, liquid water droplets does not exist at temperatures below −35°C. But, this behavior is also found by other lidar observations during the Eyjafjallajökull period (Seifert et al., 2011). The most likely reason for this is the occurrence of specular reflection.

In the time period of the occurrence of volcanic ash, the lidar system measured in the zenith orientation. In the case of planar planes of horizontally oriented ice crystals, specular reflection appears (e.g. Westbrook et al., 2010; Sassen and Benson, 2001), which results in a high backscatter coefficient and a low depolarization ratio. Specular reflection occurs under conditions where large planar ice crystals are formed and align horizontally during sedimentation. This is mostly the case for warmer conditions in moist air with temperatures between -8 and −25°C, where ice crystals can grow to sizes around 50 to 100 ¯m in radius. In the time period between 19:30 and 21:30 the air was mostly cold and relatively dry with temperatures around −50°C and 105 % rel. humidity with respect to ice in the cirrus region (see Section 6.2.2 and Figure 6.3). Ice simulation (Section 6.2.4) shows the development of rather small ice crystals around 10 ¯m in radius in a volcanic ash environment. However, the are also observations were specular reflections occurs under colder conditions below −30°C as reported by Noel and Chepfer (2010). Indeed, these observations are very rarely, but indicate that sedimentation of ice crystals can occur under cold conditions producing specular reflection when a zenith pointing lidar is used.

6.2.2 Trajectory analysis

For the observation time between 18:00 to 03:00 UTC, we calculate around 2000 single trajectories in the altitude range between 1 and 12 km. The time interval between two trajectories is 15 minutes and the altitude resolution is 200 m. The probability density function (PDF) at each location of all trajectories is shown in Figure 6.2 a) for a latitude/longitude grid with a resolution of 0.2 x 0.2 degrees. Since the observed air mass must contain volcanic ash particles to form an induced cirrus, the trajectories have to be close to the Eyjafjallajökull volcano. This is indeed the case as shown in panel a). The figure implies that the most trajectories could contain volcanic ash particles as shown by the lidar observations. In panel b), c), and d) of Figure 6.2 we performed a trajectory analysis to confirm possible ash loadings of air masses and to estimate the possibility of cirrus cloud occurrence. These figures have the same altitude and time scale as the lidar data from Figure 6.1, so that it is possible to compare both figures easily. In addition, the range in which the induced cirrus cloud occurred at the observational site is framed by a black box.

In panel b) the shortest distance to the volcano for each trajectory sampled at Jülich is

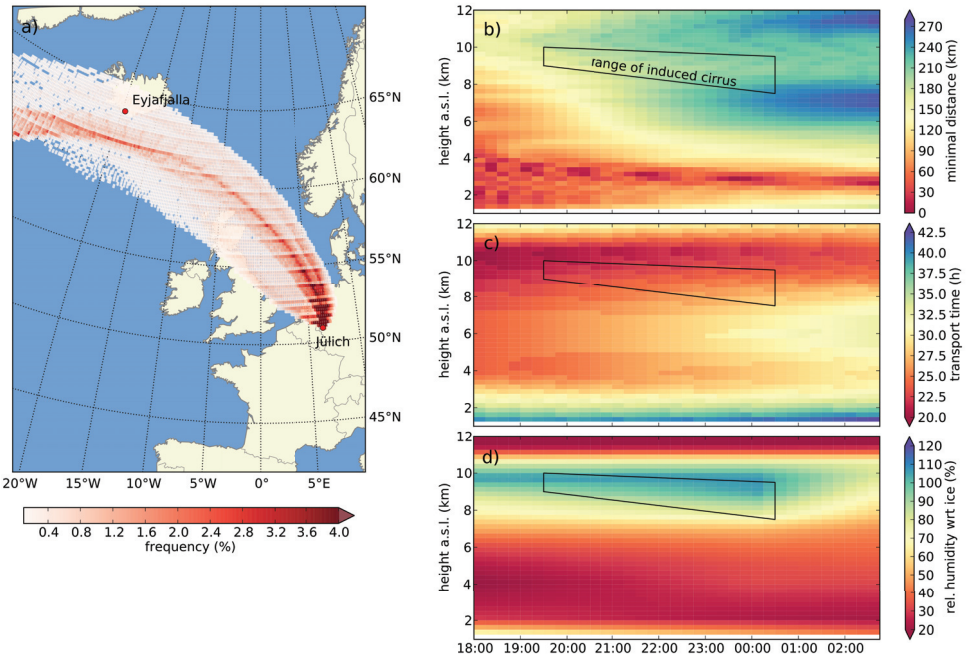

Figure 6.2: Backward trajectories started at a specific time and altitude in Jülich and show where the air mass originates: a) Probability density function of all calculated trajectories, b) minimal distance of each trajectory to the Eyjafjallajökull volcano, c) transportation time from minimal distance, and d) relative humidity with respect to ice at the end of each trajectory over Jülich.

shown. A layered structure between 2 and 4 km, which has the shortest distances between 0 and 60 km to the volcano, is clearly visible in panel b). This structure represents the main volcanic ash layer, which is also visible in the lidar data. The second layer in an altitude range from 8 - 11 km, with distances between 90 and 160 km, can also be identified. This structure coincides with the cirrus observation assumed in Section 6.2.1. Thus the air masses in the region under consideration could potentially contain volcanic ash and the particles could serve as IN. In panel c) the transport time from the shortest distance to the lidar site shows the same behavior with the two main layers. Short transportation times of around 24 hours are visible which are in accordance to Dacre et al. (2011). In addition to the IN occurrence, the relative humidity with respect to ice is important for cirrus formation and persistent behavior of the ice crystals. Thus in panel d) of Figure 6.2 the relative humidity with respect to ice is shown. A blue shaded layer from 8 to 11 km is clearly visible. This layer shows values slightly above 100 % rel. humidity and in principle ice crystals can occur in this layer. However, the air masses are only a few percent supersaturated. This implies low freezing thresholds and

therefore the existence of very efficient IN in the volcanic ash layer.

Figure 6.3 shows mean profiles of ECMWF temperature and rel. humidity for three different time intervals (16 April 20:00 UTC; 17 April 00:00 and 01:30 UTC). In addition, one radiosonde launched by DWD (German Meteorological Service) station Essen, 70 km north west of Jülich at 00:00 UTC on 17 April is shown. The relative humidity data are dry bias corrected with an algorithm provided by Miloshevich et al. (2009). The humidity profiles illustrate a rather good agreement between the ECMWF data and the radiosonde data and rule out the existence of high ice supersaturations. Small discrepancies can be explained by the distance of the launch site from the corresponding ECMWF grid point. Further, the profiles show again that air masses between 8 and 10 km are only a few percent supersaturated and would suggest no cirrus occurrence under normal clean air conditions. The temperature range from -45 to -55°C between 8 and 10 km is clearly in the range of possible deposition freezing.

All in all, the trajectories can be used for model simulation of the induced cirrus cloud and the ECMWF data are sufficient for this purpose.

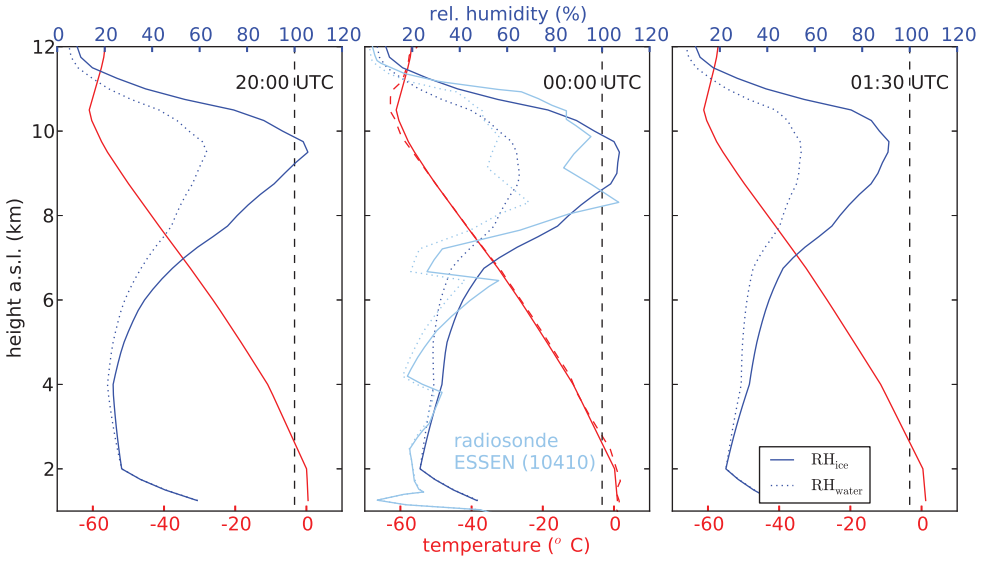

Figure 6.3: Profiles of temperature and rel. humidity with respect to water (RH_{water}) and ice (RH_{ice}) at Jülich from ECMWF data (16.04.2010 at 20:00, and 17.04. at 00:00, and 01:30 UTC) and a radiosonde launched in Essen (station code 10410) on 17.04. at 00:00 UTC.

6.2.3 IN properties

Ice formation depends strongly on the ambient conditions of the air mass. Especially the concentration and microphysical properties of aerosol particles, which can serve as IN, have a strong impact on heterogeneous freezing. Both affect also the number concentration of ice crystals and therefore the IWC or the extinction. Thus it is important to know the IN concentration and freezing threshold as precisely as possible to compare the lidar extinction with MAID simulation results in a meaningful manner.

However, the total particle concentration alone can also be estimated from the extinction profile measured with the lidar. The particle concentration can be obtained by applying an extinction to the particle concentration conversion factor. Seifert et al. (2011) used a conversion factor of 0.5 to $1 \cdot 10^{-6}$ m/cm^3, from a study of Ansmann et al. (2008) for Sahara dust particles with radii > 250 nm. Seifert et al. (2011) discussed the fact that the conversion factor for volcanic ash should be similar. Since it is not possible to determine the ash particle concentration during cirrus occurrence, the lidar observations directly before and after the cirrus cloud are used. It is assumed that the ash particle concentration is comparable during cirrus occurrence. The extinction profile derived from averaged data before cirrus occurrence (18:00 to 19:30 UTC) and after cirrus occurrence (01:15 to 03:00 UTC) is shown in Figure 6.4 for a lidar ratio of 60 sr. It is further assumed that the air masses observed in these time intervals do not contain ice crystals. This is justified by a low backscatter coefficient and a low volume depolarization visible between 18:00 and 19:30 UTC in the 8 to 10 km height range in Figure 6.1. Figure 6.4 b) illustrates the conversion from extinction to particle concentration with a mean conversion factor of $0.75 \cdot 10^{-6}$ m/cm^3 and the range of conversion in the blue shaded area for the profile before cirrus occurrence. The total uncertainty including the uncertainty of extinction and the conversion factor is shown as a reddish shaded area. Ash particle concentrations in the range from 10 to 25 cm^{-3} are found before cirrus occurrence, while concentrations around 5 cm^{-3} are found after cirrus occurrence.

Besides the lidar measurements, the most precise measurements of particles can be made with an aircraft probing the ash cloud in situ. During the Ejyafjalla ash period, the German research aircraft DLR Falcon probed the ash cloud on 19 April over Leipzig, Germany (Schumann et al., 2011). In a dive flight pattern a vertical profile of the ash layer is investigated. In an altitude range from 4 to 5.5 km, an ash particle concentration of about 15 cm^{-3} was found in the size range from 250 to 1000 nm. The concentration of larger particles > 2 $^{-}$m in the same air volume was 0.4 cm^{-3}. Lower concentrations of around 5 cm^{-3} were found at cirrus altitude during the dive, which is in accordance to lidar observations of Seifert et al. (2011) on 18 April over Leipzig. Although these measurements were taken over Leipzig on 18 and 19 April, these measured concentrations are in good agreement with the estimation from the lidar observations.

However, even a realistic determination of the particle concentration does not directly yield

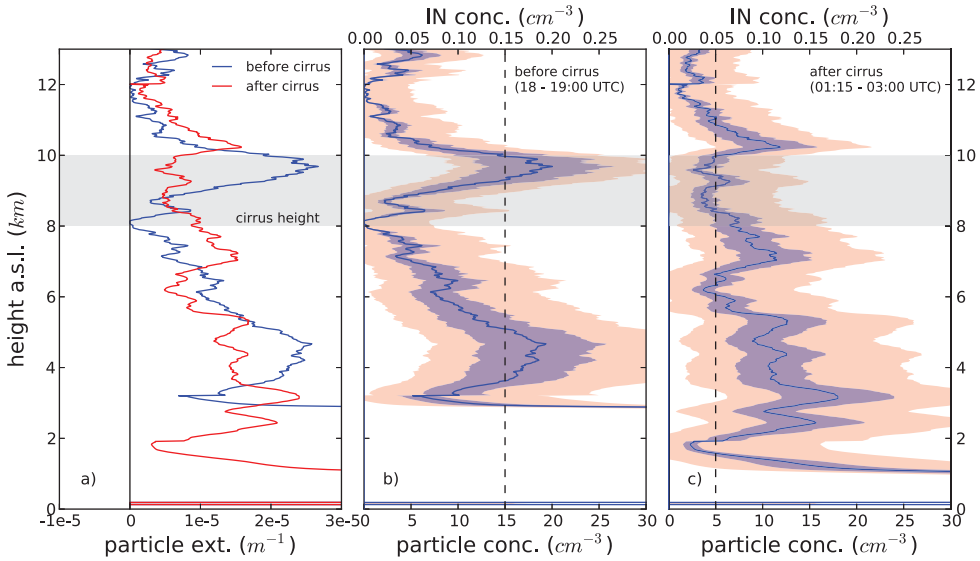

Figure 6.4: a) Lidar extinction profile obtained from averaged data before (blue, 18:00 to 19:30 UTC) the cirrus occurrence and after the cirrus occurrence (red, 01:10 to 03:00 UTC). Corresponding extinctions converted to particle concentration profiles are shown in b) and c), respectively. A scale for IN concentration is given at the top of b) and c), assuming an IN concentration of 1 % of total particle concentration.

the IN concentration. Steinke et al. (2011) analyzed freezing experiments with Eyjafjallajökull ash probes in an atmospheric simulation chamber. They found that around 1 % of the ash particles were very efficient IN with freezing thresholds around 110 % rel. humidity with respect to ice at a temperature of −48°C in the deposition freezing mode. Therefore we assume in our analysis that 1 % of the ash particles serve as IN. The IN concentration taking 1 % of the particle concentration before and after cirrus occurrence is also displayed in Figure 6.4 b) and c) at the top axis. The profile before the cirrus occurrence shows an increased particle concentration from 8 to 11 km with an IN concentration of 0.12 cm^{-3} to 0.25 cm^{-3} in the altitude range of the induced cirrus cloud (marked as a gray shaded area from 8 to 10 km). The profile after the cirrus occurrence clearly indicates a lower IN concentration of 0.05 cm^{-3} in the altitude range of the cirrus cloud. Although the IN concentration above 10 km stays almost constant in comparison to the profile before cirrus occurrence, the IN concentration increases below 8 km. Obviously, the ash layer descends within the time interval shown in Figure 6.4 and leaves the supersaturated region between 8 and 10 km shown in Figure 6.2. The decreasing top height of the cirrus from 10 to 9 km, visible in the temporal progress of the cirrus cloud in the lidar observations (see Figure 6.1), confirms the descent of the ash layer. The strong backscatter coefficients in the first part (19:30 to 21:30 UTC) of the cirrus cloud indicates a higher ice particle concentration and therefore a higher IN concentration than the

rest of the cirrus cloud. This is in accordance with the estimated concentrations before and after the cirrus occurrence. An IN concentration of 0.10 cm^{-3} obtained from the mean of both profiles before and after the cirrus occurrence is close to the values found by induced cirrus lidar observation from Seifert et al. (2011). Therefore a suitable assumption for the simulation of the volcanic-ash-induced cirrus is a high IN concentration of 0.1 cm^{-3}. This IN concentration is around 10 times higher than under normal conditions (DeMott et al., 2010) and implies a modification of the microphysical behavior of ice formation.

Besides the IN concentration, the freezing efficiency or freezing threshold is also important for the simulation of the induced cirrus cloud. Older laboratory studies by Durant et al. (2008) and Fornea et al. (2009) regarded volcanic ash from other volcano eruptions as very efficient IN. Steinke et al. (2011) as well as Seifert et al. (2011) suggest efficient IN during the Eyjafjallajökull ash period. Due to these findings, the assumption of a low freezing threshold for the heterogeneous deposition freezing slightly below 110 % is also justified in general. The freezing threshold is estimated in detail in section 6.2.4 with the help of a model-based case sensitivity study in comparison to the lidar observation.

Another property used for the ice formation study is the size distribution of volcanic ash. For volcanic ash particles we use a mono modal log-normal distribution with a width of 1.7 σ, minimal radius of 0.1 $^{-}$m and maximum radius of 5 $^{-}$m. This values are similar to the outcome of inverted lidar and photometer data from Gasteiger et al. (2011) or aircraft in situ measurements (Johnson et al., 2012; Schumann et al., 2011).

As described in Section 6.1, MAID simulations are performed for each trajectory with the input parameters water vapor, IN concentration, and freezing threshold. The temperature and pressure along the trajectory are taken from ECMWF data. The following two subsections present model sensitivity studies to reproduce and explore the observed cirrus and a comparison between the simulated and the observed cloud.

6.2.4 Model sensitivity studies

Case study

The case sensitivity study was performed to determine the set of input parameters which provides the best representation of the cloud extinction measured by the lidar. For this study, 20 representative backward trajectories were used starting at different altitudes and times with a focus on the time period at the beginning of the cirrus occurrence. About 10000 single MAID runs were made with a different sets of input parameters. The parameter space of the initialization covers 7 IN concentrations (0.01, 0.03, 0.09, 0.1, 0.2, 0.5, and 1.0 cm^{-3}), 5 freezing thresholds (105, 110, 115, 120, and 130 % rel. humidity with respect to ice), and 7 water vapor initializations (90, 100, 110, 120, 130, 140, and 150 in % of mean ECMWF water vapor along the trajectory). Each trajectory was simulated with two different sets of temperature fluctuations as described in Section 3.2.

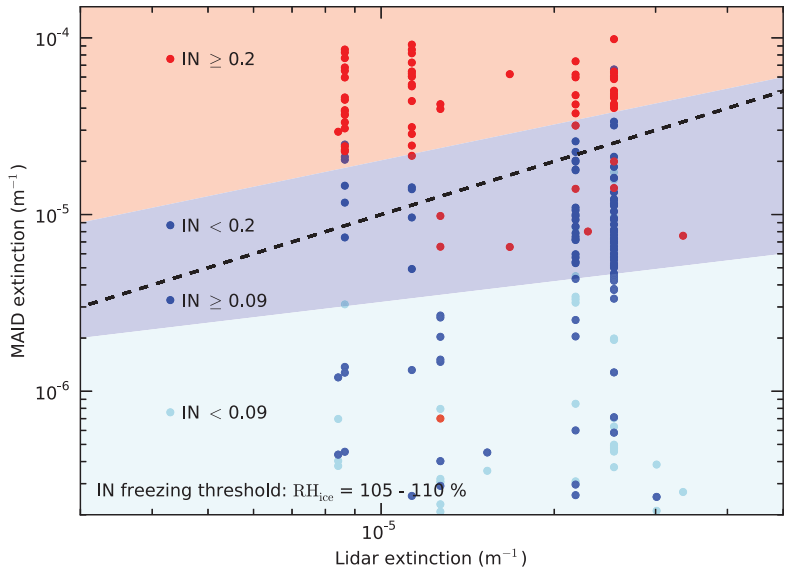

Figure 6.5: Comparison of MAID and lidar extinction to find IN concentration with high IN concentration in red (≥ 0.2 cm^{-3}), medium in blue (0.09 - 0.2 cm^{-3}), and low in light blue ($<$ 0.09 cm^{-3}). The black dashed curve represents the 1:1 line between lidar and MAID extinction. The freezing threshold of the IN is set to 105 - 110 % RH$_{ice}$.

In none of the model runs homogeneous freezing occurred after the heterogeneous freezing event even with the superimposed temperature fluctuations. These fluctuations seemingly play only a minor role in the ice crystal formation process at low cooling rates and high loading of effective IN.

The results of all model runs were compared with the lidar extinction by calculating the extinction based on the IWC as explained in Section 6.1. The best agreement with the lidar observation is obtained for the parameter sets with high IN concentrations of 0.09 - 0.2 cm^{-3}, a freezing threshold around 105 to 110 %, and with a water initialization of 100 % ECMWF water vapor.

Figure 6.5 illustrates the influence of IN concentration relating to the extinction. Both MAID and lidar extinctions are plotted against each other. Only trajectories with volcanic ash conditions, low freezing threshold in the range of 105 - 110 % rel. humidity and water vapor less than 110 % from ECMWF are considered. Most of trajectories produce ice crystals independent of the IN concentration. However, the resulting extinction strongly depends on the number of IN. If the model is initialized with high IN concentration more ice crystals can be formed resulting in a higher extinction signal than the observation. Analogously, a low IN concentration results in fewer ice crystals and a low extinction (light blue dots in light bluish area). In addition, a small IN concentration results in larger ice crystals that can sediment out

before reaching the site of observation. As shown in Figure 6.5, the best agreement between MAID and lidar extinction is found for a range of IN concentration from 0.09 to 0.2 cm^{-3}. This fits well with the estimated concentration from the lidar observation before the cirrus cloud derived in Section 6.2.3, which was of the order of 0.1 to 0.2 cm^{-3}. The lidar observations after the cirrus occurrence are compatible with somewhat lower IN numbers (down to 0.05 cm^{-3}) and suggest some variation of IN concentration over time.

During the Eyjafjallajökull ash period, the air in the cirrus region was mostly relatively dry (see Section 6.2.2 and Seifert et al. (2011)) and at most only a few percent supersaturated. Ice formation only occurred in the presence of very effective IN (e.g. volcanic ash), allowing a low freezing threshold below 110 %. Trajectories show that ice formation also occurs with higher water vapor initialization above 110 % of the ECMWF mean value. However in fact the ECMWF data agree well with the radiosonde profile in Figure 6.3 and Seifert et al. (2011) show similar humidity profiles over Lindenberg and Meiningen, Germany. ECMWF water vapor is thus suitable for the model initialization and can reproduce ice formation in the volcanic ash environment in accordance with the lidar observations. Under these circumstances, a cirrus cloud was only formed under volcanic ash conditions.

The possible impact of volcanic ash as IN on cirrus micophysical properties is shown in Figure 6.6 where model results of ice particle numbers and sizes for various IN concentrations and freezing thresholds (see color code in Figure 6.6) are plotted. The results of the model runs can be split up into two regimes denoted as normal and volcanic ash IN conditions.

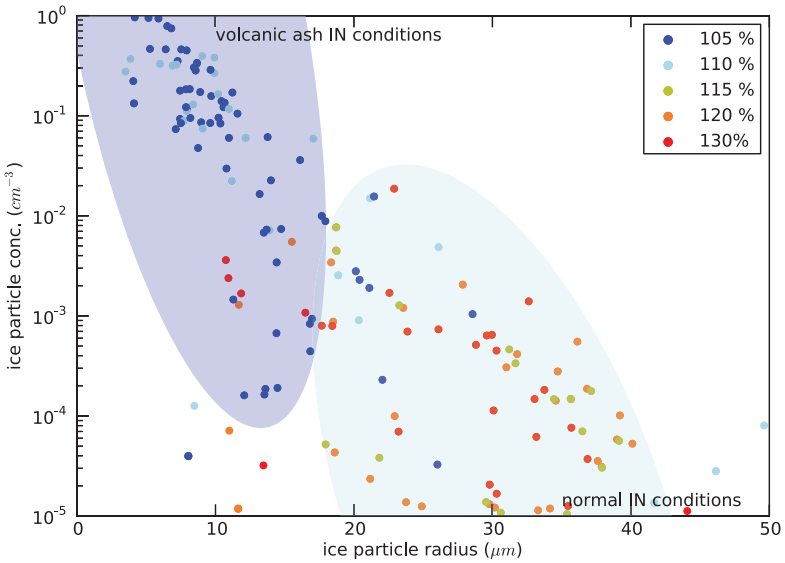

Figure 6.6: Impact of volcanic ash on mean ice particle radius and number concentration. The color represents the freezing thresholds.

Under volcanic ash IN conditions (blue shaded area) with a freezing threshold of 105 to 110 % (blueish dots) more but smaller ($r_{ice} \sim 10$ µm) ice crystals appear than under normal IN conditions (light blue shaded area, $r_{ice} = 20$ - 40 µm) with a freezing threshold higher than 110 % (yellow-reddish dots). This implies that a high loading of volcanic ash can alter the microphysical and thus radiative properties of cirrus such that instead of a cloud with few large crystals a cloud having many small crystals forms. Moreover, it can happen that the presence of volcanic ash even allows a cirrus cloud to form.

Idealized simulations

For a more general view on the change of cirrus properties with the concentration of efficient IN, we compared in another set of idealized MAID sensitivity runs the number of ice crystals appearing from heterogeneous ice nucleation (with possible subsequent homogeneous freezing) for normal and polluted IN conditions. In Figure 6.7, the ice crystal numbers nucleated for vertical velocities (w in cm/s) ranging from 1 cm/s up to 10 m/s are shown for temperatures varying between about −60°C and −35°C, i.e. the mid-latitude cirrus range is covered by these sensitivity runs. Here, MAID is driven by constant vertical velocities (i.e. constant temperature and corresponding pressure changes) and is initialized with an amount of water corresponding to $RH_{ice} = 90$ %. Small scale temperature fluctuations are not superimposed in these simulations since from the case study it became obvious that these fluctuations do not

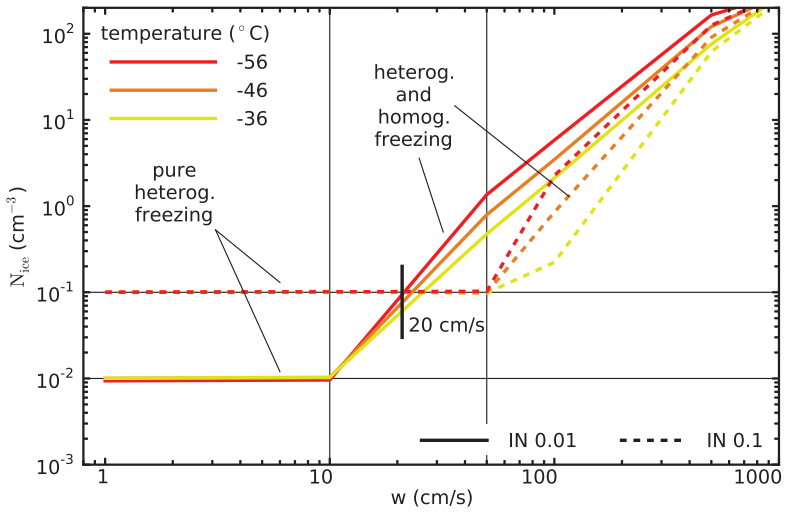

Figure 6.7: Ice crystal numbers vs. vertical velocity w (cm/s) from idealized MAID sensitivity runs for normal and polluted IN conditions (IN number 0.01 and 0.1 cm^{-3}) and three temperatures. The freezing threshold is at $RH_{ice} = 110\%$. Note that the ice crystal numbers are identical in case of a higher freezing threshold, but that the formation temperature (indicated in the legend) would be lower. For more detail see text.

trigger a second homogeneous freezing event. Figure 6.7 shows the results for IN concentrations of 0.01 cm^{-3} (normal conditions) and 0.1 cm^{-3} (polluted conditions), which corresponds to the observed volcanic ash induced IN number. The resulting ice particle numbers in the idealized model runs are quite similar to former studies of Karcher et al. (2006), Gierens (2003), and Spichtinger and Cziczo (2010).

Under normal conditions the ice crystal numbers are identical to the IN number (pure heterogeneous freezing) for small vertical velocities below 10 cm/s and for all temperatures (Figure 6.7, solid lines). That means that the updraft is not strong enough to raise RH_{ice} up to the homogeneous freezing threshold after the heterogeneous ice nucleation event. Note that in these cases homogeneous freezing would produce fewer ice crystal than the heterogeneous. For higher vertical velocities, the ice crystal numbers increase due to a second homogeneous freezing event, producing more ice crystals the higher the vertical velocity and the colder the temperature is, as expected for the homogeneous freezing process.

The high amount of IN in the polluted case also leads to an identical ice crystal number, but up to vertical velocities of about 50 cm/s (Figure 6.7, dotted lines). This is since the many ice crystals can deplete the water vapor more efficiently and thus stronger updrafts are necessary to increase RH_{ice} up to the homogeneous freezing threshold. For higher vertical velocities the same behavior as in the normal case is seen, but with slightly lower ice crystal numbers.

Comparing the two scenarios it can be seen that for updrafts smaller than about 20 cm/s the microphysical properties of cirrus clouds are generally influenced by a high loading of IN in the way we observed it in our volcanic ash case study, namely that cirrus with more -but smaller- ice crystals appear. For higher vertical velocities the picture reverses: now the ice crystal numbers in the polluted cirrus are smaller than those of the normal cirrus, but approaching to each other with increasing updraft. For comparison, the large scale vertical updrafts in the case of the ash-induced cirrus were rather small with values around 1 cm/s and a standard deviation of around 0.5 cm/s. In summary it can be seen that cirrus clouds can be modified by a high number of heterogeneously freezing efficient IN over nearly the complete atmospheric updraft range.

6.2.5 Comparison of the observed cirrus cloud with model simulations

The case sensitivity study, described in the previous section, shows that volcanic ash particles are necessary to reproduce the observed extinction or cirrus cloud. An interesting question is whether the whole cloud can be reproduced by the model and ECMWF data. To answer this question we calculated backward trajectories from 18:00 to 03:00 UTC with 15 minutes time and 200 m vertical resolution. To capture the whole height range of the cirrus and ash occurrence the trajectories are calculated from 7 to 11 km. Again five different sets of temperature fluctuations are used for each trajectory to account for temperature variability not captured by ECMWF. A total of 3600 single MAID runs results in a 2D picture of the

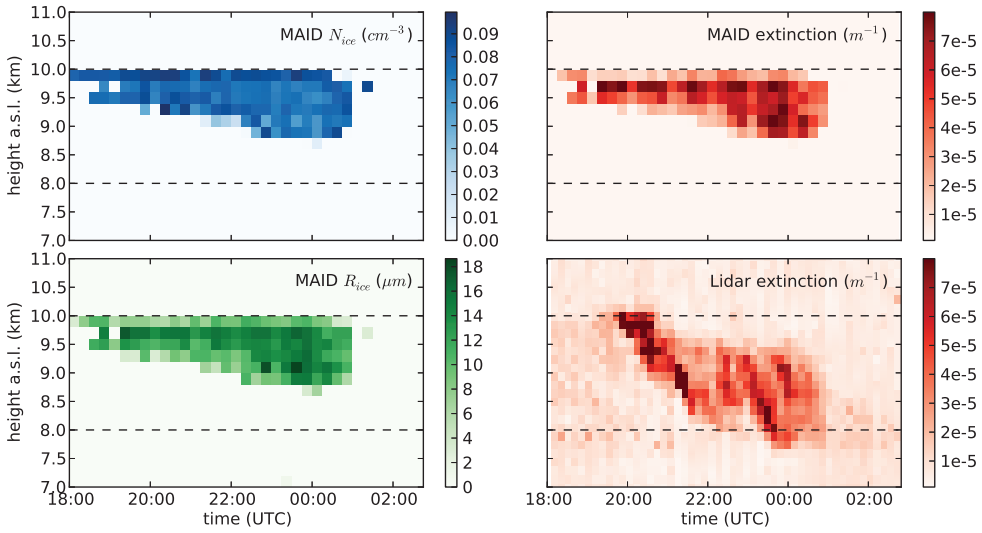

Figure 6.8: Comparison of MAID simulated and observed induced cirrus cloud. Ice number concentration (N_{ice}), mean radius (R_{ice}), calculated extinction of MAID runs are shown as well as lidar-determined extinction.

cloud that can be compared with the lidar observation. The model runs are initialized as follows. The amount of water vapor is set to 100 % of ECMWF in all trajectories in accordance with the results from the sensitivity study. We assume a slight sedimentation of ice crystals (sedimentation factor of 0.9) which is common for all trajectories in the middle of a cirrus cloud. In altitude ranges between 8 and 10 km, the IN properties are set to a concentration of 0.1 cm^{-3} with a low freezing threshold around 105 % rel. humidity with respect to ice. Above and below, a smaller concentration of 0.01 cm^{-3} and a higher freezing threshold around 130 % rel. humidity is assumed to represent the normal IN conditions. These rough assumptions are consistent with the lidar-determined ash profile before cirrus occurrence.

The result is illustrated in Figure 6.8. On the left side, the microphysical properties of ice crystals, number concentration and mean radius are shown. The right side displays the extinction determined from the simulation and lidar observation. A reasonable correspondence between the extinction simulated by MAID and the observed values is found. The occurrence of the simulated cloud is around one hour too early, but the cloud disappeared almost on time at 01:00 UTC. The top height is limited through the IN properties of the trajectories. Thus it fits well at the beginning and overestimates the height after about 21:00 UTC. The cloud base height is overestimated almost all the time. The observed cirrus base height goes down to 8 km while the lower limit of simulated cirrus is around 8.8 km. This is an effect of underlying ECMWF trajectories, which are too dry to contain ice crystals below 8.8 km see Figure 6.2). The ice crystals present would sublimate within a few minutes.

Again the size of the resulting ice crystals is mostly around 10 to 15 µm and this is rather small in comparison to observations of natural cirrus clouds from purely heterogeneous freezing under normal conditions. The number concentration is around 0.07 to 0.09 cm^{-3} and lower than the initialization of 0.1 IN per cm^{-3}. This implies that sedimentation along the trajectory has a significant effect despite the small sizes of the ice crystals. This is due to the long cirrus occurrence of several hours within the trajectories and thus also permitting sufficient time for a slow sedimentation. The standard deviation of resulting ice particle number in the different trajectory realizations is in most cases in the order of 1 to 10 %. This also corroborate the use of only two representation in the case study above. Overall, it is obvious that our simplified model runs provide a reasonable reproduction of the observed cirrus extinction structure. It is shown further that the influence of volcanic ash as IN could be simulated with the box model MAID.

7 Summary and outlook

7.1 Summary

Within the scope of this work, lidar observations of cirrus clouds over Jülich, in the west of Germany, were performed and analyzed, focusing on obtaining a representative cirrus climatology in terms of cirrus thickness, top and base heights, mid temperature, optical thickness and ice water content (IWC). The observed cirrus clouds were evaluated with a temporally averaged extinction profile, corrected for multiple scattering.

143 cirrus observations were analyzed together with additional meteorological data from macrophysical, radiative, and microphysical aspects and assessed to be representative in comparison to other mid-latitude lidar climatologies. Most observed cirrus base heights are around 6 to 10.5 km and top heights around 12 km, implying a frequent cirrus generation due to synoptic weather patterns (e.g. frontal systems). Thus, the cirrus clouds are relatively thick with a vertical extent of about 2.25 km and occur mostly directly below the tropopause. While in summer more cirrus clouds are observed directly below the tropopause, in winter the cirrus top heights are more widely spread in altitude. By comparing the cirrus macrophysical properties to three other mid-latitude lidar climatologies (Sassen and Comstock, 2001; Immler and Schrems, 2002; Goldfarb et al., 2001), rather good agreement is found. For example, the positive cloud mid temperature trend for increasing cirrus thickness (Sassen and Comstock, 2001) is also found in our observations.

The optical depth was used to classify cirrus radiative properties. Mean and median values of optical depth are found to be 0.28 and 0.12 (range: 0.002 - 3), respectively. The distribution of optical depths is in good accordance with the other mid-latitude climatologies (especially the study of Immler and Schrems, 2002). The trend of increasing optical depth with increasing cirrus thickness and cloud mid temperature (Sassen and Comstock, 2001) is also found. The frequency distribution of the IWC derived from the lidar measurements shows two peaks at 0.01 and 6 ppmv, respectively. This bi-modality is in agreement with aircraft in situ measurements and might be attributable to cirrus generation mechanisms at different vertical velocities.

Further comparison of the lidar IWC climatology to the aircraft in situ climatologies of Schiller et al. (2008) and Luebke et al. (2012) answers **question 1** from Section 1.1:

- *Do aircraft in situ water instruments - in particular the hygrometers FISH and CLH - identify thin cirrus clouds?*

  The detectable IWC range of the Leo-Lidar is 0.01 ppmv to 400 ppmv. Higher IWCs cannot be measured with the Leo-Lidar. However, it is particular suitable to detect very thin cirrus clouds. In contrast, the in situ instruments Fish and CLH can measure high IWCs with high accuracy, but for very low values the quality of the measurements becomes increasingly doubtful. Nevertheless, the good agreement of the lowest IWCs around 0.01 ppmv observed by both the Leo-Lidar and the in situ instruments (at least above 225 K) indicates that the very thin cirrus clouds are identified by the in situ instruments.

The results of the climatological measurements as well as the combination of measurements and model simulations allows an answer to **question 2** from Section 1.1:

- *Is it possible to derive cirrus microphysical properties from lidar observations?*

  The vertical profile of cirrus cloud extinction coefficients can be derived from the lidar backscatter signals. The extinction coefficient in turn depends on the cirrus microphysical quantities of ice number concentration and size. A clear relation of these properties to the lidar extinction cannot be established because of the under-determined relation between extinction and microphysical properties. Identical extinction coefficients can be reproduced by an ice particle ensemble composed of either small but many or large but fewer ice crystals. Nevertheless, the IWC, which depends likewise on number and size distribution, can be estimated as a microphysical parameter based on extinction parameterizations. In addition, further detailed knowledge of ice particle properties, including number and size distribution, can be obtained by coupling lidar measurements with microphysical box model simulations as can be seen by the answer to **question 3** from Section 1.1:

- *Does volcanic ash from the Eyjafjallajökull volcano influence cirrus cloud formation?*

  The presence of volcanic ash particles at cirrus altitudes was indicated by lidar measurements outside clouds in April 2010. The IN concentration determined by lidar measurements yields a concentration of effective IN of around 0.1 cm^{-3} at the beginning of cirrus cloud occurrence. This concentration is about 10 times higher than the amount of background IN. The source of potential IN was identified by means of ECWMF trajectories showing air masses originating directly at the volcano. Extensive simulations with the box model MAID show that the observed cirrus cloud was clearly induced by the volcanic ash. In model runs for normal IN conditions no cirrus cloud was formed. Only with the presence of the large amount of highly efficient IN with a low freezing threshold of around 105 % rel. humidity (with respect to ice) can the observations be qualitatively reproduced. The ash-induced

cirrus consists of small but many ice particles with a mean concentration of 0.08 cm^{-3} and a mean radius of 12 µm. This means that the microphysical properties of cirrus clouds can be significantly influenced by a high IN loading. This result already answers the first part of **question 4** from Section 1.1:

- *What is the impact of a high amount of heterogeneous efficient IN and is it of significance for the atmosphere?*

  The difference between the volcanic-ash-induced cirrus (high IN concentration) and a cirrus that would have developed under normal IN concentrations can be seen from the respective model simulations performed for the same air mass trajectories: the number of ice crystals is strongly enhanced from $3 \cdot 10^{-4}$ cm^{-3} to 0.08 cm^{-3}, while the size of the crystals is smaller (12 instead of 30 µm). A whole set of idealized model sensitivity runs covering the major atmospheric temperature and vertical velocity range was performed to further investigate the role of a high IN number for cirrus microphysics. It is shown that for updrafts of up to 20 cm/s a strong positive Twomey effect occurs, generating a higher ice particle concentration than from homogeneous freezing. A negative Twomey effect (fewer ice crystals than from homogeneous freezing) is noticeable for updrafts above 20 cm/s. Fewer homogeneously produced ice particles appear for the higher updrafts, since in the presence of many IN the first heterogeneously formed ice crystals consume part of the water vapor prior to homogeneous freezing. Altogether, cirrus clouds microphysical and thus optical properties are generally affected in an environment polluted by very efficient IN (e.g. volcanic ash).

7.2 Outlook

The lidar-determined cirrus climatology seems to be quite representative of mid-latitudes despite the rather sparse data frequency. However, further lidar measurements are desirable to consolidate the properties of the cirrus climatology. In particular, the inter-comparison of aircraft in situ data and lidar observations could be extended to lower temperatures.

Around 5 % of the cirrus clouds in the lidar climatology occurred above the thermal tropopause. This enables further investigations relating to cirrus cloud occurrence in the lowermost stratosphere (LMS) and would improve the understanding of mixing processes in the UT/LS. The gradient in water vapor at the transition between troposphere and LMS is strongly negative. Even small contributions of moist tropospheric air masses from the tropics due to quasi-horizontal transport into the LMS can increase the water vapor concentration significantly. These enhanced water vapor values could initiate the formation of thin cirrus clouds in the LMS up to polar latitudes. ECMWF data could be used to show the origin of the air masses containing cirrus clouds above the tropopause as implied by the lidar observations. This could be done by using the static stability as a marker for stratospheric and tropospheric air masses (Kunz et al., 2009).

The results and the knowledge gained from the cirrus observations and model-based analysis of ash-induced cirrus cloud form a basis for further model studies concerning natural cirrus clouds. The lidar climatology could be extended by microphysical quantities such as number concentrations and size distributions obtained from MAID model simulations. In particular, the general reliability and reproducibility of lidar-observed natural cirrus clouds based on ECMWF data could be estimated. In addition, this would also make it possible to further investigate the bimodal IWC distribution.

Furthermore, simultaneous cirrus cloud measurements by aircraft and the Leo-Lidar afford the opportunity to validate both measurement techniques. The in situ measurements could be compared to optical cirrus properties observed by the Leo-Lidar. For further improvement of the combined Lidar-MAID approach, model-based microphysical ice particle properties could additionally be compared to in situ measurements.

Bibliography

Ansmann, A.: Molecular-backscatter lidar profiling of the volume-scattering coefficient in cirrus, in Cirrus, edited by D. K. Lynch, K. Sassen, D. O. Starr and G. Stephens, pp. 197-210, Oxford University Press, 2002.

Ansmann, A., Tesche, M., Althausen, D., Mueller, D., Seifert, P., Freudenthaler, V., Heese, B., Wiegner, M., Pisani, G., Knippertz, P., and Dubovik, O.: Influence of Saharan dust on cloud glaciation in southern Morocco during the Saharan Mineral Dust Experiment, Journal of Geophysical Research-atmospheres, 113, D04 210, doi:10.1029/2007JD008785, 2008.

Ansmann, A., Tesche, M., Gross, S., Freudenthaler, V., Seifert, P., Hiebsch, A., Schmidt, J., Wandinger, U., Mattis, I., Muller, D., and Wiegner, M.: The 16 April 2010 major volcanic ash plume over central Europe: EARLINET lidar and AERONET photometer observations at Leipzig and Munich, Germany, Geophysical Research Letters, 37, L13 810, doi:10.1029/2010GL043809, 2010.

Ansmann, A., Tesche, M., Seifert, P., Gross, S., Freudenthaler, V., Apituley, A., Wilson, K. M., Serikov, I., Linne, H., Heinold, B., Hiebsch, A., Schnell, F., Schmidt, J., Mattis, I., Wandinger, U., and Wiegner, M.: Ash and fine-mode particle mass profiles from EARLINET-AERONET observations over central Europe after the eruptions of the Eyjafjallajokull volcano in 2010, Journal of Geophysical Research-atmospheres, 116, D00U02, doi:10.1029/2010JD015567, 2011.

Bailey, M. and Hallett, J.: Nucleation effects on the habit of vapour grown ice crystals from-18 to-42 degrees C, Quarterly Journal of the Royal Meteorological Society, 128, 1461–1483, doi:10.1256/00359000260247318, 2002.

Bailey, M. and Hallett, J.: Growth rates and habits of ice crystals between-20 degrees and-70 degrees C, Journal of the Atmospheric Sciences, 61, 514–544, doi:10.1175/1520-0469(2004)061<0514:GRAHOI>2.0.CO;2, 2004.

Baumgardner, D., Avallone, L., Bansemer, A., Borrmann, S., Brown, P., Bundke, U., Chuang, P. Y., Cziczo, D., Field, P., Gallagher, M., Gayet, J. F., Heymsfield, A., Korolev, A., Kramer, M., McFarquhar, G., Mertes, S., Mohler, O., Lance, S., Lawson, P., Petters, M. D., Pratt, K., Roberts, G., Rogers, D., Stetzer, O., Stith, J., Strapp, W., Twohy, C., and Wendisch,

M.: IN SITU, AIRBORNE INSTRUMENTATION Addressing and Solving Measurement Problems in Ice Clouds, Bulletin of the American Meteorological Society, 93, E529–E534, doi:10.1175/BAMS-D-11-00123.1, 2012.

Bingemer, H., Klein, H., Ebert, M., Haunold, W., Bundke, U., Herrmann, T., Kandler, K., Mueller-Ebert, D., Weinbruch, S., Judt, A., Weber, A., Nillius, B., Ardon-Dryer, K., Levin, Z., and Curtius, J.: Atmospheric ice nuclei in the Eyjafjallajokull volcanic ash plume, Atmospheric Chemistry and Physics, 12, 857–867, doi:10.5194/acp-12-857-2012, 2012.

Bissonnette, L. R.: Multiple-scattering lidar equation, Applied Optics, 35, 6449–6465, doi:10.1364/AO.35.006449, 1996.

Bissonnette, L. R., Roy, G., and Roy, N.: Multiple-scattering-based lidar retrieval: method and results of cloud probings, Applied Optics, 44, 5565–5581, doi:10.1364/AO.44.005565, 2005.

Bohren, C. F. and Huffman, D. R.: Absorption and Scattering of Light by Small Particles, Wiley-VCH, Weinheim, 1. edn., 2004.

Boudala, F. S., Isaac, G. A., Fu, Q., and Cober, S. G.: Parameterization of effective ice particle size for high-latitude clouds, International Journal of Climatology, 22, 1267–1284, doi:10.1002/joc.774, 2002.

Bucholtz, A.: Rayleigh-scattering Calculations For the Terrestrial Atmosphere, Applied Optics, 34, 2765–2773, 1995.

Bunz, H., Benz, S., Gensch, I., and Kraemer, M.: MAID: a model to simulate UT/LS aerosols and ice clouds, Environmental Research Letters, 3, 035 001, doi:10.1088/1748-9326/3/3/035001, 2008.

Cairo, F., Di Donfrancesco, G., Adriani, A., Pulvirenti, L., and Fierli, F.: Comparison of various linear depolarization parameters measured by lidar, Applied Optics, 38, 4425–4432, doi:10.1364/AO.38.004425, 1999.

Cantrell, W. and Heymsfield, A.: Production of ice in tropospheric clouds - A review, Bulletin of the American Meteorological Society, 86, 795–+, doi:10.1175/BAMS-86-6-795, 2005.

Chazette, P., Bocquet, M., Royer, P., Winiarek, V., Raut, J.-C., Labazuy, P., Gouhier, M., Lardier, M., and Cariou, J.-P.: Eyjafjallajkull ash concentrations derived from both lidar and modeling, Journal of Geophysical Research-atmospheres, 117, D00U14, doi:10.1029/2011JD015755, 2012.

Cziczo, D. J., Froyd, K. D., Gallavardin, S. J., Moehler, O., Benz, S., Saathoff, H., and Murphy, D. M.: Deactivation of ice nuclei due to atmospherically relevant surface coatings, Environmental Research Letters, 4, 044 013, doi:10.1088/1748-9326/4/4/044013, 2009.

Dacre, H. F., Grant, A. L. M., Hogan, R. J., Belcher, S. E., Thomson, D. J., Devenish, B. J., Marenco, F., Hort, M. C., Haywood, J. M., Ansmann, A., Mattis, I., and Clarisse, L.: Evaluating the structure and magnitude of the ash plume during the initial phase of the 2010 Eyjafjallajokull eruption using lidar observations and NAME simulations, Journal of Geophysical Research-atmospheres, 116, D00U03, doi:10.1029/2011JD015608, 2011.

Davis, S. M., Avallone, L. M., Weinstock, E. M., Twohy, C. H., Smith, J. B., and Kok, G. L.: Comparisons of in situ measurements of cirrus cloud ice water content, Journal of Geophysical Research-atmospheres, 112, D10 212, doi:10.1029/2006JD008214, 2007.

Dean, S. M., Lawrence, B. N., Grainger, R. G., and Heuff, D. N.: Orographic cloud in a GCM: the missing cirrus, Climate Dynamics, 24, 771–780, doi:10.1007/s00382-005-0020-9, 2005.

DeMott, P. J., Cziczo, D. J., Prenni, A. J., Murphy, D. M., Kreidenweis, S. M., Thomson, D. S., Borys, R., and Rogers, D. C.: Measurements of the concentration and composition of nuclei for cirrus formation, Proceedings of the National Academy of Sciences of the United States of America, 100, 14 655–14 660, doi:10.1073/pnas.2532677100, 2003.

DeMott, P. J., Prenni, A. J., Liu, X., Kreidenweis, S. M., Petters, M. D., Twohy, C. H., Richardson, M. S., Eidhammer, T., and Rogers, D. C.: Predicting global atmospheric ice nuclei distributions and their impacts on climate, Proceedings of the National Academy of Sciences of the United States of America, 107, 11 217–11 222, doi:10.1073/pnas.0910818107, 2010.

Dobbie, S. and Jonas, P.: Radiative influences on the structure and lifetime of cirrus clouds, Quarterly Journal of the Royal Meteorological Society, 127, 2663–2682, doi:10.1256/smsqj.57807, 2001.

Durant, A. J., Shaw, R. A., Rose, W. I., Mi, Y., and Ernst, G. G. J.: Ice nucleation and overseeding of ice in volcanic clouds, Journal of Geophysical Research-atmospheres, 113, D09 206, doi:10.1029/2007JD009064, 2008.

Fernald, F. G.: Analysis of Atmospheric Lidar Observations - Some Comments, Applied Optics, 23, 652–653, 1984.

Fornea, A. P., Brooks, S. D., Dooley, J. B., and Saha, A.: Heterogeneous freezing of ice on atmospheric aerosols containing ash, soot, and soil, Journal of Geophysical Research-atmospheres, 114, D13 201, doi:10.1029/2009JD011958, 2009.

Gary, B. L.: Mesoscale temperature fluctuations in the stratosphere, Atmospheric Chemistry and Physics, 6, 4577–4589, 2006.

Gasteiger, J., Gross, S., Freudenthaler, V., and Wiegner, M.: Volcanic ash from Iceland over Munich: mass concentration retrieved from ground-based remote sensing measurements, Atmospheric Chemistry and Physics, 11, 2209–2223, doi:10.5194/acp-11-2209-2011, 2011.

Gensch, I. V., Bunz, H., Baumgardner, D. G., Christensen, L. E., Fahey, D. W., Herman, R. L., Popp, P. J., Smith, J. B., Troy, R. F., Webster, C. R., Weinstock, E. M., Wilson, J. C., Peter, T., and Kraemer, M.: Supersaturations, microphysics and nitric acid partitioning in a cold cirrus cloud observed during CR-AVE 2006: an observation-modelling intercomparison study, Environmental Research Letters, 3, 035 003, doi:10.1088/1748-9326/3/3/035003, 2008.

Gierens, K.: On the transition between heterogeneous and homogeneous freezing, Atmospheric Chemistry and Physics, 3, 437–446, 2003.

Goldfarb, L., Keckhut, P., Chanin, M. L., and Hauchecorne, A.: Cirrus climatological results front lidar measurements at OHP (44 degrees N, 6 degrees E), Geophysical Research Letters, 28, 1687–1690, doi:10.1029/2000GL012701, 2001.

Gross, S., Freudenthaler, V., Wiegner, M., Gasteiger, J., Geiss, A., and Schnell, F.: Dual-wavelength linear depolarization ratio of volcanic aerosols: Lidar measurements of the Eyjafjallajokull plume over Maisach, Germany, Atmospheric Environment, 48, 85–96, doi:10.1016/j.atmosenv.2011.06.017, 2012.

Gu, Y. and Liou, K. N.: Cirrus cloud horizontal and vertical inhomogeneity effects in a GCM, Meteorology and Atmospheric Physics, 91, 223–235, doi:10.1007/s00703-004-0099-2, 2006.

Guerrero-Rascado, J. L., Costa, M. J., Bortoli, D., Silva, A. M., Lyamani, H., and Alados-Arboledas, L.: Infrared lidar overlap function: an experimental determination, Optics Express, 18, 20 350–20 359, 2010.

Haag, W., Karcher, B., Strom, J., Minikin, A., Lohmann, U., Ovarlez, J., and Stohl, A.: Freezing thresholds and cirrus cloud formation mechanisms inferred from in situ measurements of relative humidity, Atmospheric Chemistry and Physics, 3, 1791–1806, 2003.

Hallett, J., Arnott, W. P., Bailey, M. P., and Hallett, J. T.: Ice crystals in cirrus, in Cirrus, edited by D. K. Lynch, K. Sassen, D. O. Starr and G. Stephens, pp. 41-77, Oxford University Press, 2002.

Heintzenberg, J. and Charlson, R. J.: Clouds in the Perturbed Climate System Their Relationship to Energy Balance, Atmospheric Dynamics, and Precipitation Introduction, doi:10.1109/CLEOE-EQEC.2009.5192754, 2009.

Heymsfield, A. J. and Iaquinta, J.: Cirrus crystal terminal velocities, Journal of the Atmospheric Sciences, 57, 916–938, doi:10.1175/1520-0469(2000)057<0916:CCTV>2.0.CO;2, 2000.

Heymsfield, A. J., Winker, D., and van Zadelhoff, G. J.: Extinction-ice water content-effective radius algorithms for CALIPSO, Geophysical Research Letters, 32, L10 807, doi:10.1029/2005GL022742, 2005.

Hogan, R. J.: Fast Lidar and Radar Multiple-Scattering Models. Part I: Small-Angle Scattering Using the Photon Variance-Covariance Method, Journal of the Atmospheric Sciences, 65, 3621–3635, doi:10.1175/2008JAS2642.1, 2008.

Holton, J. R. and Gettelman, A.: Horizontal transport and the dehydration of the stratosphere, Geophysical Research Letters, 28, 2799–2802, doi:10.1029/2001GL013148, 2001.

Hoyle, C. R., Luo, B. P., and Peter, T.: The origin of high ice crystal number densities in cirrus clouds, Journal of the Atmospheric Sciences, 62, 2568–2579, 2005.

Hoyle, C. R., Pinti, V., Welti, A., Zobrist, B., Marcolli, C., Luo, B., Hoeskuldsson, A., Mattsson, H. B., Stetzer, O., Thorsteinsson, T., Larsen, G., and Peter, T.: Ice nucleation properties of volcanic ash from Eyjafjallajokull, Atmospheric Chemistry and Physics, 11, 9911–9926, doi:10.5194/acp-11-9911-2011, 2011.

Immler, F. and Schrems, O.: LIDAR measurements of cirrus clouds in the northern and southern midlatitudes during INCA (55 degrees N, 53 degrees S): A comparative study, Geophysical Research Letters, 29, 1809, doi:10.1029/2002GL015077, 2002.

Immler, F., Treffeisen, R., Engelbart, D., Kruger, K., and Schrems, O.: Cirrus, contrails, and ice supersaturated regions in high pressure systems at northern mid latitudes, Atmospheric Chemistry and Physics, 8, 1689–1699, 2008.

IPCC: Climate Change 2007: The Physical Science Basis of Climate Change. Contribution of Working Group I to the Fourth Assessment Report of the Intergovernmental Panel on Climate Change, Chambridge University Press, 2007.

Isono, K., Komabayasi, M., and Ono, A.: Volcanoes As A Source of Atmospheric Ice Nuclei, Nature, 183, 317–318, doi:10.1038/183317a0, 1959.

Johnson, B., Turnbull, K., Brown, P., Burgess, R., Dorsey, J., Baran, A. J., Webster, H., Haywood, J., Cotton, R., Ulanowski, Z., Hesse, E., Woolley, A., and Rosenberg, P.: In situ observations of volcanic ash clouds from the FAAM aircraft during the eruption of Eyjafjallajokull in 2010, Journal of Geophysical Research-atmospheres, 117, D00U24, doi:10.1029/2011JD016760, 2012.

Kärcher, B. and Lohmann, U.: A parameterization of cirrus cloud formation: Homogeneous freezing of supercooled aerosols, Journal of Geophysical Research-atmospheres, 107, 4010, doi:10.1029/2001JD000470, 2002.

Kärcher, B. and Lohmann, U.: A parameterization of cirrus cloud formation: Heterogeneous freezing, Journal of Geophysical Research-atmospheres, 108, 4402, doi:10.1029/2002JD003220, 2003.

Kärcher, B. and Spichtinger, P.: Clouds in the Perturbed Climate System Their Relationship to Energy Balance, Atmospheric Dynamics, and Precipitation: Cloud-controlling Factors of Cirrus, 2009.

Karcher, B., Hendricks, J., and Lohmann, U.: Physically based parameterization of cirrus cloud formation for use in global atmospheric models, Journal of Geophysical Research-atmospheres, 111, D01 205, doi:10.1029/2005JD006219, 2006.

Klett, J. D.: Stable Analytical Inversion Solution For Processing Lidar Returns, Applied Optics, 20, 211–220, doi:10.1364/AO.20.000211, 1981.

Klett, J. D.: Lidar Inversion With Variable Backscatter Extinction Ratios, Applied Optics, 24, 1638–1643, 1985.

Kley, D., Russel, J. M., and Phillips, C.: SPARC Assessment of upper tropospheric and stratospheric water vapor, WCRP-113, WMO/TD-No.1043, SPARC Report No. 2, pp. 312, 2000.

Konopka, P., Guenther, G., Mueller, R., dos Santos, F. H. S., Schiller, C., Ravegnani, F., Ulanovsky, A., Schlager, H., Volk, C. M., Viciani, S., Pan, L. L., McKenna, D. . S., and Riese, M.: Contribution of mixing to upward transport across the tropical tropopause layer (TTL), Atmospheric Chemistry and Physics, 7, 3285–3308, 2007.

Koop, T.: Homogeneous ice nucleation in water and aqueous solutions, Zeitschrift Fur Physikalische Chemie-international Journal of Research In Physical Chemistry & Chemical Physics, 218, 1231–1258, doi:10.1524/zpch.218.11.1231.50812, 2004.

Koop, T., Luo, B. P., Tsias, A., and Peter, T.: Water activity as the determinant for homogeneous ice nucleation in aqueous solutions, Nature, 406, 611–614, doi:10.1038/35020537, 2000.

Krämer, M. and Afchine, A.: Sampling characteristics of inlets operated at low U/U-0 ratios: new insights from computational fluid dynamics (CFX) modeling, Journal of Aerosol Science, 35, 683–694, doi:10.1016/j.jaerosci.2003.11.011, 2004.

Krämer, M. and Hildebrandt, M.: The role of heterogeneous freezing in cirrus formation: new model sensitivity studies, AMS Cloud Physics Conference, Portland, USA, 2010.

Krämer, M., Schiller, C., Afchine, A., Bauer, R., Gensch, I., Mangold, A., Schlicht, S., Spelten, N., Sitnikov, N., Borrmann, S., de Reus, M., and Spichtinger, P.: Ice supersaturations and

cirrus cloud crystal numbers RID E-3868-2010, Atmospheric Chemistry and Physics, 9, 3505–3522, 2009.

Kulkarni, G. and Dobbie, S.: Ice nucleation properties of mineral dust particles: determination of onset RHi, IN active fraction, nucleation time-lag, and the effect of active sites on contact angles, Atmospheric Chemistry and Physics, 10, 95–105, 2010.

Kunz, A., Konopka, P., Mueller, R., Pan, L. L., Schiller, C., and Rohrer, F.: High static stability in the mixing layer above the extratropical tropopause, Journal of Geophysical Research-atmospheres, 114, D16 305, doi:10.1029/2009JD011840, 2009.

Langer, G., Garcia, C. J., Mendonca, B. G., Pueschel, R. F., and Fullerto, C.: Hawaiian Volcanos - Source of Ice Nuclei, Journal of Geophysical Research, 79, 873–875, doi:10.1029/JC079i006p00873, 1974.

Luebke, A. E., Avallone, L. M., Schiller, C., Rolf, C., and Kraemer, M.: Ice Water Content of Arctic, Midlatitude, and Tropical Cirrus. Part II: Extension of the Database and New Statistical Analysis, to be submitted, 2012.

Luo, Z. Z., Kley, D., Johnson, R. H., and Smit, H.: Ten years of measurements of tropical upper-tropospheric water vapor by MOZAIC. Part II: Assessing the ECMWF humidity analysis, Journal of Climate, 21, 1449–1466, doi:10.1175/2007JCLI1887.1, 2008.

Lynch, D. K., Sassen, K., Starr, D. O., and Stephens, G.: Cirrus, chapter: Molecular-backscatter lidar profiling of the volume-scattering coefficient in cirrus, in Cirrus, Oxford University Press, 2002.

Mangold, A., Wagner, R., Saathoff, H., Schurath, U., Giesemann, C., Ebert, V., Kramer, M., and Mohler, O.: Experimental investigation of ice nucleation by different types of aerosols in the aerosol chamber AIDA: implications to microphysics of cirrus clouds, Meteorologische Zeitschrift, 14, 485–497, doi:10.1127/0941-2948/2005/0053, 2005.

Mattis, I., Tesche, M., Grein, M., Freudenthaler, V., and Mueller, D.: Systematic error of lidar profiles caused by a polarization-dependent receiver transmission: quantification and error correction scheme, Applied Optics, 48, 2742–2751, 2009.

McKenna, D. S., Konopka, P., Grooss, J. U., Gunther, G., Muller, R., Spang, R., Offermann, D., and Orsolini, Y.: A new Chemical Lagrangian Model of the Stratosphere (CLaMS) - 1. Formulation of advection and mixing, Journal of Geophysical Research-atmospheres, 107, 4309, doi:10.1029/2000JD000114, 2002.

Miloshevich, L. M., Vomel, H., Whiteman, D. N., and Leblanc, T.: Accuracy assessment and correction of Vaisala RS92 radiosonde water vapor measurements, Journal of Geophysical Research-atmospheres, 114, D11 305, doi:10.1029/2008JD011565, 2009.

Moehler, O., Stetzer, O., Schaefers, S., Linke, C., Schnaiter, M., Tiede, R., Saathoff, H., Kramer, M., Mangold, A., Budz, P., Zink, P., Schreiner, J., Mauersberger, K., Haag, W., Karcher, B., and Schurath, U.: Experimental investigation of homogeneous freezing of sulphuric acid particles in the aerosol chamber AIDA, Atmospheric Chemistry and Physics, 3, 211–223, 2003.

Moehler, O., Buttner, S., Linke, C., Schnaiter, M., Saathoff, H., Stetzer, O., Wagner, R., Kramer, M., Mangold, A., Ebert, V., and Schurath, U.: Effect of sulfuric acid coating on heterogeneous ice nucleation by soot aerosol particles, Journal of Geophysical Research-atmospheres, 110, D11 210, doi:10.1029/2004JD005169, 2005.

Moehler, O., Benz, S., Saathoff, H., Schnaiter, M., Wagner, R., Schneider, J., Walter, S., Ebert, V., and Wagner, S.: The effect of organic coating on the heterogeneous ice nucleation efficiency of mineral dust aerosols, Environmental Research Letters, 3, 025 007, doi:10.1088/1748-9326/3/2/025007, 2008.

NOAA, NASA, and USAF: U.S. Standard Atmosphere, 1976, NOAA-S/T 76-1562, Washington, D.C., National Oceanic and atmospheric administration, National Aeronautics and Space Administration, United States Air Force, 1976.

Noel, V. and Chepfer, H.: A global view of horizontally oriented crystals in ice clouds from Cloud-Aerosol Lidar and Infrared Pathfinder Satellite Observation (CALIPSO), Journal of Geophysical Research-atmospheres, 115, D00H23, doi:10.1029/2009JD012365, 2010.

Peter, T., Marcolli, C., Spichtinger, P., Corti, T., Baker, M. B., and Koop, T.: When dry air is too humid, Science, 314, 1399–+, doi:10.1126/science.1135199, 2006.

Platt, C. M. R., Abshire, N. L., and McNice, G. T.: Some Microphysical Properties of An Ice Cloud From Lidar Observation of Horizontally Oriented Crystals, Journal of Applied Meteorology, 17, 1220–1224, doi:10.1175/1520-0450(1978)017<1220:SMPOAI>2.0.CO;2, 1978.

Prenni, A. J., Demott, P. J., Rogers, D. C., Kreidenweis, S. M., Mcfarquhar, G. M., Zhang, G., and Poellot, M. R.: Ice nuclei characteristics from M-PACE and their relation to ice formation in clouds, Tellus Series B-chemical and Physical Meteorology, 61, 436–448, doi:10.1111/j.1600-0889.2009.00415.x, 2009.

Pruppacher, H. and Klett, J.: Microphysics of Clouds and Precipitation, Kluwer Academic Publishers, Dordrecht, 2nd edition, 1997.

Rolf, C., Krämer, M., Schiller, C., Hildebrandt, M., and Riese, M.: Lidar observation and model simulation of a volcanic-ash-induced cirrus cloud during the Eyjafjallajökull eruption, Atmospheric Chemistry and Physics Discussions, 12, 15 675–15 707, doi:10.5194/

acpd-12-15675-2012, URL http://www.atmos-chem-phys-discuss.net/12/15675/2012/, 2012.

Salzmann, M., Ming, Y., Golaz, J. . C., Ginoux, P. A., Morrison, H., Gettelman, A., Kraemer, M., and Donner, L. J.: Two-moment bulk stratiform cloud microphysics in the GFDL AM3 GCM: description, evaluation, and sensitivity tests, Atmospheric Chemistry and Physics, 10, 8037–8064, doi:10.5194/acp-10-8037-2010, 2010.

Sassen, K.: Polarization in lidar, in Lidar: Range-Resolved Optical Remote Sensing of the Atmosphere, edited by C. Weitkamp, pp. 19-42, Springer, 2005.

Sassen, K. and Benson, S.: A midlatitude cirrus cloud climatology from the facility for atmospheric remote sensing. Part II: Microphysical properties derived from lidar depolarization, Journal of the Atmospheric Sciences, 58, 2103–2112, doi:10.1175/1520-0469(2001)058<2103:AMCCCF>2.0.CO;2, 2001.

Sassen, K. and Campbell, J. R.: A midlatitude cirrus cloud climatology from the facility for atmospheric remote sensing. Part I: Macrophysical and synoptic properties, Journal of the Atmospheric Sciences, 58, 481–496, doi:10.1175/1520-0469(2001)058<0481:AMCCCF>2.0.CO;2, 2001.

Sassen, K. and Cho, B. S.: Subvisual Thin Cirrus Lidar Dataset For Satellite Verification and Climatological Research, Journal of Applied Meteorology, 31, 1275–1285, doi:10.1175/1520-0450(1992)031<1275:STCLDF>2.0.CO;2, 1992.

Sassen, K. and Comstock, J. M.: A midlatitude cirrus cloud climatology from the facility for atmospheric remote sensing. Part III: Radiative properties, Journal of the Atmospheric Sciences, 58, 2113–2127, doi:10.1175/1520-0469(2001)058<2113:AMCCCF>2.0.CO;2, 2001.

Sassen, K. and Zhao, H. G.: Lidar Multiple-scattering In Water Droplet Clouds - Toward An Improved Treatment, Optical Review, 2, 394–400, doi:10.1007/s10043-995-0394-2, 1995.

Schiller, C., Kraemer, M., Afchine, A., Spelten, N., and Sitnikov, N.: Ice water content of Arctic, midlatitude, and tropical cirrus, Journal of Geophysical Research-atmospheres, 113, D24 208, doi:10.1029/2008JD010342, 2008.

Schnell, R. C. and Delany, A. C.: Airborne Ice Nuclei Near An Active Volcano, Nature, 264, 535–536, doi:10.1038/264535a0, 1976.

Schotland, R. M., Sassen, K., and Stone, R.: Observations by Lidar of Linear Depolarization Ratios for Hydrometeors, Journal of Applied Meteorology, 10, 1011–1017, doi:10.1175/1520-0450(1971)010<1011:OBLOLD>2.0.CO;2, 1971.

Schroeder, S., Preusse, P., Ern, M., and Riese, M.: Gravity waves resolved in ECMWF and measured by SABER, Geophysical Research Letters, 36, L10 805, doi:10.1029/2008GL037054, 2009.

Schumann, U., Weinzierl, B., Reitebuch, O., Schlager, H., Minikin, A., Forster, C., Baumann, R., Sailer, T., Graf, K., Mannstein, H., Voigt, C., Rahm, S., Simmet, R., Scheibe, M., Lichtenstern, M., Stock, P., Ruba, H., Schauble, D., Tafferner, A., Rautenhaus, M., Gerz, T., Ziereis, H., Krautstrunk, M., Mallaun, C., Gayet, J. F., Lieke, K., Kandler, K., Ebert, M., Weinbruch, S., Stohl, A., Gasteiger, J., Gross, S., Freudenthaler, V., Wiegner, M., Ansmann, A., Tesche, M., Olafsson, H., and Sturm, K.: Airborne observations of the Eyjafjalla volcano ash cloud over Europe during air space closure in April and May 2010, Atmospheric Chemistry and Physics, 11, 2245–2279, doi:10.5194/acp-11-2245-2011, 2011.

Seifert, P.: A statistical analysis based on 11 years of lidar observations of aerosols and clouds over Leipzig, Ph.D. thesis, Faculty for physics and geosciences, University of Leipzig, Germany, 2010.

Seifert, P., Ansmann, A., Mueller, D., Wandinger, U., Althausen, D., Heymsfield, A. J., Massie, S. T., and Schmitt, C.: Cirrus optical properties observed with lidar, radiosonde, and satellite over the tropical Indian Ocean during the aerosol-polluted northeast and clean maritime southwest monsoon, Journal of Geophysical Research-atmospheres, 112, D17 205, doi:10.1029/2006JD008352, 2007.

Seifert, P., Ansmann, A., Gross, S., Freudenthaler, V., Heinold, B., Hiebsch, A., Mattis, I., Schmidt, J., Schnell, F., Tesche, M., Wandinger, U., and Wiegner, M.: Ice formation in ash-influenced clouds after the eruption of the Eyjafjallajokull volcano in April 2010, Journal of Geophysical Research-atmospheres, 116, D00U04, doi:10.1029/2011JD015702, 2011.

She, C. Y.: Spectral structure of laser light scattering revisited: bandwidths of nonresonant scattering lidars, Applied Optics, 40, 4875–4884, doi:10.1364/AO.40.004875, 2001.

Spichtinger, P. and Cziczo, D. J.: Impact of heterogeneous ice nuclei on homogeneous freezing events in cirrus clouds, Journal of Geophysical Research-atmospheres, 115, D14 208, doi: 10.1029/2009JD012168, 2010.

Spichtinger, P. and Gierens, K. M.: Modelling of cirrus clouds - Part 1a: Model description and validation, Atmospheric Chemistry and Physics, 9, 685–706, 2009a.

Spichtinger, P. and Gierens, K. M.: Modelling of cirrus clouds - Part 1b: Structuring cirrus clouds by dynamics, Atmospheric Chemistry and Physics, 9, 707–719, 2009b.

Steinke, I., Moehler, O., Kiselev, A., Niemand, M., Saathoff, H., Schnaiter, M., Skrotzki, J., Hoose, C., and Leisner, T.: Ice nucleation properties of fine ash particles from the

Eyjafjallajokull eruption in April 2010, Atmospheric Chemistry and Physics, 11, 12 945–12 958, doi:10.5194/acp-11-12945-2011, 2011.

Stubenrauch, C. J., Chedin, A., Radel, G., Scott, N. A., and Serrar, S.: Cloud properties and their seasonal and diurnal variability from TOVS path-B, Journal of Climate, 19, 5531–5553, doi:10.1175/JCLI3929.1, 2006.

Thomas, L., Cartwright, J. C., and Wareing, D. P.: Lidar observations of the horizontal orientation of ice crystals in cirrus clouds, Tellus Series B, 42, 211–216, 1990.

Thornton, B. F., Toohey, D. W., Tuck, A. F., Elkins, J. W., Kelly, K. K., Hovde, S. J., Richard, E. C., Rosenlof, K. H., Thompson, T. L., Mahoney, M. J., and Wilson, J. C.: Chlorine activation near the midlatitude tropopause, Journal of Geophysical Research-atmospheres, 112, D18 306, doi:10.1029/2006JD007640, 2007.

Twomey, S.: Pollution and Planetary Albedo, Atmospheric Environment, 8, 1251–1256, doi:10.1016/0004-6981(74)90004-3, 1974.

Vömel, H., Selkirk, H., Miloshevich, L., Valverde-Canossa, J., Valdes, J., Kyro, E., Kivi, R., Stolz, W., Peng, G., and Diaz, J. A.: Radiation dry bias of the vaisala RS92 humidity sensor, Journal of Atmospheric and Oceanic Technology, 24, 953–963, doi:10.1175/JTECH2019.1, 2007.

Wandinger, U.: Multiple-scattering influence on extinction- and backscatter-coefficient measurements with Raman and high-spectral-resolution lidars, Applied Optics, 37, 417–427, 1998.

Wandinger, U.: Introduction to lidar, in Lidar: Range-Resolved Optical Remote Sensing of the Atmosphere, edited by C. Weitkamp, pp. 1-18, Springer, 2005.

Westbrook, C. D., Illingworth, A. J., O'Connor, E. J., and Hogan, R. J.: Doppler lidar measurements of oriented planar ice crystals falling from supercooled and glaciated layer clouds, Quarterly Journal of the Royal Meteorological Society, 136, 260–276, doi:10.1002/qj.528, 2010.

Young, A. T.: Rayleigh-scattering, Applied Optics, 20, 533–535, doi:10.1364/AO.20.000533, 1981.

Young, A. T.: Rayleigh-scattering, Physics Today, 35, 42–48, doi:10.1063/1.2890003, 1982.

Zöger, M., Afchine, A., Eicke, N., Gerhards, M. T., Klein, E., McKenna, D. S., Morschel, U., Schmidt, U., Tan, V., Tuitjer, F., Woyke, T., and Schiller, C.: Fast in situ stratospheric hygrometers: A new family of balloon-borne and airborne Lyman alpha photofragment fluorescence hygrometers, Journal of Geophysical Research-atmospheres, 104, 1807–1816, doi:10.1029/1998JD100025, 1999.

A Lidar Appendix

A.1 Light scattering processes in the atmosphere

Light in the atmosphere is scattered and absorbed by air molecules and aerosol as well as cloud particles. The scattering process related to molecules is mentioned as molecular scattering and on particles as particular scattering, as long as the size of the scatterer is in the same order as the wavelength λ of the involved light. The interaction between objects which are much larger than the wavelength of the light can be described with geometrical optics (not further mentioned here). The cross sections for particular and molecular scattering depends on the wavelength and optical properties as well as the sizes of the scatterer. In addition, the polarization of the light can be changed by the scattering process. Therefore, the knowledge of the basic terms and definitions of light scattering is important for the understanding of the lidar technique. A brief overview, mostly specific for the wavelength of 355 nm used by the lidar instrument in this study, is given in the following.

Basic terms and definitions of light scattering

The electric field vector $\vec{\mathrm{E}}$ of a quasi monochromatic electromagnetic wave with the frequency ν, the wave vector $\vec{\mathrm{k}}$ at time t and point $\vec{\mathrm{r}}$ is described as

$$\vec{E}(t) = \left(E_{\parallel}\ \hat{e}_{\parallel} + E_{\perp}\ \hat{e}_{\perp}\right) exp\left(i(\vec{k}\ \vec{r} - 2\pi\ \nu t)\right). \tag{A.1}$$

The oscillation of the electric field vector is always perpendicular to the direction of propagation and thus a transverse wave. But, the development of the oscillation orientation can have several pattern and is called the polarization. If the vector oscillates in a fixed plane, the wave is called linearly polarized and is mostly used in the lidar measurement technique. Light is called circularly polarized, when the vector oscillate with a constant angular speed and a constant amplitude. In that case, the electric vector maps a circle on the propagation plane. If the absolute value of the amplitude varies with the time, the polarization is called elliptic due to the elliptic pattern on the propagation plane. A polarized electromagnetic wave can be described by the superposition of two linearly polarized components parallel ($\parallel$) and perpendicular ($\perp$) (see Eq. A.1). The wave and its polarization state can be expressed by four quantities, the amplitudes of $\mathrm{E}^{\parallel}$ and $\mathrm{E}^{\perp}$, and the phase differences between both components.

All four elements are combined in a so called Stokes parameter $\tilde{\mathrm{P}} = (\mathrm{P}_1,\mathrm{P}_2,\mathrm{P}_3,\mathrm{P}_4)$, explicitly represented after Bohren and Huffman (2004):

$$P_1 = \langle E_\parallel E_\parallel^* + E_\perp E_\perp^* \rangle \tag{A.2}$$

$$P_2 = \langle E_\parallel E_\parallel^* - E_\perp E_\perp^* \rangle \tag{A.3}$$

$$P_3 = \langle E_\parallel E_\perp^* + E_\perp E_\parallel^* \rangle \tag{A.4}$$

$$P_4 = i\langle E_\parallel E_\perp^* - E_\perp E_\parallel^* \rangle. \tag{A.5}$$

The arrow brackets represents the temporal average over an observation period which is much larger than the oscillation period of the wave ($\mathrm{T} \gg 1/\nu$). The *-operator produces the complex conjugated of E. P_1 is proportional to the total intensity of the electromagnetic wave, P_2 is proportional to the intensity of the parallel (0°) or perpendicular (90°) polarized amount and P_3 is proportional to (45°) or (135°), respectively. P_4 represents the intensity of the circular polarized light. In practice, a scatter object (molecule or particle) has scattering planes in any arbitrary orientation. For lidar measurements the scattering plane parallel to the laser polarization is chosen as reference orientation. The degree of polarization is given by

$$p = \frac{\sqrt{(P_2)^2 + (P_3)^2 + (P_4)^2}}{P_1}. \tag{A.6}$$

Completely parallel or perpendicular polarized light has a polarization degree of one. If only linearly polarized light is used ($\mathrm{P}_3 = \mathrm{P}_4 = 0$), which is typical for a lidar system, the polarization degree or linear depolarization (Bohren and Huffman, 2004) is described as

$$\delta = \frac{P_1 - P_2}{P_1 + P_2} = \frac{1-p}{1+p}. \tag{A.7}$$

In the atmosphere, where different scattering partners (molecules or particles) in the measurement volume exists, the linear depolarization δ can not be addressed to one particle with one geometry. Here, δ is a mean depolarization of many scattering partners, named volume depolarization (δ_{vol}).

The scattering process of an incident electromagnetic wave $\vec{\mathrm{P}}^{\mathrm{i}}$ can be represented by a linear equation with the help of a scattering or transformation matrix F also known as Mueller matrix. Thus, the transmitted Stokes vector results in $\vec{\mathrm{P}}^{\mathrm{t}} = \mathrm{F} \cdot \vec{\mathrm{P}}^{\mathrm{i}}$. Each scattering process by molecules and particles in the atmosphere as well as transmission through optical components or reflections on surfaces can be described by such a matrix F.

Aerosol and cloud particles or air molecules are placed in a beam of electromagnetic radiation. A detector measures the intensity I of the transmitted radiation. If all particles and molecules

are removed, the detector measures the emitted intensity I_0, where $I_0 > I$. Therefore the molecules and particles attenuate the intensity ($I_0 - I$) received by the detector due to scattering and absorption. This is called the extinction of the incident beam. The extinction depends on concentration, shape, size, orientation, and chemical composition of particles and molecules as well as the wavelength of the incident radiation. The extinction characterize the exponent in the well known Lambert-Beer's law, which describes the attenuation of radiation passing a certain medium. The extinction can be slit up into a molecular extinction introduced in Section A.1.1 and extinction resulting from absorption and scattering by particles (see Section A.1.2 and 4.3). In contrast to the extinction the backscatter coefficient describes the faculty of a certain medium to scatter radiation back into the incident direction. Extinction and backscatter coefficient are coupled and constitute crucial quantities relating to lidar measurements.

A.1.1 Molecular scattering

The interaction between electromagnetic radiation and molecules with radius much smaller than the wavelength is called molecular scattering. It can be divided into the Rayleigh scattering and the vibrational Raman scattering (Young, 1981, 1982; She, 2001). The latter describes the excitation of the molecule to vibrational oscillations of charge carrier and emission of a photon with a smaller or larger wavelength than the incoming radiation. Thus the vibrational Raman scattering is an inelastic scattering process. The Rayleigh spectrum consists of the central Cabannes line and is as well as the vibrational Raman lines surrounded by the rotational Raman lines. The Cabannes line is the elastic part of the Rayleigh spectrum with no change in wavelength and represent the most probable scattering process. The distance between the Cabannes line and the vibrational Raman lines on the wavelength scale is molecule dependent and for nitrogen for instance 32 nm. The distance between the Cabannes line and the rotational Raman lines is much smaller and typical around 2 nm for nitrogen. But is has to keep in mind that only molecules with an anisotropy of charge carriers like nitrogen or oxygen can produce Raman scattering.

The vibrational Raman lines are not considered further because this lines are only used for Raman lidars and not for aerosol lidars used in this study. Therefore only the interaction due to Rayleigh scattering is described below. The scattering cross section describes the probability for occurrence of a Rayleigh scattering process. These cross section σ represent a surface (in m^2) at which the electromagnetic wave can interact with. Whereas the differential cross section $\partial\sigma/\partial\Omega$ describes the angle distribution of scattered photons dependent on the scattering angle θ. Thus the unit is measured in $m^2 sr^{-1}$. The scattering phase function represents the intensity distribution of a scattering process dependent on the scattering angle θ. In Figure A.1 a) the Rayleigh scattering phase function for an incident wave $\vec{E}$ with one spherical molecule in the center is shown. While the component perpendicular to the paper plane $I_\perp$ is isotropic, the component which is parallel to the incident polarized light ($I_\parallel \propto \cos^2\theta$) represent the resulting

emission characteristic of a Rayleigh scattering process with the typical forward and backward scattering lobes. This is also typical for polarized laser photons. The sum of both represents the Rayleigh scattering of unpolarized incident light (e.g. sun light). The scattering phase function is normally rotationally symmetric.

If an electromagnetic wave scatters at a molecule with the polarizability of charge carriers (like N_2 or O_2), a dipole moment is induced. The induced dipole moments and their oscillation causes a change in the angle dependent Rayleigh cross sections and depolarization of molecules. This behavior is expressed by the relative anisotropy of the regarded molecules, whereas the knowledge of this quantity is necessary for the explicit calculation of Rayleigh cross sections or the molecular depolarization (She, 2001). A relative anisotropy of $\varepsilon = 0.238$ at a wavelength of 355 nm for a normal atmospheric molecular composition is used from a study of Bucholtz (1995). In general the Rayleigh scattering cross section for a scattering angle of 180° or respective backscatter cross section (typical for lidar measurements) can be written as

$$\frac{\partial \sigma_{ray}}{\partial \Omega}(\theta = 180°) = \frac{\pi^2 (n(\lambda) - 1)^2}{N_M^2 \lambda^4} \left(1 + \frac{7\varepsilon}{180}\right) \tag{A.8}$$

with the wavelength (λ) dependent refractive index n(λ), and the molecular particle density N_M (Young, 1981). The proportionality dependence of the reciprocal wavelength to the order of four is typical for the Rayleigh scattering and approximate to $\lambda^{-4.08}$ in the visible spectral range (Young, 1982). This equation considers only the Cabannes line of the Rayleigh scattering which depends strongly on the detection system and the used filters of the lidar instrument. For a full width half maximum (FWHM) of the interference filter between 0.2 and 1.0 nm only the Cabannes line contribute to the detected Rayleigh scattering. The backscatter lidar system used in this study has a interference filter with a FWHM of 0.5 nm (see table A.1). Thus only the impact of the Cabannes line is considered here. The anisotropy correction factor is therefore $1 + 7\varepsilon/180$ instead of $1 + 7\varepsilon/45$ for a wider spectrum including the rotational Raman lines. This results in a value of the backscatter cross section at a wavelength of 355 nm of $\frac{\partial \sigma_{\mathrm{ray}}}{\partial \Omega} = 3.159 \cdot 10^{-31}\ \mathrm{m^2 sr^{-1}}$. The Rayleigh cross section for 180° (Eq. A.8) gets into the total Rayleigh cross section by integration over the whole solid angle, which is proportional to an extinction cross section:

$$\sigma_{ray} = \frac{8\pi}{3} \frac{\pi^2 (n(\lambda) - 1)^2}{N_M^2 \lambda^4} \left(1 + \frac{2\varepsilon}{9}\right). \tag{A.9}$$

The total cross section at a wavelength of 355 nm is $\sigma_{\mathrm{ray}} = 2.761 \cdot 10^{-30}\ \mathrm{m^2}$. The Rayleigh scattering ratio L_{ray} can now be introduced.

This quantity is the ratio of the extinction to the backscatter coefficient of the Rayleigh scattering and is constant for one wavelength and the molecular composition of the atmosphere:

$$L_{ray} = \frac{\sigma_{ray}}{\partial\sigma_{ray}^{180^\circ}/\partial\Omega} = \frac{8\pi}{3} \cdot \left(\frac{180 + 40\varepsilon}{180 + 7\varepsilon}\right) \approx 8.739 \text{ sr}. \tag{A.10}$$

The multiplication of the Rayleigh backscatter and total cross section with the molecular particle density at range r to the ground yield in the molecular backscatter and extinction coefficient (see Eq. A.11 and A.12). The values for backscatter and extinction are derived for the standard ground conditions with a pressure of 1013.25 hPa and temperature of 288.15 K.

$$\alpha_{ray}(r) = N_M(r) \cdot \sigma_{ray}, \qquad \alpha_{ray}^S \approx 7.033 \cdot 10^{-5} \text{ m}^{-1}, \tag{A.11}$$

$$\beta_{ray}(r) = N_M(r) \cdot \frac{\partial\sigma_{ray}}{\partial\Omega}(\theta = 180^\circ), \qquad \beta_{ray}^S \approx 8.046 \cdot 10^{-6} \text{ sr}^{-1}\text{m}^{-1}. \tag{A.12}$$

The molecular number density has to be known to derive the Rayleigh coefficient for every location in the atmosphere. This can easily done with the ideal gas law, Equation A.11 and the knowledge of temperature T and pressure P at the desired location by applying:

$$\beta_{ray} = \beta_{ray}^S \cdot \frac{N_M}{N_M^S} = \beta_{ray}^S \cdot \frac{P}{P^S}\frac{T^S}{T}. \tag{A.13}$$

Whereas $\mathrm{T^S}$, $\mathrm{P^S}$, and β^S are the values for standard atmospheric conditions as also used in Equation A.11 and A.12. The same equation can used for determination of Rayleigh extinction coefficient by replacing β_ray with α_ray. Both values, the backscatter and extinction coefficient, are important for the analysis of lidar data and has to be known as accurate as possible to reduce the error in particle backscatter and extinction calculation described in chapter 4.3.

The depolarization of molecular scattering is important for depolarization measurements either and is already introduced above. Through the anisotropy of the atmospheric gas molecules the polarization of an incident polarized wave changes and depolarization is not zero. The rotational Raman scattering contribute particularly to the molecular depolarization, whereas the depolarization of the Cabannes line only is very week and equal to (Young, 1981):

$$\delta_{ray} = \frac{3\varepsilon}{4\varepsilon + 180} \approx 0.00395. \tag{A.14}$$

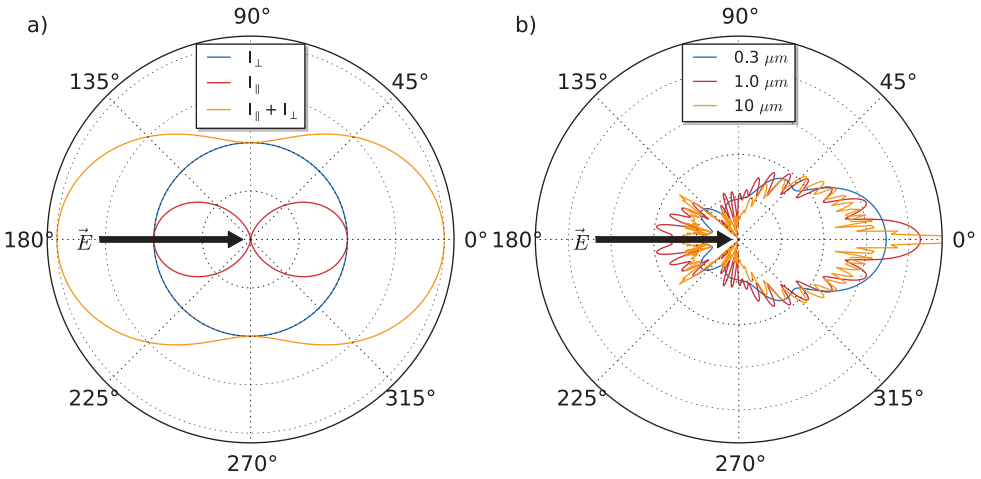

Figure A.1: Scattering phase functions depending on scattering angle θ for an incoming electromagnetic wave with 355 nm wavelength. a) Rayleigh scattering of light by air molecules for the perpendicular polarized component, the parallel component and the sum of both, b) Mie scattering of light by spherical particles with different radii: 0.3, 1.0, and 10 µm.

A.1.2 Particular scattering

Scattering of electromagnetic waves at objects with size similar to the wavelength is called particular scattering. The analytical calculation of the cross section and phase function is considerably more difficult than in the molecular case and is only solvable for particular particle shapes. The most common solution is for a homogeneous sphere with arbitrary size and refractive index given by the Mie formalism. The Mie theory is a complete analytical solution of Maxwell's equations for scattering of electromagnetic radiation by spherical particles Bohren and Huffman (2004). The electromagnetic field inside of the spherical particle is described by normal spherical wave function, which solution are Bessel functions. By using boundary conditions at the spheres surface the scattered radiation at each spatial point outside of the spherical particle can be calculated. The solution of the Mie theory can be approximated by Rayleigh scattering for small objects with size $< 0.2 \cdot \lambda$. Panel b) of Figure A.1 shows the scattering phase functions of spherical particles with different size calculated with the Mie formalism. If the size of the particle is in the order of wavelength (0.3 nm, blue line) the scattering phase function approach to the Rayleigh phase function shown in the left panel of Figure A.1. With increasing size forward scattering becomes more dominant as visible for the particle size of 10 µm (orange line). This size depended behavior has to be considered by interpreting lidar observations of cirrus clouds as explained in Section 4.4.3.

There exists extensions of the Mie formalism which express the solution in terms of infinite series for more complex shapes such as coated spheres, multispheres, spheroids, and infinite

cylinders. With the T-matrix method is it possible to get a solution of the scattering problem for rotational symmetric particle shapes, but this implies a high numerical effort. The technique is also known as null field method and extended boundary technique method (EBCM). Matrix elements are obtained by matching boundary conditions for solutions of Maxwell equations similar to the Mie theory. The resulting T (for transition) matrix describes the linear transformation of coefficients resulting from the boundary conditions of the incident and the scattered field. For spherical particles the T Matrix is diagonal and approaches to the Mie solution.

In general extinction and backscatter coefficient can be derived likewise from these formalisms for one single particle. By considering a particle ensemble the results for one single particle has to be adjusted by the size distribution and the orientation distribution. Normally randomly oriented particles are assumed in case of ice particles. However, one has to know the exact shape and refractive indices of the involved particles for any calculation of scattering properties.

A.2 Explicit calculation of errors in particle backscatter coefficient

The Fernald/Kett inversion of lidar profiles provide the solution for the aerosol backscatter coefficient (Equation 4.6) in the range r_i from the lidar:

$$\beta_{aer}(r_i) = \frac{A(r_i)}{N(r_i)} - \beta_{ray}(r_i)$$

with

$$N(r_i) = B \; - \; 2 \; L_{aer} \int_{r_{ref}}^{r_i} A(\tilde{r}) \, \mathrm{d}\tilde{r}, \qquad B = \frac{P(r_{ref})}{\beta_{aer}(r_{ref}) + \beta_{ray}(r_{ref})},$$

$$A(r_i) = P(r_i) \; e^{-2 \; (L_{aer} - Lray) \; \int_{r_{ref}}^{r_i} \beta_{ray}(\tilde{r}) \, \mathrm{d}\tilde{r}}.$$

Here, only the error calculation below the reference height ($i < r_{ref}$) is presented. For error calculation above r_{ref} it is necessary to interchange the boundaries of the integration in all equations. For a realization in a computer algorithm the integrals have to converted into sums. The knowledge of the three following therms is required for the error determination in the backscatter coefficient $\beta_{aer}(r_i)$:

(a) $\frac{\partial \beta_{aer}(r_i)}{\partial P(r_j)}$, (b) $\frac{\partial \beta_{aer}(r_i)}{\partial \beta_{ray}(r_j)}$ and (c) $\frac{\partial \beta_{aer}(r_i)}{\partial L_{aer}}$.

To simplify the equations we denote the quantities with indices and introduce two case differentiations:

$$\begin{aligned} A_i &= A(r_i) \\ N_i &= N(r_i) \\ P_i &= P(r_i) \\ \beta_i^{ray} &= \beta_{ray}(r_i) \\ \beta_i^{aer} &= \beta_{aer}(r_i). \end{aligned}$$

$$\varepsilon_{ij} = \begin{cases} 1 & : \quad j \geq i \\ 0 & : \quad j < i \end{cases}$$

$$\delta_{ij} = \begin{cases} 1 & : \quad j = i \\ 0 & : \quad j \neq i \end{cases}$$

The difference quotients can be determined by normal Gaussian error propagation by assuming an error on the backscatter signal P, the Rayleigh backscatter coefficient, and the lidar ratio. The explicit representation are:
a) the error caused by the uncertainties of the measured backscatter signal P :

$$\begin{aligned}
\frac{\partial \beta_i^{aer}}{\partial P_j} &= \frac{N_i \; A_i \; \delta_{ij} \; / \; P_j + 2 \; L_{aer} \; A_i \; A_j \; \varepsilon_{ij} \; / \; P_j}{N_i^2} && \text{if } i < r_{ref}, j < r_{ref} \\
\frac{\partial \beta_i^{aer}}{\partial P_j} &= \frac{-\; A_i \; / \; (\beta_{r_{ref}}^{aer} + \beta_{r_{ref}}^{ray}) - 2 \; L_{aer} \; A_i \; A_j \; / \; P_j}{N_i^2} && \text{if } i < r_{ref}, j = r_{ref} \\
\frac{\partial \beta_i^{aer}}{\partial P_j} &= 0 && \text{otherwise.}
\end{aligned}$$

b) the error caused by the uncertainties of the assumption of β_{ray} :

$$\frac{\partial \beta_i^{aer}}{\partial \beta_j^{ray}} = \frac{-2 \; (L_{aer} - L_{ray}) \; N_i \; A_i \; \varepsilon_{ij} - 4 \; L_{aer} \; (L_{aer} - L_{ray}) \; A_i \int_j^i A_{\tilde{r}} \, \mathrm{d}\tilde{r}}{N_i^2} - \delta_{ij}$$

if $i < r_{ref}, j < r_{ref}$

$$\frac{\partial \beta_i^{aer}}{\partial \beta_j^{ray}} = \frac{-2 \; (L_{aer} - L_{ray}) \; N_i \; A_i - A_i \left(-(\beta_{r_{ref}}^{aer} + \beta_{r_{ref}}^{ray})^{-1} \; B + 4 \; L_{aer} \; (L_{aer} - L_{ray}) \; \int_{r_{ref}}^i A_{\tilde{r}} \, \mathrm{d}\tilde{r}) \right)}{N_i^2}$$

if $i \leq r_{ref}, j = r_{ref}$

c) the error caused by the uncertainties of the assumption of L_{aer} :

$$\frac{\partial \beta_i^{aer}}{\partial L_{aer}} = \frac{-2 \; N_i \; A_i \int_{r_{ref}}^i \beta_{\tilde{r}}^{ray} \, \mathrm{d}\tilde{r} + 2 \; A_i \; (\int_{r_{ref}}^i A_{\tilde{r}} \, \mathrm{d}\tilde{r} - 2 \; L_{aer} \int_{r_{ref}}^i A_{\tilde{r}} \int_{r_{ref}}^i \beta_{\xi}^{ray} \mathrm{d}\xi \, \mathrm{d}\tilde{r})}{N_i^2} \; \delta_{ij}.$$

A.3 Transmission ratio

In this section the experimental determination of the transmission ratios, performed at the IfT (Institut für Troposphärenforschung) Leipzig, is described. The same experimental setup is used as described by Mattis et al. (2009) and is only roughly described here. The lidar head was build up horizontally on an optical table. A motorized rotate-able polarizer is placed in front of the telescope window of the lidar head. This polarizer let pass only linear polarized light with a specified polarization direction. The calibration measurements are performed with a halogen-deuterium lamp, witch is connected to the polarizer via a glass fiber. This lamp has a broadband spectrum from 200 to 1100 nm, with a very stable intensity. To determine the transmission ratios the angle position of the polarizer is varied from the signal minimum of parallel channel (P_h) to the maximum visible in Figure A.2. While the parallel channel has a minimum at a certain position of the polarizer, the perpendicular channel has a maximum in the same position. The lidar was measuring in the photon counting mode averaged over three minutes in each polarizer angle position. Around the minimum and maximum positions the average count rate of both channels is measured with an angle resolution of 0.5° and the rest with 10°. Both data series are fitted with a sine squared curve with the amplitude A_i, offset B_i, phase shift x_i, and width w_i depending on the rotation angle φ, whereas the fit looks like:

$$P_i = A_i \cdot sin\left(\frac{\varphi - x_i}{w_i}\right)^2 + B_i. \tag{A.15}$$

The transmission ratios D_i can be derived from the ratio of the darkcount-corrected signals at the perpendicular to parallel aligned position of the polarizer (see Eq. A.16). These positions can be identified by the minimum and maximum in the signal or the amplitude A_i and offset B_i of the fitting function, respectively. In Figure A.2 these fit function are shown either.

$$D_i = \frac{P_i^{\perp}}{P_i^{\parallel}} \qquad \text{results in} \qquad D_h = \frac{B_h}{A_h + B_h}, \qquad D_v = \frac{A_v + B_v}{B_v}. \tag{A.16}$$

Both transmission ratios are calculated after Equation A.16 from the fitting function and yielding for the parallel detector $D_h = 5.0 \cdot 10^{-4} \pm 0.1 \cdot 10^{-4}$ and for the perpendicular detector $D_v = 571.8 \pm 7.9$. This means that for the parallel detector every 2000th detected photon is actual perpendicular polarized and for the perpendicular detector about every 570 detected photon is parallel polarized. While the volume depolarization of a cirrus cloud assuming a ideal detection system yielding a value of 20 %, the true volume depolarization results in 29 % in case of the non-ideal detection system. This large difference between both depolarizations shows the importance of the transmission ratio characterization. All used depolarization values in this study are derived with this measured transmission ratios.

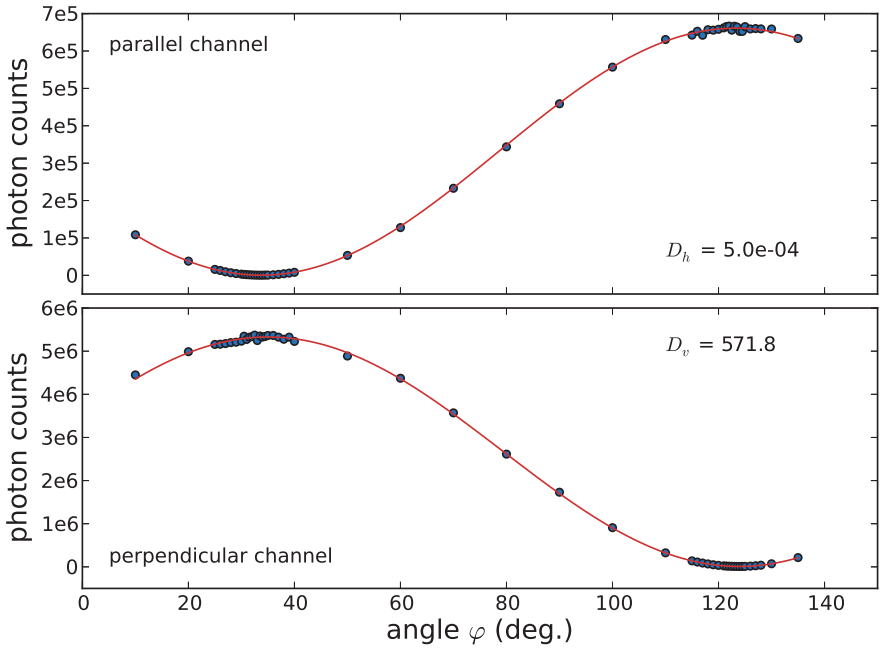

Figure A.2: Averaged photon counts of each detection channel against appointed polarizer angles. The red lines represents sine squared fits.

A.4 Overlap function

The use of the lidar data below the full overlap between the laser and FOV requires the knowledge of the overlap function O(r) (see lidar equation 4.1). The overlap region is defined from the altitude where the laser penetrate the FOV the first time and reach to the altitude where the laser foot print is full visible in the FOV (full overlap). Figure A.3 illustrates the overlap region between the laser and FOV depending on the distance to the laser center by the use of the divergence values from Table A.1.

If the exact geometry of laser and telescope is not known, the overlap function can be estimated by horizontal measurement, as described by Guerrero-Rascado et al. (2010). This means that the lidar head is oriented horizontally to the ground. The lidar measure the same backscatter and extinction coefficients values along the laser path at least the first kilometers range by assuming a homogeneous atmosphere at ground levels. Thus the lidar equation depends only on the overlap function, the decrease of range squared, and the transmission $\mathrm{T(r)} = \exp\{-\int\sigma(\mathrm{r})\mathrm{dr}\}$ (integral over a constant extinction coefficient) and can be denoted as:

$$P(r) = P_0 \, \frac{O(r)}{r^2} \, E \, \beta \, T(r)^2. \tag{A.17}$$

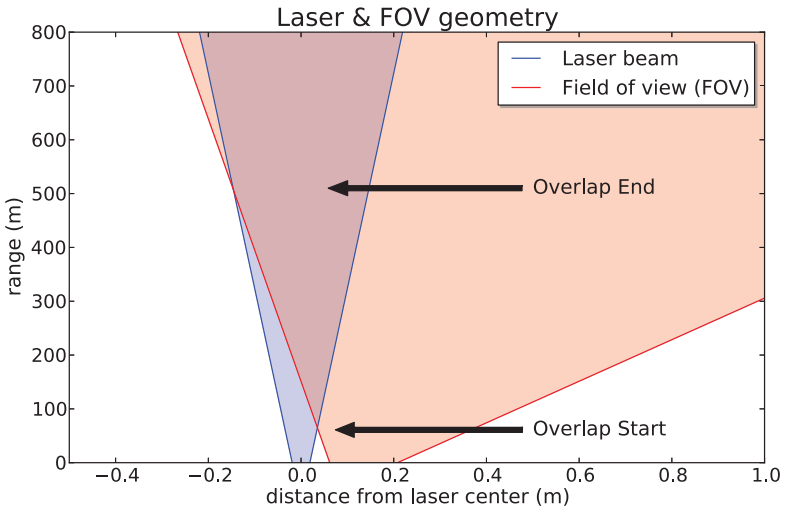

Figure A.3: Overlap between the laser (blue shaded area) and the field of view (FOV, red shaded area) depending on the distance to laser laser center and the measurement range.

This equation can be rearranged to get the overlap function O(r) with the assumption of a constant backscatter and extinction coefficient in the first 1500 m along the laser path:

$$O(r) = \frac{P(r)\ r^2}{K\ \beta\ T(r)^2}. \tag{A.18}$$

The constant K contains all range independent variables like emitted laser power and system efficiency E. This unknown constant parameter can be eliminated by normalizing the overlap function to one, which is even the definition of the overlap function with values from zero to one. The overlap measurement is performed on the roof of the IfT building in Leipzig. During the measurement it was really windy and therefore the atmosphere was well mixed. This reinforced the assumption of a particle homogeneous atmosphere in the height of 25 m (approximately the roof height) along a path of 1500 m horizontally to the ground. From temperature and pressure measurements, also installed on the roof, the Rayleigh backscatter and extinction coefficient can be estimated very accurate. The unknown particle extinction coefficient can be provided by DOAS (Differential Optical Absorption Spectroscopy) measurements with the instrument SAEMS installed on the roof of the IfT building likewise. These measurements reveal a particle extinction coefficient of $1.4 \cdot 10^{-4}$ m^{-1}. The transmission T(r) in range r can then be specified by this extinction value and the overlap function can derived from the measured total backscatter signal and Equation A.18.

The range corrected signal (30 min average) of both channels up to 600 m is displayed in Figure A.4 on the left side. The derived overlap function up to 1500 m is shown on the right

side. The overlap function has a typical s shape with starting at zero, increases rapidly with progressive overlap, and stays constant at one for a complete overlap. These measured overlap function is fitted with the best fit function found in a study of Guerrero-Rascado et al. (2010) to get a functional dependence. From these fit function the start and the end of the overlap function can be estimated by reaching a value of 0.002 and 0.998, respectively. This results in an overlap range starting from 52 m to reach full overlap at 510 m, marked in the left panel of Figure A.4. The full overlap range coincides not with the backscatter signal maximum, because of increasing overlap function and decreasing transmission acting against each other differently. The measured signals can be corrected with the overlap fit function in order that the Klett inversion can be applied to the minimum level of 52 m instead of 510 m.

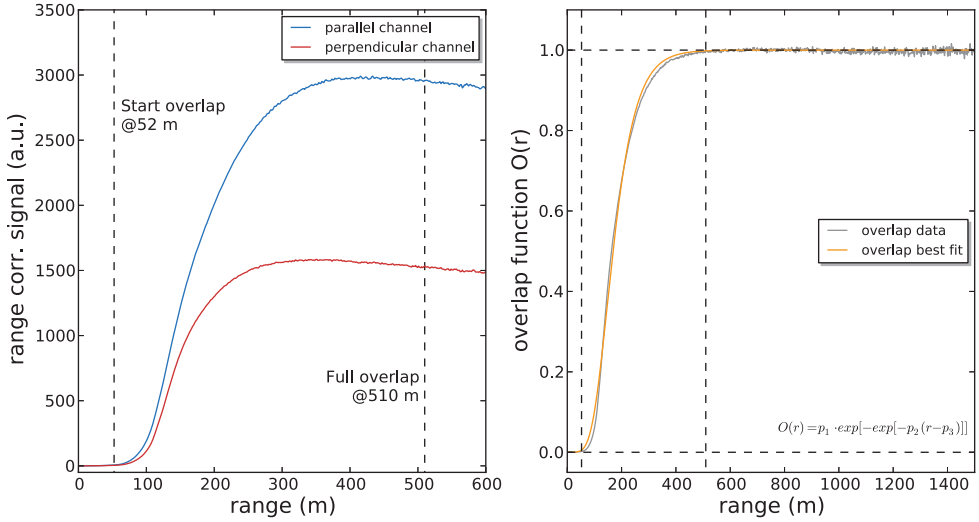

Figure A.4: Measured overlap function between laser and FOV from horizontal measurements. a) Range corrected data averaged over 30 min, b) overlap function from data and fit.

A.5 Specifications of Leosphere ALS 450

Table A.1: Specifications of Leosphere ALS 450.

Performance	
Range:	500 m to 15 km ;(best including overlap: 150 m to 20 km)
Temporal Resolution:	30 s (day) to 3000 s (night)
Vertical Resolution:	60 m (day) and 15 m (night); (best 1.5 m)
Electrical	
Power Supply:	100 - 240 V AC / 50 – 60 Hz
Power Consumption:	max. 550 W
Environmental	
Temperature range:	-20 - 40 °C (various casing)
Operating Humidity:	0 – 100 %
Casing Certification:	Three levels: IP40 to IP65
Weight / Dimensions (Basic Casing)	
Optical Head:	15 kg / 650 x 365 x 190 mm
Electronics:	100 kg / 700 x 600 x 600 mm
Optics, Electrical and Mechanics	
Laser Type:	Flash lamp laser Nd:Yag (Quantel ultra)
Eye-Safety Compliance:	EN 60825-1
Emitted Wavelength:	355 nm
Output Pulse Energy:	16 mJ
Pulse Repetition Rate:	20 Hz
Pulse Duration:	4 ns
Laser beam diameter:	38 mm
Beam expansion factor:	x10
Beam divergence:	$\cong$ 0.25 mrad
Telescope:	Lens
Telescope aperture diameter:	150 mm but 146 mm of useful aperture
Field of View:	$\cong$ 1.5 mrad (0 left beam and 3 mrad right beam)
Field of View tilt angle:	$\cong$ 1.1 mrad
Filter width (FWHM):	0.5 nm
Overlap:	52 m to 510 m
Detection:	2 x PMT (Analog and Photon counting)
PMT manufacturer:	Hamamatsu
Deathtime of PMT (PC):	14 ns
Data	
Data Format:	ASCII, HDF5
Data Transfer Protocol:	Ethernet

A.6 Multiple scattering correction

Figure A.5 shows the correction of measured extinction (black curves) which is influenced by multiple scattering depending of particle size and optical depth with the detection geometry of the used Leo-Lidar. In both upper panels the correction for an optical thick cirrus cloud and in both lower panels an optical thin cirrus clouds is shown. In panel a) an idealized three layered cirrus cloud from 7 to 10 km with a high extinction of $1 \cdot 10^{-3}$ m^{-1} and a 10 times lower extinction above and below is shown. The measured optical depth of the cloud is 1.19. The corrected extinction profiles are shown in color curves for three different ice particle effective radius. The least radius creates the smallest correction of the extinction profile in total as expected. The extinction is actually higher by a factor of 2 than the measured extinction by starting at the cloud base at 7 km. This factor decreases with increasing altitude for small radii and stay almost constant for larger radii of 10 or 50 µm. The same behavior is visible in the cloud layer above, whereby the true extinction gets smaller than the measured at the upper range for the small particle radius. In the thinner cloud layer above 9 km the true extinction is smaller for particle radii of 5 or 10 µm and nearly equal for the large particles. This show the influence on multiple scattering and the strength of the size depending forward scattering. As described above the strongest correction of extinction values is applied at the cloud base and increases with increasing particle radius. The altitude range for relaxation to the measured extinction values increases also with increasing particle radius. Thus the measured optical depth of 1.19 is corrected to the true value of 1.51 for particle radius of 10 µm. In panel b) a more natural cirrus extinction profile with a Gaussian shape is shown. Here the same effects occur as also visible in panel a). Nevertheless, the shape of the extinction profiles is more retained and particle independent. In panel c) and d) the same cirrus clouds are shown but with a smaller optical depth near the sub-visible limit of 0.03. The chosen particle radii are smaller suitable for a thin cirrus cloud, thus the extinction profiles from panel a) and c) or b) and d) can only compared for a radius of 10 µm. The effect on extinction profiles are similar to both cases a) and b). The cloud has a lower number concentration of potential scatter particles trough the lower optical depth. Therefore the distance between two scatter processes increase and detention time within the cloud and the FOV increases. This leads to a longer relaxation range for approaching of corrected and measured extinction profile. The relative amount of true and measured optical depth is in both cases (thin and thick) similar.

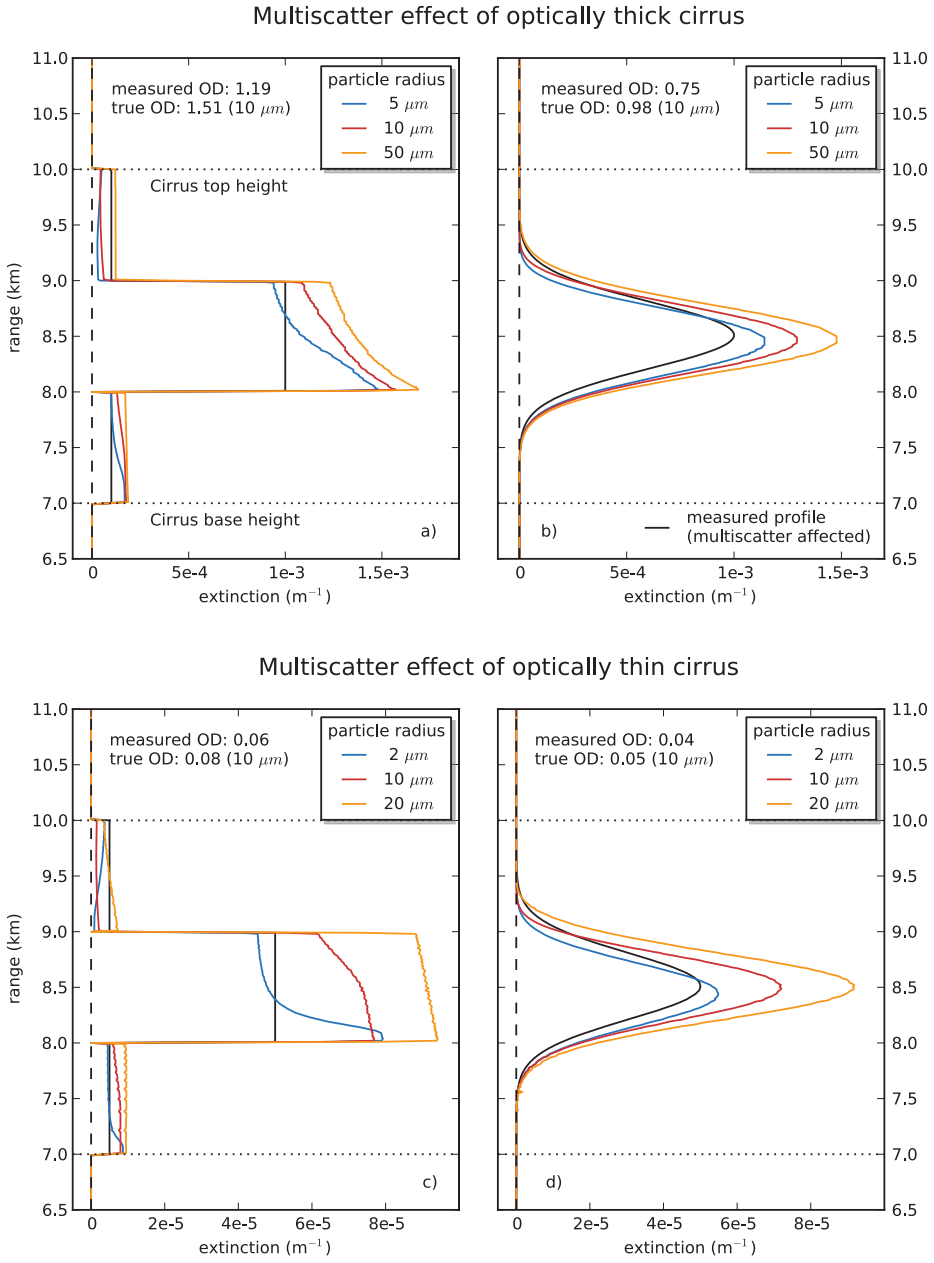

Figure A.5: Multiple scattering correction of measured extinction profile (black) for three different ice particle effective radii (blue, red and orange) of optically thick and thin cirrus clouds. Thick cirrus cloud with idealized extinction profile in a) and natural in b) with optical depth of 1.19 and 0.75, respectively. Thin cirrus cloud with idealized extinction profile in c) and natural in d) with optical depth of 0.06 and 0.04, respectively.

B Maid Appendix

B.1 Particle size distribution

The size distribution describes the amount of particles according to a specific size. In particle simulations and measurements the resolution of particle size such as the radius is finite and is given by the number of size bins (intervals) N and there width. One way of characterize and summarize particle size distributions is to express them with only view numbers like mean and median radius. From the number and mass size distribution it is easy to calculate a number-weighted average or a mass-weighted average, the count mean radius or mass mean radius, respectively. The count and mass median radius represent the radius which split the distribution into halves and is a crucial quantity to describe a size distribution.

In general, the standard average of a size distribution is described by the arithmetic mean of a weighted quantity x

$$r_{mean} = \frac{\sum_{i=0}^{N} r_i \; x_i}{\sum_{i=0}^{N} x_i}$$

and the statistical half of the distribution by the median

$$r_{median} = \left(\prod_{i=0}^{N} r_i^{n_i} \right)^{\frac{1}{N}} = exp\left(\frac{\sum_{i=0}^{N} ln(r_i) \; n_i}{\sum_{i=0}^{N} n_i} \right).$$

If we assume a monomodal lognormal size distribution (see Figure B.1) with a given number concentration, it is possible to derive all mean and median radii listed in Table B.1 with respect to count, surface, and mass. These radii are also shown in Figure B.1. The surface and mass distribution can easily calculated from the radius bins and assuming a particle density. Thus the mean and median radius of the length, surface, and mass distribution can calculated. Each radius shows the important points of the belonging distribution. In the box model MAID three mean radii are important. First the count median radius (CMR) which marks the radius with the largest amount of particles. Then the surface mean radius $\overline{r_{sm}}$ which represent the mean cross section of an ice particle reacting with radiation. Therefore this radius is important to compare the MAID results with a lidar or to calculate the extinction from simulations. This radius is also called effective radius. The last in MAID implemented radius is the mass mean

radius $\overline{r_{mm}}$. This radius implies the particle size where the average mass of the distribution is. This radius is typically larger than the mass median radius (MMR) where the most of the mass contribute to the distribution (see different radii in Figure B.1).

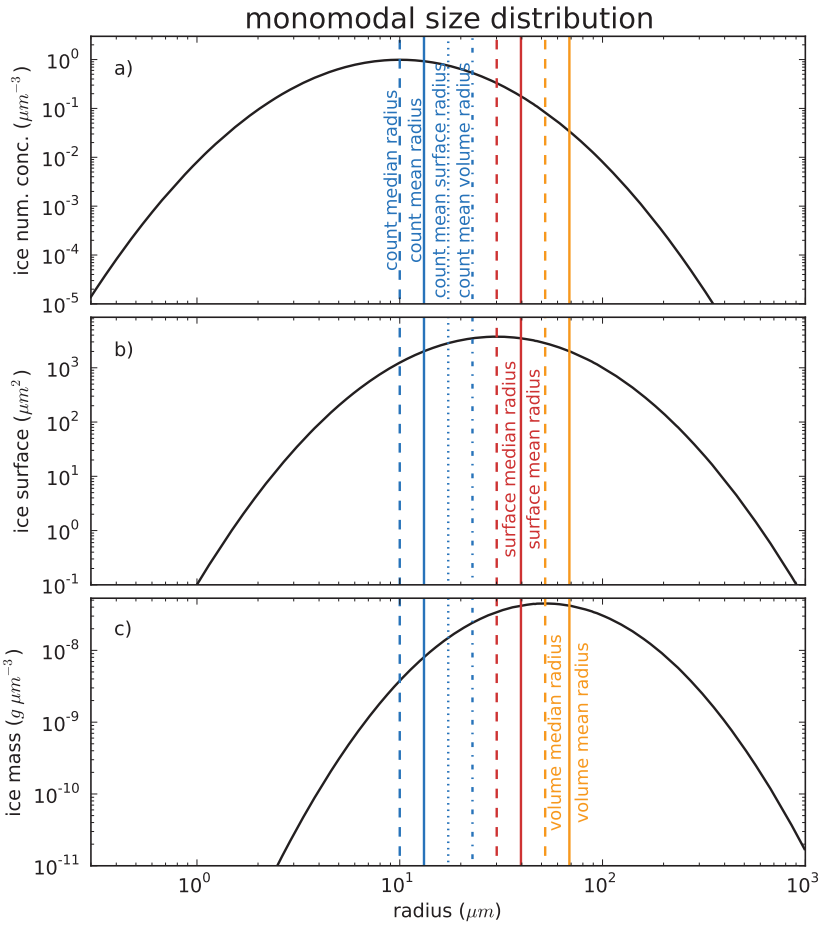

Figure B.1: Monomodal lognormal size distribution with all kinds of radii: a) number size distribution, b) surface size distribution, and c) mass / volume size distribution.

Table B.1: Different mean and median radii of a particle number distribution. For simplification all sums go over all N size bins.

Distr.	Median radius, geom. mean	Mean radius	Mean surface	Mean volume, mass
Count	$CMR = exp\left(\frac{\sum ln(r_i)\ n_i}{\sum n_i}\right)$	$\overline{r_{cm}} = \frac{\sum r_i\ n_i}{\sum n_i}$	$\overline{r_s} = \left(\frac{\sum r_i^2\ n_i}{\sum n_i}\right)^{\frac{1}{2}}$	$\overline{r_m} = \left(\frac{\sum r_i^3\ n_i}{\sum n_i}\right)^{\frac{1}{3}}$
Lenght	$LMR = exp\left(\frac{\sum ln(r_i)\ r_i\ n_i}{\sum n_i\ r_i}\right)$	$\overline{r_{lm}} = \frac{\sum r_i^2\ n_i}{\sum n_i\ r_i}$		
Surface	$SMR = exp\left(\frac{\sum ln(r_i)\ r_i^2\ n_i}{\sum n_i\ r_i^2}\right)$	$\overline{r_{sm}} = \frac{\sum r_i^3\ n_i}{\sum n_i\ r_i^2}$		
Volume, mass	$MMR = exp\left(\frac{\sum ln(r_i)\ r_i^3\ n_i}{\sum n_i\ r_i^3}\right)$	$\overline{r_{mm}} = \frac{\sum r_i^4\ n_i}{\sum n_i\ r_i^3}$		

B.2 Interpolation of temperature fluctuation

Figure B.2 illustrate the influence of linear and spline interpolated temperature fluctuations based on the same idealized MAID trajectory with an updraft of 0.1 m/s as also shown in Figure 3.1, but without sedimentation effect. While a linear interpolation have a discontinuity in the turning points, the cubic spline interpolation produces continuous transitions in the temperature and pressure fluctuations. The spline interpolation produces more realistic and physical more sensible behavior of air parcel movements. In Panel a) both interpolations are shown whereas the linear interpolation of temperature is shown in blue and the spline interpolation in red. In general, both curves are very close to each other and depict the temperature progress. Only the fluctuations interpolated with a spline function appear to be smoother. The spline interpolation achieve also a smoother and more realistic progress in relative humidity with respect to ice without having corners as can seen in Panel b). This has a direct effect on resulting ice particle properties (i.e. number and mean radius) as shown in Panel c). The effect is more or less localized to the point of ice formation as also visible in Section 3.2 where impact on various amplitudes σT is investigated. The spline interpolation create more higher cooling rates at the inflection points in the temperature progress and therefore a higher ice particle number. Due to the more realistic behavior of a continuous temperature and pressure progress, a cubic spline is recommended for the interpolation.

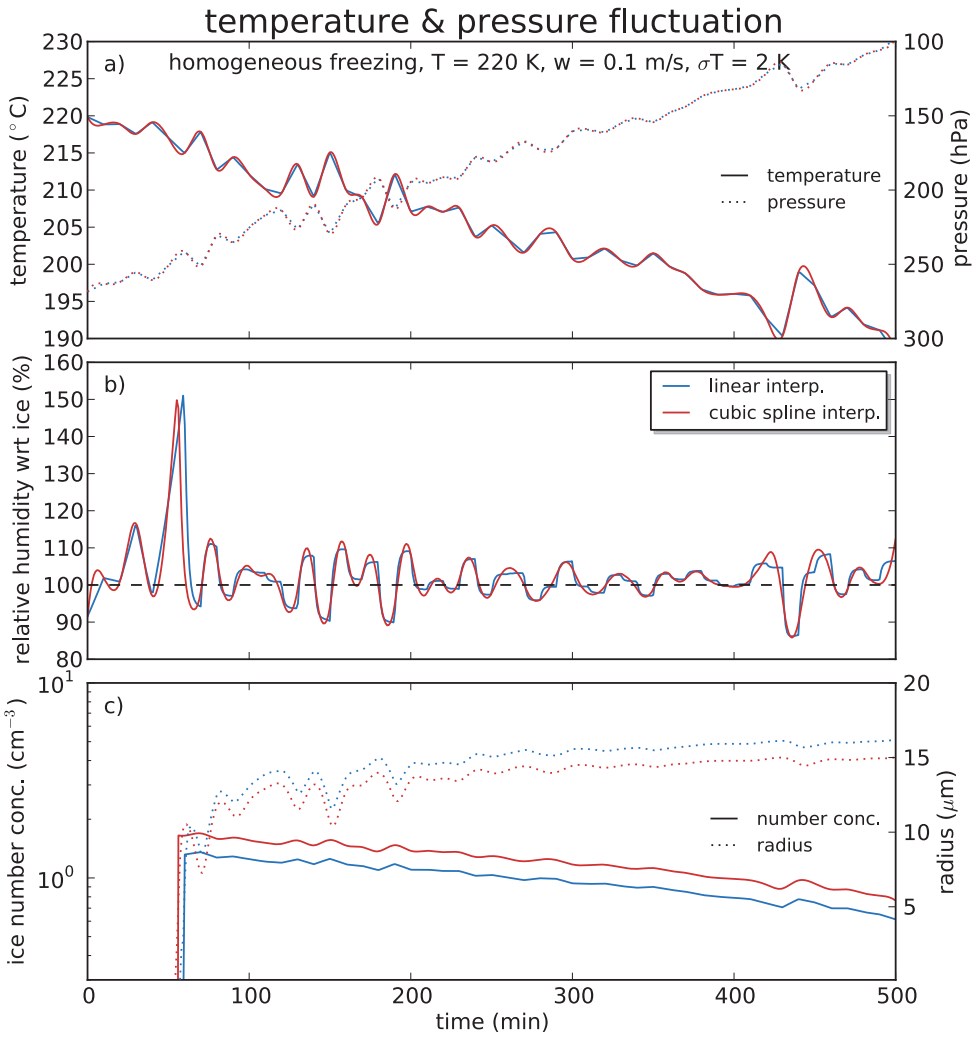

Figure B.2: Influence of linear and spline interpolated temperature fluctuations on microphysics and evolution of a homogeneous frozen cirrus cloud (no sedimentation): a) adiabatic temperature and pressure fluctuation b) relative humidity with respect to ice, and c) resulting ice particle concentration and mean radius.

C Acknowledgment

Now, that this work is done, it is time to thanks all the people who contribute directly or indirectly to this work. Without their help, support, and good nature this achievement would not be possible in this way or would even have taken considerably longer.

First of all I would like to thank my both supervisors Dr. Martina Krämer and Dr. Cornelius Schiller. They had the initial idea to enlarge the water and cloud group of the IEK-7 by a new instrument type, the lidar. This gave me the opportunity to start this work on cirrus cloud measurements in this enthusiastic and inspiring group. During all the time of this Ph.D. work Martina and Cornelius ideas were fruitful and a source of motivation and inspiration for me. I would like thank Martina for her support in the preparation of the volcanic-ash-induced cirrus paper and this thesis. Here, i would like to express my deep grief for my dear supervisor Cornelius Schiller, who passed away on 3 March 2012. We will miss his boundless energy and enthusiasm for atmospheric research.

I thank the director of the IEK-7 Prof. Dr. Martin Riese for giving me the opportunity to work at this institute with its enjoyable working atmosphere. I also thank him for reviewing the paper and this thesis. I am also grateful to Prof. Dr. Ralf Koppmann for the supervision of this thesis as the second examiner. I acknowledge the Helmholtz Gemeinschaft for the support of this thesis within the HGF program EOS (Earth Observing System).

I am very grateful to Patric Seifert and Albert Ansmann from the Institute for Tropospheric Research (IfT) in Leipzig for providing their expertise and knowledge in lidar measurements. Their description and explanations helped me a lot to understand the lidar key issues. I had the possibility for two research stays at the IfT were Patric introduced me into aspects of the Klett inversion and multiple scattering. Additionally, they gave me the opportunity to use their depolarization calibration setup to characterize the Leo-Lidar.

Sincere thanks to Dr. Jens-Uwe Grooß and Dr. Gebhard Günther for the introduction in the CLaMS model, its use for trajectory calculation, and providing regular and "special" ECMWF data for the analysis. Furthermore, i thank the Department of Atmospheric Science at the University of Wyoming for providing the radiosonde data. For the cooperation and support of the Leo-Lidar i wish to thank Leosphere. A special thanks goes also to Erika Kienast-Sjögren at the ETH Zürich for the nice discussions about the Leo-Lidar.

Many thanks go to Nicole Spelten and Anne Kunz for the wonderful time together in the office. We had always nice and interesting conversations. I'm grateful also for acquire a taste for sugar-containing things by feeding me with a large amount sweets. Thanks also goes to all

the other colleagues and friends who made my life (even) more enjoyable during the time of my Ph.D work in Jülich.

Last but not least i would like to dedicate loving thanks to my little family around me: To Katja for giving extraordinary patience, emotional support, and appreciation; to my sons Leonard and Justus, to have brought my life to a deeper satisfaction and happiness. They are two unbeatable reasons to let rest the work once a while.

Band / Volume 149
IEK-Report 2011. Climate-Relevant Energy Research
(2012), ca. 250 pp.
ISBN: 978-3-89336-809-9

Band / Volume 150
Netzintegration von Fahrzeugen mit elektrifizierten Antriebssystemen in bestehende und zukünftige Energieversorgungsstrukturen
Advances in Systems Analyses 1 (2012)
ISBN: 978-3-89336-811-2

Band / Volume 151
Stratospheric ClOOCl chemistry at high solar zenith angles
O. Suminska-Ebersoldt (2012), VI, 126 pp
ISBN: 978-3-89336-817-4

Band / Volume 152
Keramiken und Keramikkombinationen zur Feinstpartikelabscheidung mit Hilfe thermisch induzierter Potentialfelder und Elektronenemissionen
D. Wenzel (2012), XXV, 155 pp
ISBN: 978-3-89336-820-4

Band / Volume 153
Bildung von sekundären Phasen bei tiefengeologischer Endlagerung von Forschungsreaktor-Brennelementen – Struktur- und Phasenanalyse
A. Neumann (2012), 329 pp
ISBN: 978-3-89336-822-8

Band / Volume 154
Coupled hydrogeophysical inversion for soil hydraulic property estimation from time-lapse geophysical data
M. Cho Miltin (2012), xi, 79 pp
ISBN: 978-3-89336-823-5

Band / Volume 155
Tiefentschwefelung von Flugturbinenkraftstoffen für die Anwendung in mobilen Brennstoffzellensystemen
Y. Wang (2012), 205 pp.
ISBN: 978-3-89336-827-3

Band / Volume 156
Self-consistent modeling of plasma response to impurity spreading from intense localized source
M. Koltunov (2012), V, 113 pp.
ISBN: 978-3-89336-828-0

Band / Volume 157
Phosphorsäureverteilung in Membran-Elektroden-Einheiten dynamisch betriebener Hochtemperatur-Polymerelektrolyt-Brennstoffzellen
W. Maier (2012), VI, 105 pp.
ISBN: 978-3-89336-830-3

Band / Volume 158
Modellierung und Simulation von Hochtemperatur-Polymerelektrolyt-Brennstoffzellen
M. Kvesic (2012), ix, 156 pp.
ISBN: 978-3-89336-835-8

Band / Volume 159
Oxidation Mechanisms of Materials for Heat Exchanging Components in CO_2/H_2O-containing Gases Relevant to Oxy-fuel Environments
T. Olszewski (2012), 200 pp.
ISBN: 978-3-89336-837-2

Band / Volume 160
Ice Crystal Measurements with the New Particle Spectrometer NIXE-CAPS
J. Meyer (2013), ii, 132 pp.
ISBN: 978-3-89336-840-2

Band / Volume 161
Thermal Shock Behaviour of Different Tungsten Grades under Varying Conditions
O. M. Wirtz (2013), XIV, 130 pp.
ISBN: 978-3-89336-842-6

Band / Volume 162
Effects of ^{137}Cs and ^{90}Sr on structure and functional aspects of the microflora in agricultural used soils
B. Niedrée (2013), XII, 92 pp.
ISBN: 978-3-89336-843-3

Band / Volume 163
Lidar observations of natural and volcanic-ash-induced cirrus clouds
C. Rolf (2013), IX, 124 pp.
ISBN: 978-3-89336-847-1

Energie & Umwelt / Energy & Environment
Band / Volume 163
ISBN 978-3-89336-847-1

JÜLICH
FORSCHUNGSZENTRUM